UNITED NATIONS UNIVERSITY
UNU-GTP
Geothermal Training Programme

Orkustofnun, Grensasvegur 9,
IS-108 Reykjavik, Iceland

Reports 2016
Number 2

BOREHOLE GEOLOGY AND SUB-SURFACE PETROCHEMISTRY OF THE DOMES AREA, OLKARIA GEOTHERMAL FIELD, KENYA, IN RELATION TO WELL OW-922

MSc thesis
School of Engineering and Natural Sciences
Faculty of Earth Sciences
University of Iceland

by

Victor Omondi Otieno
Kenya Electricity Generating Company, Ltd. - KenGen
P.O Box 785-20117, Naivasha
KENYA
votieno@kengen.co.ke, kotienovic@gmail.com

United Nations University
Geothermal Training Programme
Reykjavík, Iceland
Published in December 2016

ISBN 978-9979-68- 406-0
ISSN 1670-7427

This MSc thesis has also been published in May 2016 by the
School of Engineering and Natural Sciences, Faculty of Earth Sciences
University of Iceland

INTRODUCTION

The Geothermal Training Programme of the United Nations University (UNU) has operated in Iceland since 1979 with six month annual courses for professionals from developing countries. The aim is to assist developing countries with significant geothermal potential to build up groups of specialists that cover most aspects of geothermal exploration and development. During 1979-2016, 647 scientists and engineers from 60 developing countries have completed the six month courses, or similar. They have come from Africa (38%), Asia (36%), Latin America (14%), Europe (12%), and Oceania (1%). There is a steady flow of requests from all over the world for the six-month training and we can only meet a portion of the requests. Most of the trainees are awarded UNU Fellowships financed by the Government of Iceland.

Candidates for the six-month specialized training must have at least a BSc degree and a minimum of one-year practical experience in geothermal work in their home countries prior to the training. Many of our trainees have already completed their MSc or PhD degrees when they come to Iceland, but many excellent students with only BSc degrees have made requests to come again to Iceland for a higher academic degree. From 1999 UNU Fellows have also been given the chance to continue their studies and study for MSc degrees in geothermal science or engineering in co-operation with the University of Iceland. An agreement to this effect was signed with the University of Iceland. A similar agreement was also signed with Reykjavik University in 2013. The six-month studies at the UNU Geothermal Training Programme form a part of the graduate programme.

It is a pleasure to introduce the 47th UNU Fellow to complete the MSc studies under a UNU-GTP Fellowship. Victor Omondi Otieno, BSc in Geology, from Kenya Electricity Generating Company – KenGen, completed the six-month specialized training in Borehole Geology through a special advanced 6-month training session given by UNU Geothermal Training Programme in Kenya, from July 2012 – February 2013. His research report, co-authored by Ms. Rose Kubai, was entitled: *Borehole geology and hydrothermal mineralisation of well OW-37A, Olkaria East geothermal field, Kenya.* After one and half year of geothermal work in Kenya, he came to Iceland for MSc studies at the University of Iceland, School of Engineering and Natural Sciences, starting in August 2014. In May 2016, he defended his MSc thesis presented here, entitled: *Borehole geology and sub-surface petrochemistry of the Domes area, Olkaria geothermal field, Kenya, in relation to well OW-922.* His studies in Iceland were financed by the Government of Iceland and KenGen through a UNU-GTP Fellowship from the UNU Geothermal Training Programme. We congratulate him on his achievements and wish him all the best for the future. We thank the School of Engineering and Natural Sciences, Faculty of Earth Sciences at University of Iceland for the co-operation, and his supervisors for the dedication.

Finally, I would like to mention that Victor's MSc thesis with the figures in colour is available for downloading on our website *www.unugtp.is*, under publications.

With warmest greetings from Iceland,

Lúdvík S. Georgsson, Director
United Nations University
Geothermal Training Programme

ACKNOWLEDGEMENTS

My heartfelt gratitude goes to my employer, Kenya Electricity Generating Company Ltd. (KenGen) for nominating and providing me with the study leave to pursue further studies at the University of Iceland. Sincere thanks goes to the Icelandic Government, the United Nations University- Geothermal Training Programme (UNU-GTP) through its able Director, Mr. Lúdvik S. Georgesson for funding this study. To the entire warm staff of UNU-GTP, Ingimar Haraldsson, Thórhildur Ísberg, Málfrídur Ómarsdóttir, Markús A. G. Wilde, and Rósa Jónsdóttir, thank you for your technical support and for making me feel always at home particularly during the harsh winter periods. Rósa you played a key role in delivering the required research papers and books, even from outside the UNU-GTP library fairly fast. I am deeply obliged to you and will always be.

I owe a large debt of gratitude to my supervisors; Gudmundur H. Gudfinnsson, Saemundur A. Halldórsson, Anette K. Mortensen and Björn S. Hardarson for the many insightful discussions, constructive comments and guidance during my study period. Your countless words of support utterly encouraged and motivated me. You helped me shape the line of my thought with very many intellectual suggestions. It was a great pleasure and honour to work with you and indeed I am very thankful. In the same token, I thank Dr. Hjalti Franzson and Dr. Kristjan Saemundsson for the innumerable discussions we held together regarding the various aspects of this study. Warm thanks are also extended to Atli Hjartarson for preparation of the microprobe samples.

To my fellow UNU MSc. and Ph.D. students who form a long list, I am grateful to you all for the times we spent encouraging each other and sharing common problems. In particular, your ingenuity and hardwork generated the insights that taught me how the World of science works. I recognize the unstinting support extended by my colleagues at KenGen in terms of timely data delivery. Joyce Okoo, Xavier Musonye, Danson Warui, Michael Mwania, David Wanjohi, Edwin Wafula and Lawrence Onyango, just to mention a few. You are indeed awesome people and I am greatly indebted.

To my family, thank you for your encouragement, infinite patience during my long absence and for allowing me a peaceful work time. Your love inspired me every day. Above all, Glory be to the Almighty God. None of this work would have been possible without his guidance and protection.

DEDICATION

This thesis is dedicated to my beloved wife, Vivian and my lovely daughter, Tasha.

ABSTRACT

Olkaria is a high temperature geothermal system located within the central sector of the Kenya Rift System, and associated with a region of Quaternary volcanism. Recharge into the system is exclusively by meteoric water, derived primarily from the high-altitude rift escarpments. Tectonic structures play without a doubt a pivotal role in enhancing fluid flow within the geothermal system. For this study, data and samples from four wells, OW-905A, OW-910, OW-917 and OW-922, have been used. Wells OW-905A, OW-910 and OW-917 were drilled within and along the proposed caldera structure. Well OW-922 is a step-out vertical well, drilled to the east of the proposed caldera structure. This study largely focuses on well OW-922, while, the other three wells have been included for comparison purposes. The study presents a comprehensive look at the borehole geology and hydrothermal mineralisation, sub-surface petrochemistry and microprobe analysis. Lithologies intersected by the study well include pyroclastics, tuff, rhyolite, basalt, trachydacite, basaltic trachyandesite, trachyandesite and trachyte. No intrusions are found in this well. Hydrothermal products in the study well occur both as replacement of primary components or glassy matrix and as open space filling in veins, fractures and vesicles. Evidence of a significant cooling process (up to over 110ºC) in the geothermal system around the study well is provided by the difference between measured formation temperature (127ºC) and inferred hydrothermal alteration temperature (epidote 240ºC). Cases of calcite overprinting epidote further points towards a cooling process.

Five feed zones have been deduced from the well and all are categorised as small. Generally, the well has low permeability and could not sustain discharge after 49 days of heat-up. Observations from temperature distribution across the field indicates that the study well is located outside the Olkaria Domes heat source, and consequently, outside the main Olkaria volcanic zone. Whole-rock chemistry displays a range of compositions of the samples of the study well, from basalt to trachyte or rhyolite, with the prevalence of the rocks being the highly evolved derivatives. Major oxides and trace element systematics are dominated by crystal fractionation, even though other differentiation processes cannot be ruled out. Evidence of a common differentiation mechanism for the surface and sub-surface rocks seems likely on the basis of comparison between the two groups of samples. Microprobe analyses have been carried out on epidote and chlorite in order to assess the chemical composition and the compositional range of the two minerals. It is found that most of the epidote are aluminium-rich, whereas, the chlorites are iron-rich varieties. Limited number of epidote and chlorite has however, impeded possible correlation of the stratigraphy in the four wells based on major and minor element contents.

TABLE OF CONTENTS

Page

1. INTRODUCTION....1
   1.1 General overview....1
   1.2 Overview of well OW-922....2
   1.3 Goals of the study....4
   1.4 Thesis layout....4

2. OUTLINE OF GEOLOGY....5
   2.1 Regional geology....5
   2.2 Geology of Olkaria volcanic complex....7
      2.2.1 Surface geology....7
      2.2.2 Sub-surface geology....9
   2.3 Structural geology and tectonics of OVC....11
   2.4 Hydrogeological setting....13
   2.5 Reservoir properties of Olkaria field....14
   2.6 Summary of drilling history....14
      2.6.1 Phase 1: Drilling of the surface hole....16
      2.6.2 Phase 2: Drilling of the intermediate hole....16
      2.6.3 Phase 3: Drilling of production hole....17
      2.6.4 Phase 4: Drilling of production section (main hole)....17

3. SAMPLING AND ANALYTICAL METHODS....18
   3.1 Sampling....18
   3.2 Analytical methods....18
      3.2.1 Binocular microscope analysis....18
      3.2.2 Petrographic microscope analysis....18
      3.2.3 X-ray diffraction analysis....18
      3.2.4 Inductively Coupled Plasma-Optical Emission Spectrometry (ICP-OES) analysis....19
      3.2.5 Electron microprobe analysis....19

4. RESULTS....20
   4.1 Lithology of well OW-922....20
      4.1.1 Pyroclastics....20
      4.1.2 Tuffs....20
      4.1.3 Rhyolite....20
      4.1.4 Basalt....21
      4.1.5 Basaltic trachyandesite....21
      4.1.6 Trachyandesite....21
      4.1.7 Trachydacite....21
      4.1.8 Trachyte....21
   4.2 Hydrothermal alteration....22
   4.3 Distribution of hydrothermal alteration minerals....22
   4.4 Hydrothermal alteration zonation....28
   4.5 Distribution of alteration mineral zones in the Domes area....30
   4.6 Feed zones....30
   4.7 Alteration and measured formation temperatures....33
   4.8 Whole-rock chemistry....34
   4.9 Major and trace element compositions....34
      4.9.1 Major elements....34
      4.9.2 Trace elements....36
   4.10 Classification of rock types....37
      4.10.1 TAS classification....38
      4.10.2 Al_2O_3 vs. FeO classification scheme....39

Page
4.11 Comparison of well OW-922 with surface and other sub-surface samples....40
4.11.1 Comparison with surface samples....40
4.11.2 Comparison with other sub-surface samples....40
4.12 Microprobe analysis....44

5. DISCUSSION....51
5.1 Lithological units....51
5.2 Hydrothermal alteration....51
5.3 Permeability and comparison of temperatures....52
5.4 Rock composition....54
5.5 Hydrothermal alteration effects on rock chemistry....54
5.5.1 Effects on major element geochemistry....54
5.5.2 Effects on trace element geochemistry....55
5.6 Magmatic differentiation processes....56
5.6.1 Major elements....56
5.6.2 Trace elements....57
5.6.3 Assessing other differentiation mechanisms....58
5.7 Comparison of surface and sub-surface samples....58
5.8 Compositional variation of alteration minerals....60
5.8.1 Epidote....60
5.8.2 Chlorite....61

6. CONCLUSION AND RECOMMENDATIONS....63
6.1 Conclusion....63
6.2 Recommendations....63

REFERENCES....65

APPENDIX A: Lithological description of well OW-922 based on binocular and optical petrographic analyses....70

APPENDIX B: XRD analysis of clay minerals in well OW-922....75

APPENDIX C: ICP-OES analysis procedure....79

APPENDIX D: EMP analysis for chlorite and epidote....80

LIST OF FIGURES

1. Map of the KRS showing the location of Olkaria Volcanic Complex....1
2. The sub-fields of Olkaria geothermal field....2
3. A section of the Olkaria Domes field showing location of well OW-922 and other study wells....4
4. DEM of the EARS....5
5. Map of the EARS showing elevations higher than 1200 m....6
6. Geological map of the Olkaria volcanic complex and the surrounding area....8
7. Surface formations and stratigraphic column of Olkaria volcanic complex....9
8. Geographical extents and stratigraphic units of the Olkaria eruptive centres....10
9. Sub-surface lithotypes of the Olkaria volcanic complex....10
10. Structural map of the Olkaria volcanic complex displaying various fault patterns....12
11. Piezometric map showing reservoir recharge areas for Olkaria and surroundings....13
12. A vertical schematic sketch of the conceptual model of Olkaria geothermal system....15
13. Drilling progress curve for well OW-922....16

Page

14. Lithology, location of feed zones, distribution of alteration minerals and alteration zones of well OW-922 23
15. X-ray diffractogram of air dried, glycolated and heated sample of smectite 26
16. Cross polarized image of mixed-layer clay at a depth of 2782 m. 27
17. A plane polarized image of fibrous chlorite filling a vesicle at 1826 m 28
18. X-ray diffractogram of illite and unstable chlorite 29
19. Distribution of alteration mineral zones across a section of the Domes area 30
20. Downhole pressure recovery logs for well OW-922 31
21. Feed zones in well OW-922 as deduced from logs, drilling parameters and geology 32
22. Comparison of inferred alteration and measured formation temperatures for well OW-922 34
23. Harker diagrams showing major element variations against SiO_2 for samples from well OW-922 35
24. Variation diagrams for a range of trace elements plotted against the index of differentiation, SiO_2 for samples from well OW-922 37-38
25. TAS diagram showing the compositional range for sub-surface rocks from well OW-922 39
26. Al_2O_3 vs. FeO classification of sub-surface rocks from well OW-922 39
27. TAS classification scheme showing comparison of sub-surface samples from wells OW-922, 905A, 910 and 917 and, surface samples from Olkaria 40
28. A comparison for variation in concentration of selected major element oxides for wells OW-922, 905A, 910 and 917 41
29. A comparison for variation in concentration of selected trace elements for wells OW-922, 905A, 910 and 917 44
30. BSE image of epidote from 864 m in well OW-910 46
31. BSE image of epidote filling a vesicle from 1560 m in well OW-905A 46
32. A WDS elemental map showing compositional zoning of epidote from 864 m in well OW-10 47
33. A WDS elemental map showing Fe (b) and Al (d) distribution within a single epidote grain from 2782 m in well OW-922 48
34. BSE image of chlorite replacing plagioclase at 1870 m in well OW-917 49
35. A possible conceptual model based on outcome of the study, along the traverse A-B 53
36. Variation diagrams showing the concentrations of Na_2O, Al_2O_3, K_2O and MnO against SiO_2 55
37. Variation diagrams showing the concentrations of Rb, Sr, La, Ni, Ba and Y against Zr 56
38. A plot of La vs. Zr. and Y vs. Zr showing different magmatic differentiation processes 59
39. Harker's variation diagrams between various pairs of incompatible trace elements displaying fractional crystallisation 60

LIST OF TABLES

1. Utilization of geothermal energy for electric power generation in Olkaria 3
2. Drilling phases and casing design for well OW-922 15
3. Alteration of primary minerals and order of replacement in well OW-922 22
4. Interpreted permeable zones based on geological observations 33
5. Major and trace element results for well OW-922 based on ICP-OES analysis 42-43
6. Representative EMP analyses of epidote from wells OW-922, 910 and 905A 46
7. Range and average molar proportion of pistachite (Xps) component in epidote 47
8. Representative EMP analyses of chlorite for wells OW-922, 910, 917 and 905A 49
9. Molar ratio of chlorite from wells OW-922 and 910 50

ACRONYMS AND ABBREVIATIONS

Aus	Additional units
BP	Before present
BSE image	Backscattered electron image
CKPP	Central Kenya peralkaline province
CT	Cellar top
DEM	Digital elevation model
EARS	East African Rift System
EMP	Electron microprobe analysis
GWDC	Great Wall Drilling Company, Ltd.
HFSE	High field strength elements
ICP-OES	Inductively Coupled Plasma-Optical Emission Spectrometry
ITEs	Incompatible trace elements
ÍSOR	Iceland GeoSurvey
Ka	Thousand years
KenGen	Kenya Electricity Generating Company, Ltd.
KRS	Kenyan Rift System
LILE	Large ion lithophile elements
LREE	Light rare earth elements
Ma	Million years
m a.s.l.	metres above sea level
MER	Main Ethiopian Rift
MLC	Mixed Layer Clay
MWe	Megawatt electrical
OD	Outside diameter
OVC	Olkaria volcanic complex
OW	Olkaria well
POOH	Pulling out of hole
ppm	parts per million
RIH	Running in hole
RKB	Rotary Kelly bottom
ROP	Rate of penetration
TAS	Total alkali versus silica
TD	Total depth
WOC	Wait on cement
WDS	Wavelength dispersive spectrometer
Xps	Mole fraction of pistachite
XRD	X-ray diffraction

1. INTRODUCTION

1.1 General overview

Olkaria geothermal field is a high-enthalpy geothermal field (temperature > 200º C at 1000 m depth), associated with a region of Quaternary volcanism in the Kenyan Rift System (KRS). The Olkaria geothermal field has been extensively explored and developed since the 1980s. Over the past 35 years, the geothermal field has been the study site for new and innovative geological and geothermal research in Kenya. The geothermal system is located in the Olkaria Volcanic Complex (OVC), a relatively young (~ 20 ka), salic volcanic complex, characterised by the eruption of peralkaline rhyolites (Omenda, 1998; Macdonald et al., 2008). Nine other similar Quaternary volcanic centres occur in the axial region of the KRS and are potential geothermal resources according to surface exploration studies (Simiyu, 2010). The OVC is located in the central sector of the KRS, ~125 km northwest of Nairobi city and ~40 km southwest of Lake Naivasha (0° 53'S; 36° 18'E) (Figure 1). The extent of the OVC is estimated to be ~240 km^2 (Clarke et al., 1990). It is bound in close geographical proximity to the north by Eburru, a predominantly pantelleritic volcanic complex, to the east and south by Longonot and Suswa volcanoes, respectively. However, chemical features indicate that all these four adjacent volcanic complexes, situated less than 50 km apart are quite distinct and derived from separate magmatic systems (e.g. Macdonald and Scaillet, 2006). Unlike Eburru, Longonot and Suswa, which are complexes with a distinct caldera, the OVC lacks a proven caldera structure. Various scientific studies have been conducted to establish the existence of the caldera structure with little success. Some scholars (e.g. Simiyu and Keller, 2000) have postulated that the group of coalesced rhyolitic domes in the eastern and southern segments of the volcanic complex mark the rim of a caldera structure.

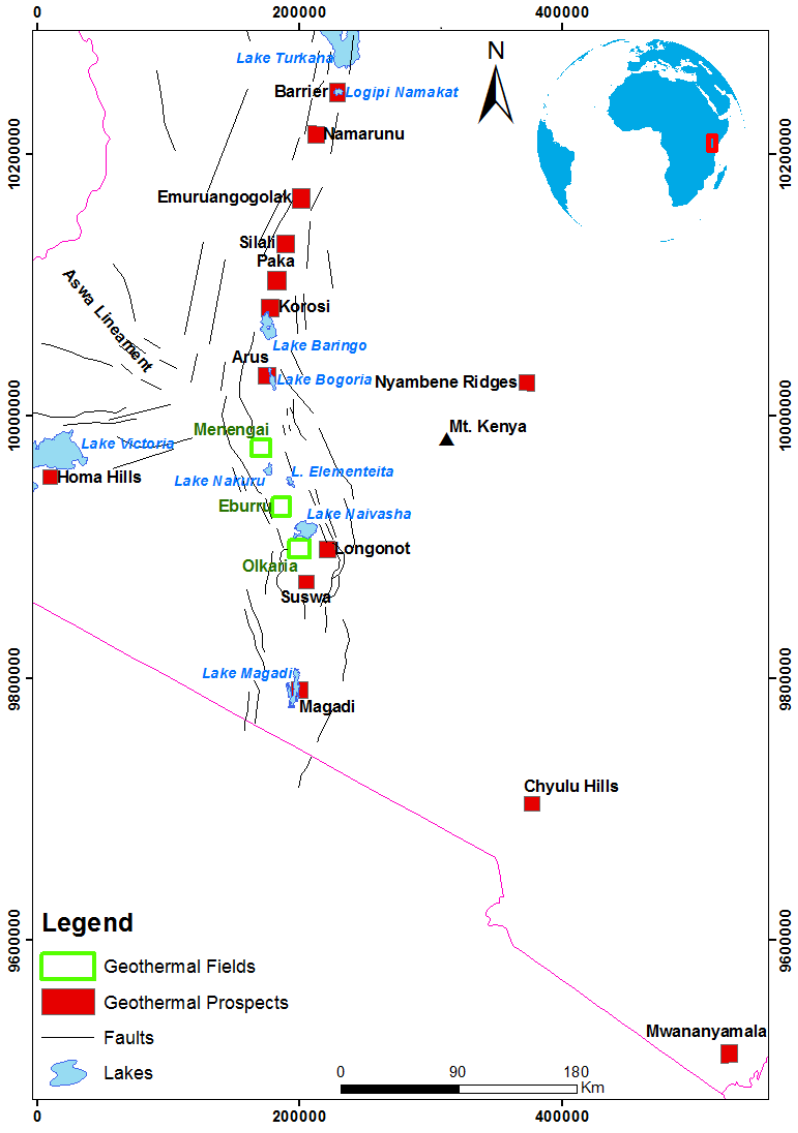

FIGURE 1: Map of the Kenyan Rift System (KRS) showing the location of Olkaria volcanic complex and other surrounding volcanic centres (modified from Ofwona et al., 2006)

Other researchers (e.g. Bliss, 1979) have argued that the great thickness of comenditic lavas (at least 1 km from borehole data) may well suggest the existence of a central comendite volcano in Quaternary times. Such a view would be consistent with the voluminous outpourings of comenditic lavas observed on the surface within the OVC. While this interpretation seems possible, the situation is complicated by the lack of ignimbrite deposits within and in the surrounding area of OVC.

Exploitation of geothermal resources at Olkaria began in the early 1980s and continues to date with more than 200 wells having been drilled, with a depth range of between 950 and 3200 m. The Olkaria geothermal field has been divided into seven sub-fields with Olkaria hill (Figure 2), a prominent geological feature about 340 m high and a basal diameter of 2 km being the reference point. Each of these sub-fields has been explored either partially or completely. They include Olkaria East, Olkaria Northeast, Olkaria Northwest, Olkaria Southwest, Olkaria Central, Olkaria Southeast and Olkaria Domes (Figure 2).

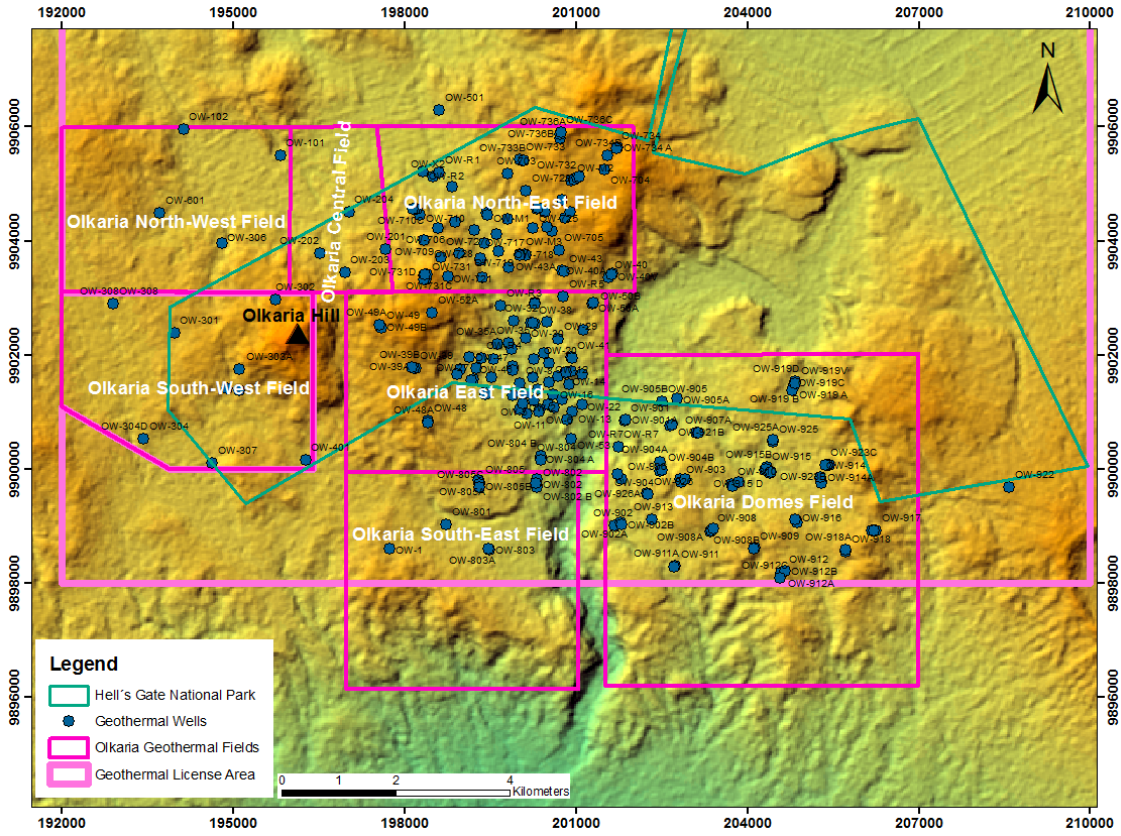

FIGURE 2: The sub-fields of Olkaria geothermal field (modified from Otieno and Kubai, 2013)

Olkaria East sub-field was the first part of the system to be developed in 1981. Exploitation of the extensive geothermal resource at Olkaria is mainly for electricity production at four conventional power plants; the Olkaria I, Olkaria I (AUs 4 & 5), Olkaria II, Olkaria III (OrPower) and Olkaria IV power stations. In addition, there are several wellhead generators installed and are operational within the geothermal field. As of the end of February, 2016, the aggregate installed generating capacity of the combined Olkaria stations is estimated at ~654 MWe. Resource consent for a 140 MWe power plant development at Olkaria V was granted by a Board of Inquiry process in May, 2015, with inauguration of construction work slated to begin in the course of this year. Although other opportunities for direct use are being explored, the activity is currently largely restricted to greenhouse heating (Oserian Development Company) and balneology (Olkaria Spa). A summary of the power plants, including the year of commissioning and the effective installed capacity, is listed in Table 1.

1.2 Overview of well OW-922

This study largely focuses on well OW-922, in addition to wells OW-905A, 910 and 917. Well OW-922 is a step-out vertical well drilled between April and September, 2014 at surface coordinates X= 208675; Y= 9899449 and Z= 2126 m a.s.l. It is located approximately 2.5 km directly east of the proposed Olkaria ring structure (Figure 3). The purpose of drilling this well was to appraise the resource potential of the mentioned area so as to expand production drilling to the plain outside the ring structure.

TABLE 1: Utilization of geothermal energy for electric power generation in Olkaria

Power plant name	Year commissioned	No. of units	Status	Total installed capacity	Total running capacity
				MWe	MWe
Olkaria I	1981 (15 MWe) 1982 (15 MWe) 1985 (15 MWe)	3	Operating	45	45
Olkaria II	2003 (70 MWe) 2010 (35 MWe)	3	Operating	105	105
Olkaria I (AUs 4 & 5)	2015	2	Operating	150	140
Olkaria III (OrPower)	2000 (53 MWe) 2008 (39 MWe) 2014 (17 MWe) 2016 (30 MWe)	-	Operating	140	140
Olkaria IV	2014	2	Operating	150	140
Olkaria wellheads	2012- 2015	-	Operating	~ 64	~ 64

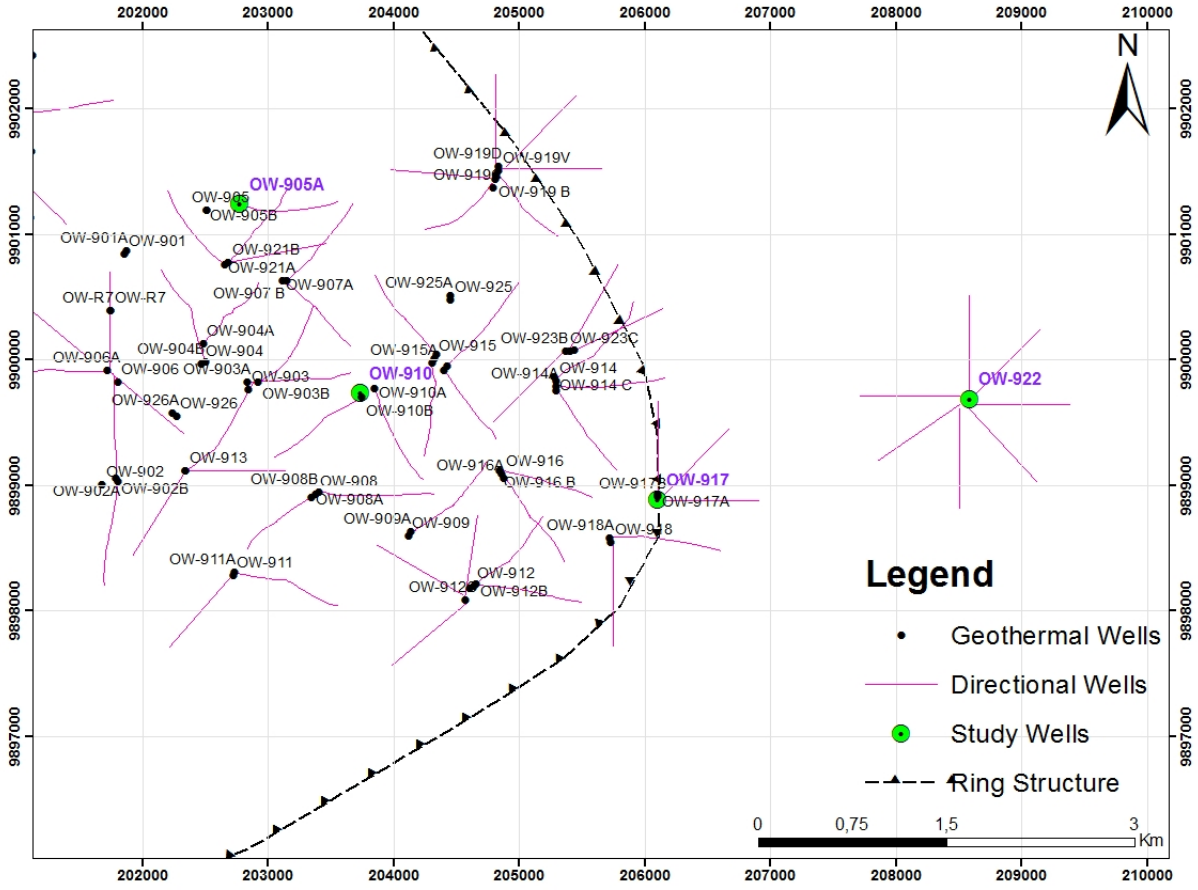

FIGURE 3: A section of the Olkaria Domes field showing location of the step-out well OW-922 and other study wells OW-910, 917 and 905A. Also shown are other drilled wells. The black triangles delineate the outline of the proposed ring structure

This has been necessitated by the renewed focus by the Kenyan government on development and utilisation of the geothermal resources for electricity generation. The government has identified additional supply of renewable energy as a fundamental foundation of achieving its Vision 2030 blue print. The latter seeks to transform the country into a newly industrialised, middle-income economy. As a result, Kenya Electricity Generating Company, Ltd. (KenGen), the leading power producer in the country, has embarked on efforts to escalate development of geothermal resources in sync with its

geothermal expansion programme. On the other hand, wells OW-905A, 910 and 917 were drilled within and along the proposed Olkaria caldera structure between November, 2007 and December, 2012. These wells have been adopted for this study based on various aspects; specifically owing to the readily available data on borehole geology and sub-surface petrochemistry from a previous study (Musonye, 2015). Until recently, there were no prior sub-surface petrochemical data (major and trace elements) since past petrochemical studies were confined only to surface rocks (e.g. Omenda, 1997; Macdonald et al., 2008; Marshall et al., 2009).

1.3 Goals of the study

The specific aims of this study are three fold;

1. To study the borehole geology of well OW-922 by analysis of drill cuttings in order to identify the stratigraphy and the sub-surface geological formations. The borehole geology study will clarify the geothermal conditions in the system east of the Domes and lead to comprehensive understanding of the hydrothermal mineralisation, temperature conditions based on alteration minerals and temperature loggings, major sources of permeability and water-rock interaction processes.
2. To investigate the chemical characteristics of the rocks in well OW-922 and attempt to decipher the processes of their petrogenesis. These will be compared with petrochemical data from wells OW-905A, 910, 917 and surface samples from Olkaria and neighbouring minor eruption centres to establish any petrogenetic connection.
3. To assess the chemical composition and variation in compositional range of epidote and chlorite, as well as the variables likely influencing the compositional changes.

1.4 Thesis layout

Chapter 1: Here, the project area is introduced, including the sub-divisions, total installed capacity and location of the study wells. The objectives of this study and the outline of the thesis are presented.
Chapter 2: Provides an overview of the regional geology of the East African Rift System. An elaborate description of both surface and sub-surface geology, structural and tectonic setting, hydrogeological setting and reservoir characteristics of the study area. Also presented is the drilling history of well OW-922.

Chapter 3: Provides an overview of the analytical methods used to achieve the project objectives. Analytical techniques spanning from binocular microscope to electron microprobe analysis are described.

Chapter 4: Presents synthesis of borehole geology, whole-rock chemistry and electron microprobe analytical results. In borehole geology, the lithologic units intercepted by the drill hole are discussed. Also discussed are the distribution of hydrothermal mineralisation, feed zones and a correlation between inferred alteration and measured formation temperatures. In whole-rock analysis, a petrochemical classification of the sub-surface rocks in the study well and the compositions of major and trace elements are explained in detail. Chlorite and epidote chemical compositions derived by electron microprobe (EMP) analysis are detailed.

Chapter 5: Provides an in-depth discussion based on the outcome of the analytical results.

Chapter 6: This chapter incorporates the conclusions based on the outcome of the findings envisaged in all the analyses and future frontiers recommended.

2. OUTLINE OF GEOLOGY

2.1 Regional geology

The East African Rift System (EARS) is considered an archetypal continental rift in the initial stage of continental breakup (Achauer and Masson, 2002) that is still in close proximity to the underlying thermal anomaly (mantle plumes). The evolution of the EARS is strongly believed to be structurally controlled (Smith and Mosley, 1993) by the exploitation of weak collisional zones at the contact between the Proterozoic orogenic belts and the Archean Tanzanian Craton by the rift faults (Shackleton, 1996). South of Turkana (Figure 1), the rift is divided into two distinct branches that encircle the robust Tanzanian Craton: an older, volcanically active eastern branch and a younger, much less volcanic active western branch (Ring, 2014) (Figure 4). The eastern branch extends from the Red Sea in the Afar region, straddles through the Main Ethiopian Rift (MER), the Kenyan (Gregory) Rift and the basins of the Tanzania divergence before terminating further south in Beira, Mozambique, a total distance of more than 4000 km. By contrast, the western branch extends over a distance of more than 2100 km from Lake Albert (Mobutu) in the north to Lake Malawi (Nyasa) in the south (Chorowicz, 2005).

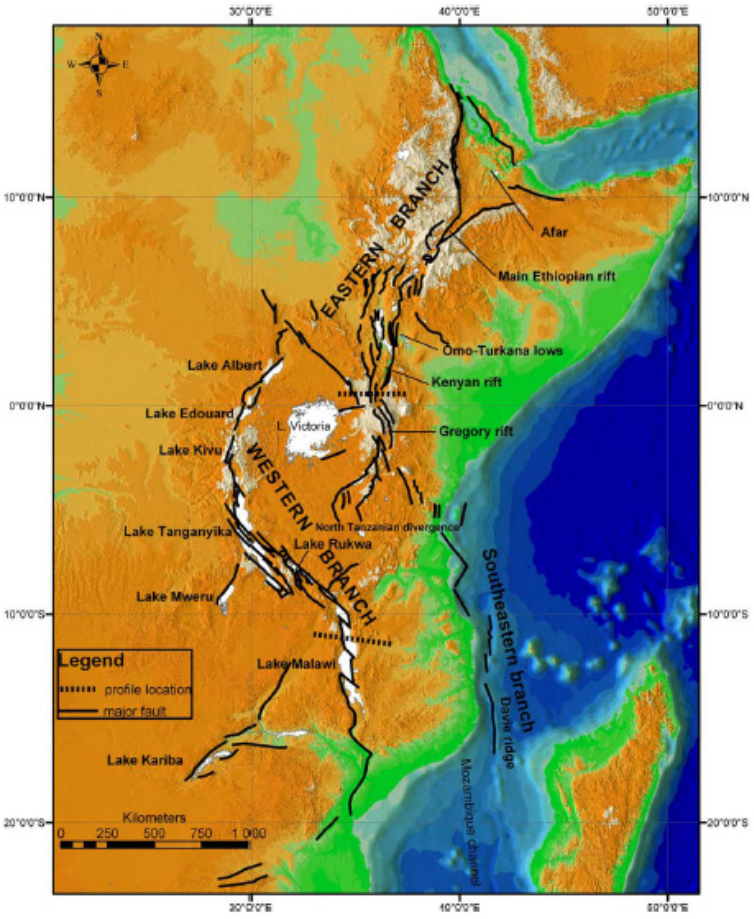

FIGURE 4: DEM of the EARS. Black lines represent main rift faults, whereas, white surfaces are lakes (modified from Chorowicz, 2005)

The zone is typically trough-like, ~40 to 65 km wide, and traverses two broad, elongated domal uplifts in Ethiopia and Kenya. The elevation of the rift floor is highest in the central part of the domes, 2000 m in Kenya and 1700 m in Ethiopia, and decreases progressively to the fringes. The onset of topographic uplift in the EARS is poorly dated. However, it certainly preceded graben development (Baker et al., 1972). The evolution of EARS dates back 30-45 Ma (Ring, 2014). Rifting is generally assumed to have developed as a result of the upwelling of a voluminous mantle plume (the African Superswell), which continuously impinged upon the base of the stretched continental lithosphere (Ebinger and Sleep, 1998). The driving force for the process has been ascribed to a hot, relatively fertile asthenospheric plume or diapir emanating from the top of the African Superswell in the upper few hundred kilometres of the mantle (Ebinger and Sleep, 1998). To date, considerable uncertainty still exists about the number of plumes influencing magmatism and tectonics beneath the EARS. Specifically, the depth extent and continuity of the hot asthenospheric material remains a tantalizing question which has evoked much speculation and debate (Chorowicz, 2005).

Based on plate analysis, the rift marks a line of very slow crustal spreading, extension being more active in the Red Sea – Gulf of Aden area, approximated at ~2 cm/year. In the Main Ethiopian rift it is estimated at ~1 mm/year, and further less than 1 mm/year in the Kenyan Rift and southwards (Ring, 2014). Propagation of the rift began as a chain of marginally warped depressions, which were accentuated as

domal uplift proceeded, until, in mid-Miocene to early Pliocene times, faulting produced asymmetrical grabens. The final uplift phase in the early Pleistocene was accompanied by major graben faulting, and subsequent faulting has intensely fractured the floor of the rift along an axial zone marked by caldera volcanoes. Seismic velocity information from refraction measurements and tomography experiments, reinforced by gravity studies (Ebinger, 2005), indicate that the eastern rift lies along a zone of progressive crustal thinning with local crustal disruption.

According to Baker et al. (1972) the uplift of the Ethiopian and Kenyan domes (Figure 5) has been synchronous in three major pulses of late Eocene (44-38 Ma), mid-Miocene (16-11 Ma), and Plio-Pleistocene (5-0 Ma) age. Volcanism of intermediate and salic type displays some relation to uplift in time and space and to the onset of graben faulting. However, major flood basalt extrusions in the early Tertiary in Ethiopia were related to massive crustal warping along the future rift margins (Williams, 1970). The volcanism associated with EARS is overwhelmingly alkaline, and at some volcanoes a strongly alkaline fractionation series is distinguishable from a more mildly alkaline series (Williams, 1970). The flood phonolites, trachytes, rhyolites, and ignimbrites of Kenya, and the pantelleritic ignimbrites of Ethiopia, could have resulted from anatexis of a mantle-derived accreted layer at the base of the crust (Baker and Wohlenberg, 1971).

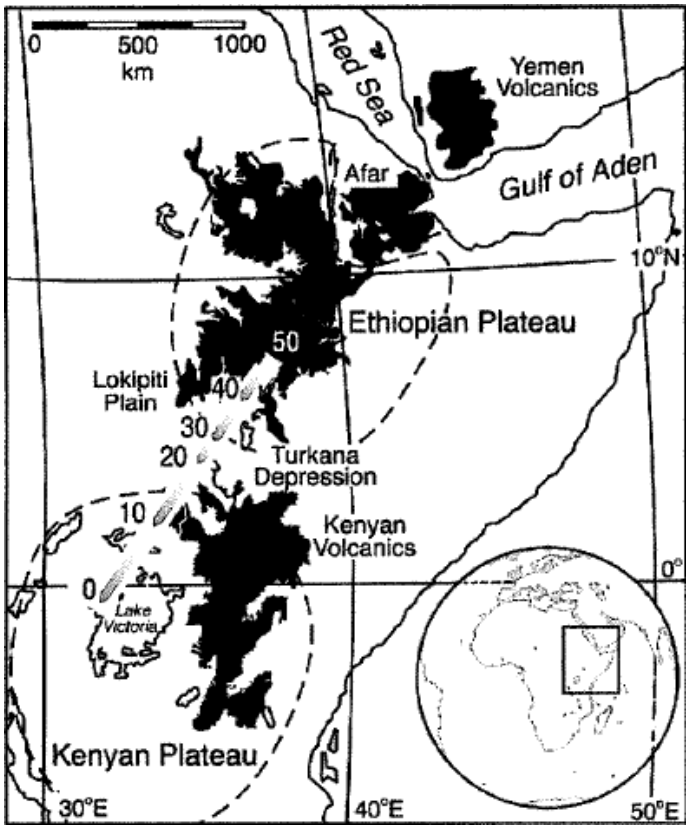

FIGURE 5: Map of the EARS showing elevations higher than 1200 m (black areas), evidencing the main Ethiopian and Kenyan Plateaux (dashed lines). The black areas mark the Cenozoic rocks of the Rift (Macdonald et al., 2001)

The evolution of the KRS, a complex graben ~ 40-65 km wide bounded by major rift faults arranged *en echelon,* dates back to the East African orogeny. The rift bisects the Kenya domal uplift, which itself is superimposed on the eastern margin of the East African plateau (Baker et al., 1972). The KRS is also located close to the boundary of the Tanzanian Craton and the Pan-African Mozambique shear belt. Volcanism associated with the KRS started during the Miocene epoch (~ 24 Ma), resulting in widespread basaltic eruptions in the Turkana topographic depression, a failed Mesozoic rift system (Nyblade and Robinson, 1994). The Miocene basalts were subsequently faulted and followed by the relatively extensive, reliably dated flood phonolites. The latter are of chemically homogeneous composition and were erupted from the crest of the Kenya dome in the late Miocene and early Pliocene (Baker et al., 1972). The total volume of eruptive rocks is estimated to be > 220,000 km^3, with a thickness of up to 900 m, as revealed by faulting at the rift margins. In an important contribution, Ebinger and Sleep (1998) suggest the flood phonolites to be a product of partial melting of the lowermost part of the crust.

Volcanism off the rift axis was concurrent with the rifting process and is responsible for the formation of the vast, uplifted, off-rift volcanic centres, namely Mt. Kenya, Chyulu and Huri hills, located on the eastern flanks (Figure 1). It has been observed that these three sites of domal uplift are not rifted, and, support a model whereby doming predated rifting (Wilson, 1989). Further block-faulting of the Miocene volcanics produced noticeably massive and extensive, more evolved eruptions of trachytic ignimbrites in the central area, provisionally assigned to lower Pliocene (Ring, 2014). The trachytic ignimbrites formed the Mau and Kinangop tuffs. A third faulting episode, which followed the ignimbrite eruptions,

resulted in the formation of the graben structure, as it is known today (Baker et al., 1972). In the developing graben, successive fissure eruptions produced approximately 900 m thick layers of trachytes, basalts, basaltic trachyandesites and trachyandesites. The plateau rocks that filled the developing graben were subsequently block-faulted to create high-angle normal faults, which are common in the axial graben of the rift floor. The fractures apparently served as conduits for a series of Quaternary volcanoes of basaltic to silicic composition (Ebinger and Sleep, 1998).

OVC is a classical example of such a Quaternary volcano of the KRS. Characteristic volcanism within the OVC and other centres exposed on the periphery of the complex (e.g. Oserian, Kibikoni, Olenguruoni, Broad Acres and the south-westerly Arcuate Domes) (Figure 8) are dominated in outcrops by peralkaline rhyolite domes and lava fields. The range of the stratigraphic units observed in each centre is variable. Similarly, each eruption centre corresponds to a different age as discussed by Marshall et al. (2009). Two main magmatic differentiation processes, namely crustal anatexis and crystal fractionation, have been proposed by Davies and Macdonald (1987) to explain the generation of felsic rocks at OVC and along the Gregory Rift at large.

2.2 Geology of Olkaria volcanic complex

Knowledge of the sequence, nature and architecture of the stratigraphy is fundamental for understanding both the surface and sub-surface geology of the OVC. The current knowledge on the geology of OVC and its surroundings presented hereafter, derives from the detailed pioneering work of many scholars (e.g. Clarke et. al., 1990; Marshall et al., 2009; Omenda, 1998). Their work has provided the foundation upon which more recent work has continued to build and has been refined through subsequent field development. The OVC constitutes part of the Central Kenya Peralkaline Province (CKPP) (Macdonald and Scaillet, 2006), which coincides with the Kenya Dome; a ~ 300-400 km wide topographic culmination in the course of the rift, with the apical region postulated to be lying around the Lake Nakuru area (Figure 1) (Macdonald and Scaillet, 2006). Nearly 80 volcanic centres composed of lavas and/or pyroclastic rocks formed by eruptions through fault zones or occuring as steep-sided domes are found within the volcanic centre, hence the term *complex*. Clarke and co-workers (1990) have notably placed the evolution of the OVC to be in the period between 22-20 ka BP.

2.2.1 Surface geology

The surface lithologic units in OVC are dominated by comenditic lavas, pumice fall and pyroclastics (Figure 6). A large fraction of the pumice fall and pyroclastic deposits is hypothesized to have originated from Longonot and Suswa volcanoes, lying immediately 20 km east and 40 km south of OVC, respectively. However, there is need for geochemical analysis of the deposits from the three volcanic centres to establish this assertion. Even though it has not been possible to enumerate systematically the contribution of pyroclastic deposits from each of the three centres, the pyroclastic activity at Longonot is presumed to post-date volcanism at Olkaria (Omenda, 1998). Occurrence of the comendites is restricted to OVC and it is the only area in the whole of the KRS with these rocks on the surface.

Clarke et al. (1990), listed six stages in the evolution of the complex based on their geological work. A tabulation of the sequence of volcanic groups is provided in Figure 7 and their distribution summarised in ascending order as discussed below. On the other hand, Olkaria eruptive centres and their manifestation as distinct topographical units are shown in Figure 8.

Stage 1: The earliest stage, of uncertain age, resulted in a pile of dominantly trachytic lava and pumice. These are termed Olkaria trachyte formation (O_t) and Maiella pumice formation (M_p). The former is exposed mostly along ridges and gullies in the southwest portion of the complex, whereas the latter is thought to have been erupted from the extensive vents in the western segment of the complex.

Stage 2: This stage, also of uncertain age is believed to mark the collapse of the proposed caldera structure, leaving behind a depression 11 × 7.5 km across. The suggested caldera formation was preceded by an eruption of a large volume of densely welded pantellerites of the Ol-Njorowa pantellerite

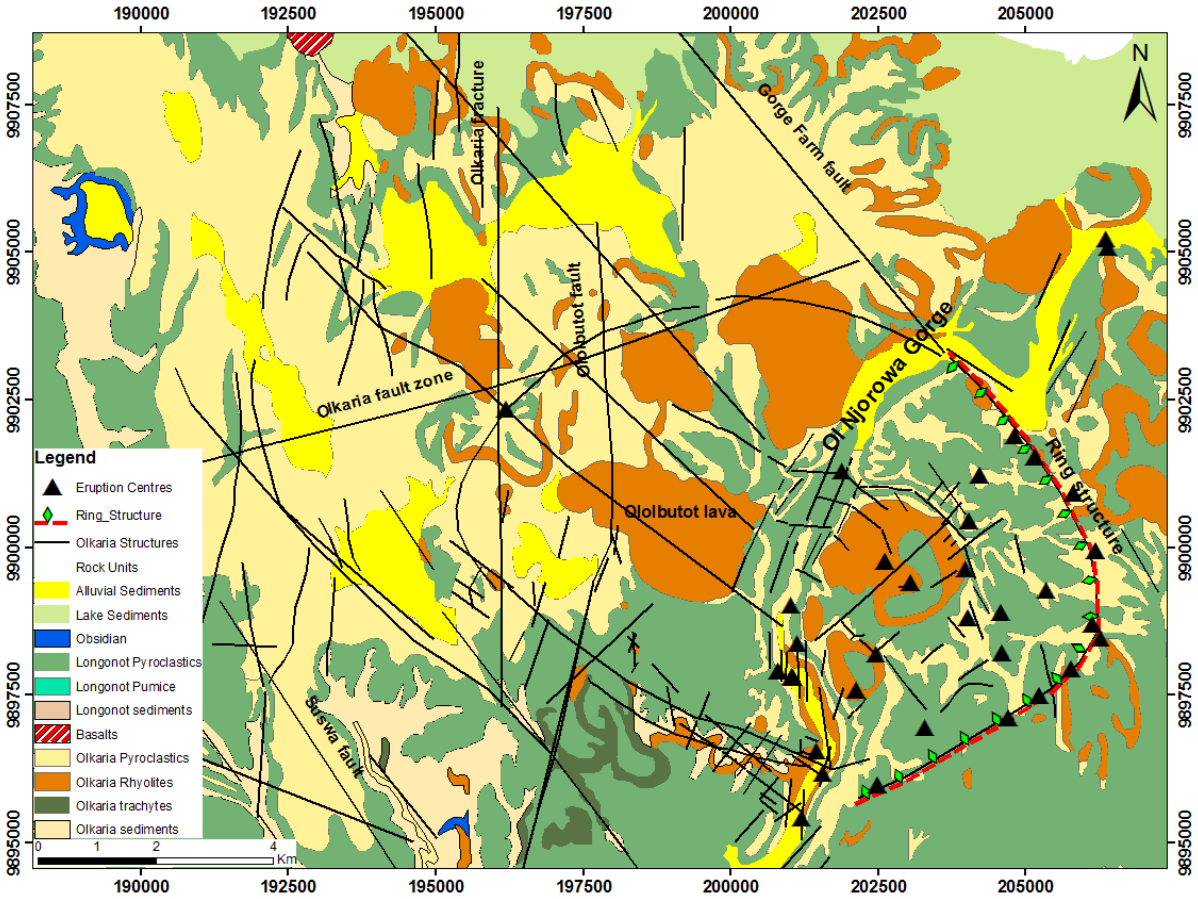

FIGURE 6: Geological map of the Olkaria volcanic complex and the surrounding area (modified from Clarke et al., 1990)

Formation (O^1). The latter are mainly exposed in the deepest sections of Ol-Njorowa gorge (Figures 6 and 7). Based on field observations, Clarke et al. (1990) relied on a group of coalesced rhyolitic domes (Figure 8), forming distinct topographic features in the eastern and southern parts of the complex to infer the ring structure. However, the caldera structure is still poorly constrained because the curved lineament of rhyolitic domes is adjudged to demarcate only 30% of a caldera rim.

Stage 3: This stage was characterised by early post-caldera activity and is represented by the eruption of pyroclastic rocks (Op^2) and peralkaline rhyolitic lavas (O^2) of the lower comendite member of the Olkaria comendite formation. The formation has been dated by Clarke et al. (1990) at > 9150±110 BP.

Stage 4: Involved ring dome building (O^3) and the eruption of thick surge deposits (Op^3) representing the middle comendite member. ^{14}C dating places the age for this member at between 9150±110 BP and 3280±120 BP (Heumann and Davies, 2002).

Stage 5: General resurgence of the caldera floor lead to the formation of short, thick comendite flows of the upper comendite member (O^4). This has been dated at >3280 BP (Clarke et al., 1990).

Stage 6: This stage was centred on the N-S Ololbutot fissure system (Figure 6). The most notable expression of this stage is very thick comenditic flows of the Ololbutot comendite member (O^5). The youngest of these flows is the Ololbutot lava, dated at 180±50 BP by ^{14}C (Macdonald and Scaillet, 2006).

Apart from the stages of evolution of the OVC, Clarke et al. (1990) also recognized a series of eruptive mafic rocks, occuring both to the north and south of the Olkaria Domes field. The Lolonito basalt formation (Ba^1) is found to the south (Figure 7), forming a string of small outcrops and largely comprised of pyroclastic cones and flows. The age of this formation has been estimated at < 0.45 Ma and it typifies

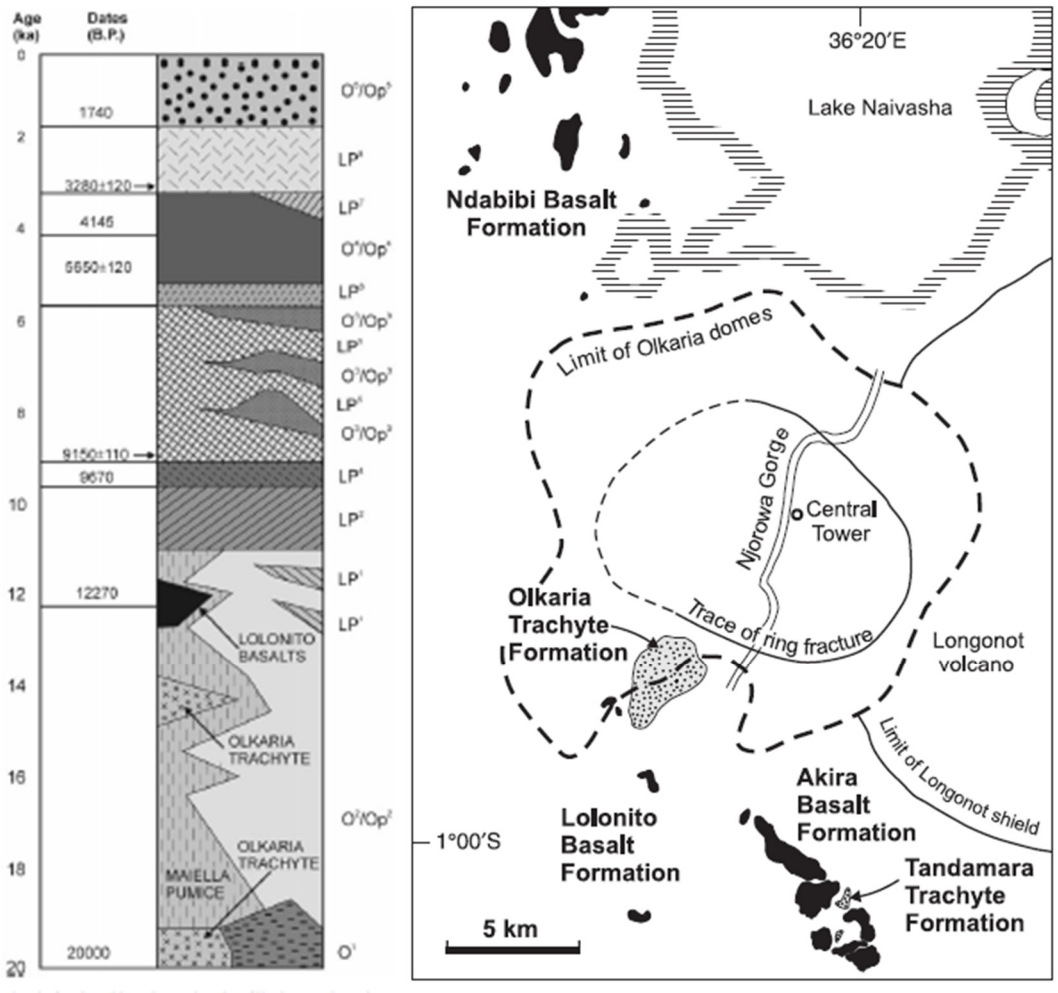

FIGURE 7: Surface formations and stratigraphic column of Olkaria volcanic complex. Also shown are a series of eruptive peripheral mafic and trachyte formations (Macdonald et al., 2008; Marshall et al., 2009)

an early phase of the younger Akira basalt formation (Ba^2). The Tandamara trachyte formation (Tt), lying in the immediate vicinity of Akira basalt formation to the southeast, is postulated to be approximately coeval with the Akira basalt formation (Clarke et al., 1990). To the north of the domes field, there is widespread mafic volcanism associated with rhyolite emplacement on the expansive Ndabibi plains (Figure 7). The latter is a low-lying area between the OVC and the Eburru Volcanic Centre. These have given rise to the Ndabibi basalt formation (Bn), comprising primarily faulted lavas and pyroclastic cones of pre-caldera age. The age range for the Bn is uncertain, a fact attributed to some lavas having well-preserved topography and lacking vegetation, possibly suggesting that they are young. Nonetheless, some of the Bn flows are intersected by minor faults and therefore considered older.

2.2.2 Sub-surface geology

Drill cuttings from several geothermal wells have contributed valuable information to the understanding of the sub-surface strata of the Olkaria geothermal field. In particular, drilling to depths > 2000 m has provided new insights into the deep sub-surface stratigraphy of the Olkaria geothermal field by enabling detailed geological analysis of drill cuttings. The litho-stratigraphic units of the Olkaria geothermal area, as revealed by data from geothermal wells and regional geology, have been classified into six distinct groups. These groups are based on age and lithology as discussed in the following section (from the youngest to the oldest).

The Upper Olkaria Volcanics are stratigraphically the youngest unit within the complex (Omenda, 1998), dated at < 0.95 Ma. Pyroclastics and comendites are prevalent within this series with minor interbeds of trachyte and basalts (Figures 8 and 9). Rocks between the surface and ~1500 m a.s.l are part

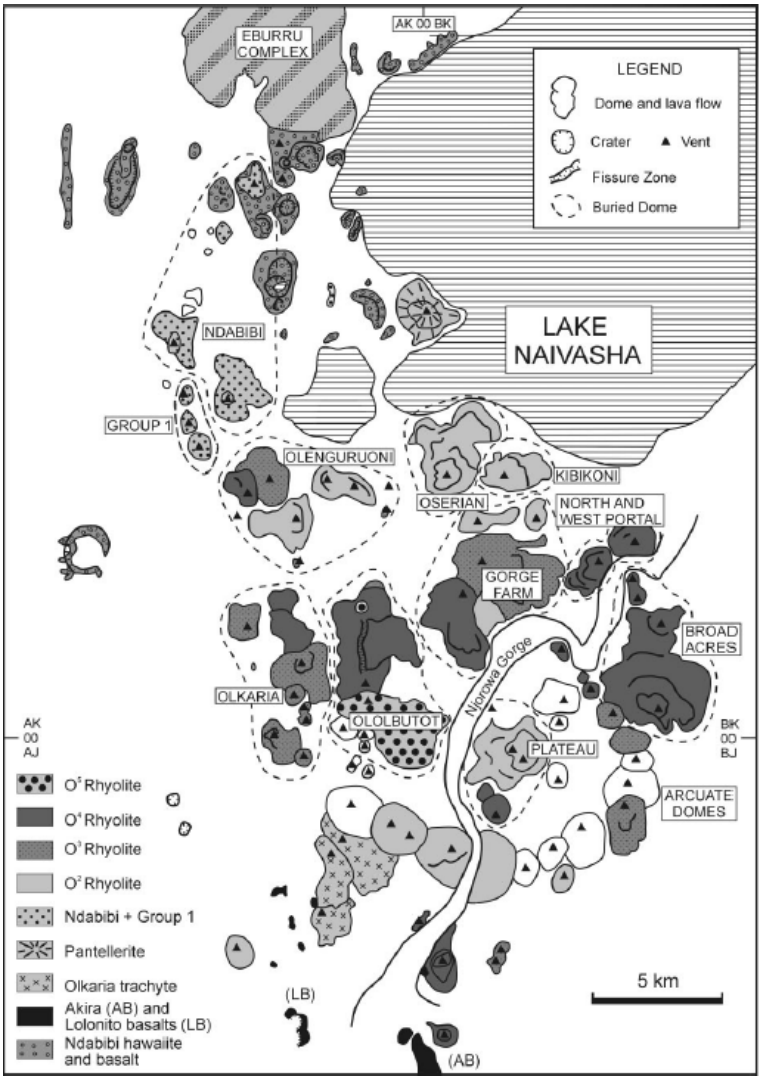

FIGURE 8: Geographical extents and stratigraphic units of the Olkaria eruptive centres. The Ol-Njorowa Pantellerite Formation (O^1) is not shown (Marshall et al., 2009)

The trachytes form part of the Kenya rift floor fissure flows which are exposed to the south and north of OVC. The formation is characterized by trachyte as the principal rock type with localized occurrence of tuffs, rhyolites and basalts. Plateau trachytes is the reservoir rock for the East, Northeast, Southeast and Domes fields. Its thickness has been estimated to be greater than 1.5 km based on borehole data from these fields (e.g., Mwangi, 2012, Okoo, 2013).

The Mau tuffs, dated between 3.4-4.5 Ma, are the oldest rocks encountered within the complex and are of unknown thickness. The formation has been penetrated by

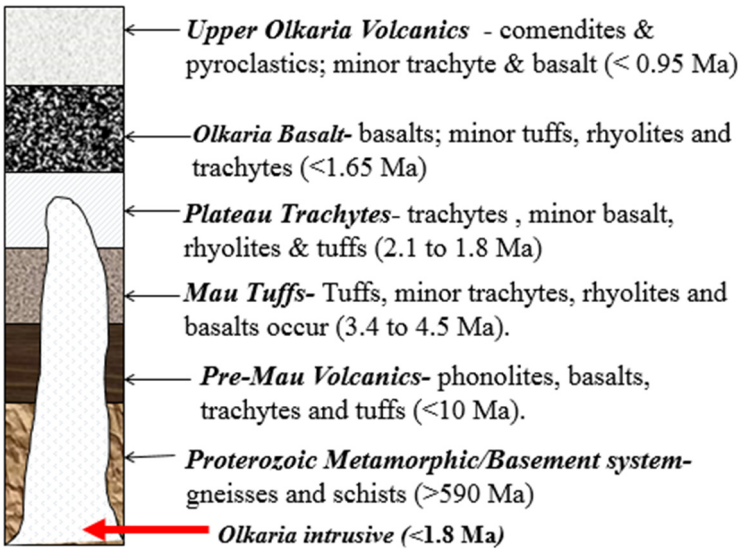

FIGURE 9: Sub-surface lithotypes of the Olkaria volcanic complex (modified from Omenda, 1998)

of this formation, the youngest being the aforementioned Ololbutot lava flow dated at 180±50 yrs ago (Macdonald and Scaillet, 2006). Moreover, the comendites forming a ring of domes east of the complex and those exposed along the Ol-Njorowa gorge belong to this series. Nonetheless, the comenditic domes have been masked by the comparatively thick pyroclastic flows deposited in the Domes field and surrounding area. Some of the deposits are believed to have originated from the adjacent Longonot and Suswa volcanoes.

The Upper Olkaria volcanics formation is underlain by Olkaria basalts. Basaltic lavas are predominant, though alternating with thin horizons of tuffs, minor trachytes and sporadic rhyolites. The formation is extensive in the East, Northeast, Southeast and Domes fields but absent in the West field. The formation has been intersected by wells at between 1900 and 1500 m a.s.l (e.g. Okoo, 2013) and forms the cap rock for the Olkaria geothermal system. Besides, the formation has been used as a marker horizon within the geothermal field, especially in the Domes field. The Olkaria basalts are preceded by plateau trachytes of Pleistocene age.

drill holes in the west fields (Northwest and Southwest), where it forms the reservoir rock. However, it has not yet been intersected by wells in the other Olkaria fields. The lithotypes constituting the Mau tuffs are composed almost exclusively of tuffs with minor interbeds of rhyolites, basalts and trachytes. Pre-Mau volcanics, dated at > 4.5 Ma constitute the fifth series and overlie the basement rock. The lithotypes in this series consist notably of phonolites, basalts, trachytes and tuffs. Underlying the Pre-Mau volcanics is a laterally extensive basement system comprising Proterozoic metamorphic amphibolite grade gneisses and schists, accompanied by marble and quartzites of the Pan-Africa basement system. This unit has been dated at > 590 Ma. The depth to the basement has been interpreted by Simiyu and Keller (2000) to be about 5-6 km in the central Kenya Rift. The apparent absence of these two units, both on the surface and within the sub-surface geological units of the Olkaria geothermal system, has been interpreted by Shackleton (1996) to be a consequence of a major graben trending N-S towards the southern flanks of the rift.

2.3 Structural geology and tectonics of OVC

Several researchers have studied and documented the distribution of geological structures in the OVC and surrounding areas since 1971 (e.g. Baker and Wohlenberg, 1971; Omenda, 1998). As mentioned earlier, the OVC is situated in the cental sector of the elliptically shaped Kenya Rift, a region marked by a sharp re-orientation in the rift's trend from a NNW alignment, to the north of the volcanic complex, to a more or less SSW direction to the south of the complex (Figure 1). Some dispute still exists regarding the explanation for the change in the rift's trend, extending for nearly 120 km before resuming a SSW course. For instance, Smith and Mosley (1993) have proposed this bend as being an intersection with a large NW-striking basement structure, the 'Aswa lineament' (Figure 1). The theory of the involvement of the basement structure has, however, been rejected by, *inter alios*, Bosworth (1987) who ascribed the shift in the rift orientation to represent an accommodation zone. The latter is taken to separate two-half grabens, the southern Magadi-Natron sub-basin and the central Nakuru-Naivasha sub-basin.

An intimate knowledge of the structural controls and their topological relationships in the OVC is instrumental in determining the reservoir fluid flow at depth, and consequently, in well siting. The determination of breccia zones associated with faults that could act as channels for geothermal fluids is of key importance. According to Steiner (1977), some faults have proved to be productive and serve as efficient conduits for the ascent of geothermal fluids, while others are known to be totally unproductive. Geological structures, especially faults and fractures, in the Olkaria geothermal system obviously play a significant role by serving as pathways for the geothermal fluids. Hence, they are the primary means for efficient heat transfer from deep to shallower levels of the system. Additionally, the structures have apparently displaced some geological units within the geothermal system, as witnessed, for example, by the presence of the Mau tuffs in Olkaria West field but lacking in wells in the East field. The structures in OVC are divided into rift faults, ring structure, Ol-Njorowa gorge, and dyke swarms (Figure 10).

The structural domains of the OVC are dominated by NE-SW and NW-SE striking faults, and subordinate N-S, NNE-SSW and ENE-WSW structural trending patterns (Figure 10). Other faults of variable orientation, though limited, also occur in the area and are not included in the structural map. Faults are more conspicuous in the East, Northeast and West Olkaria fields. However, their presence on the surface in the Domes area is severely limited by the substantial blanketing of the surface geology by thick, younger pyroclastic deposits (Otieno et al., 2014). The oldest faults of the complex are the NW-SE (e.g. Gorge farm fault) and ENE-WSW (e.g. Olkaria fault zone) trending faults (Omenda, 1998), and are associated with the rift formation (~30-45 Ma). The most recent fault systems, i.e. the N-S, NE-SW and NNE-SSW trending ones, are considered to be of a different structural regime and are thus interpreted to be associated with later tectonic activities, and perhaps, the proposed caldera collapse. The most obvious of these structures are the Olkaria fracture and Ololbutot fissure (Figure 10). The trace of the latter is revealed by extensive hydrothermal manifestations (mainly fumarolic activity), characterized by deposits of kaolinite and silica. This fault has obviously an impact on the vertical permeability witnessed along the N-S trend (Mungania, 1999).

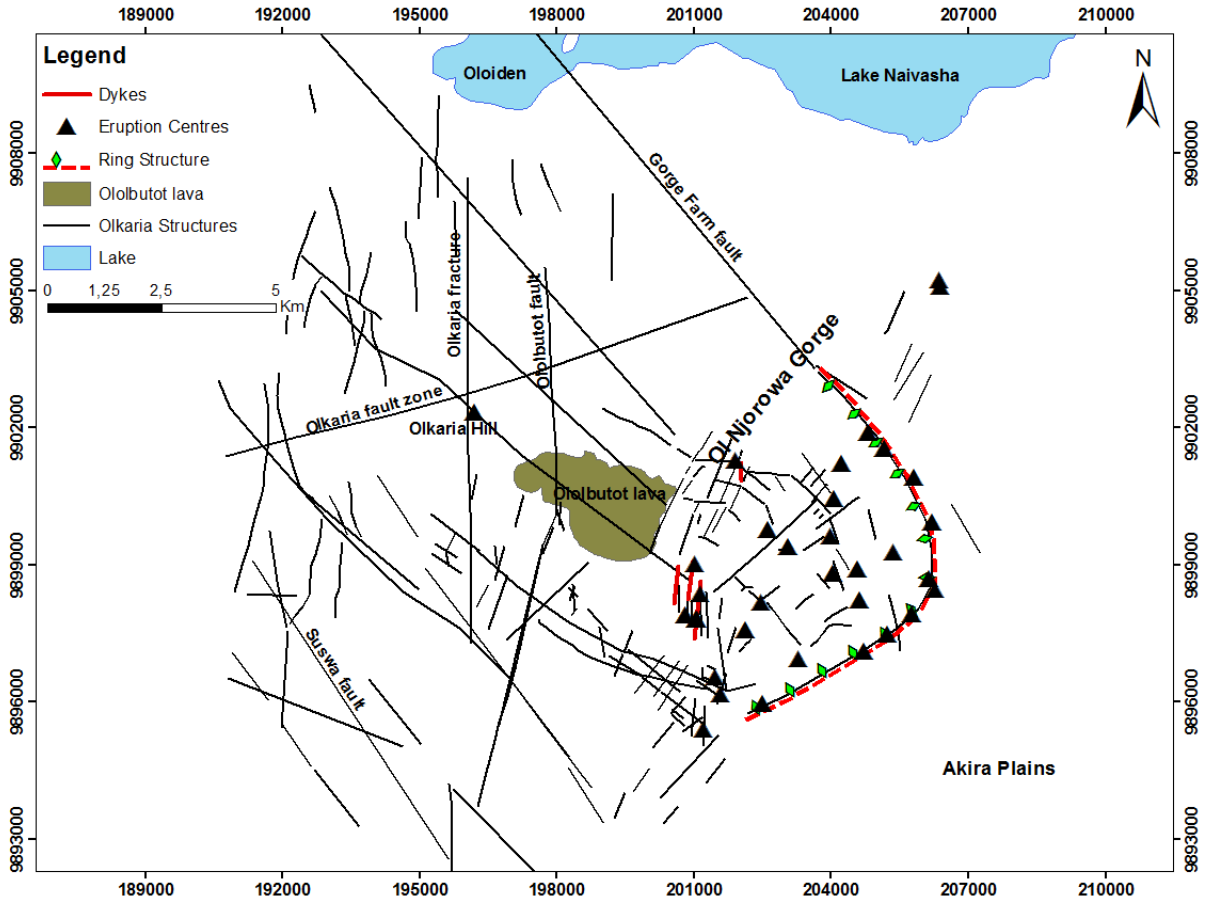

FIGURE 10: Structural map of the Olkaria Volcanic Complex displaying the orientation of various fault patterns (modified from Omenda, 1998)

Surface geothermal activity in Olkaria coincides with fault arrays. Prominent manifestations, notably, hot springs, fumaroles and altered grounds, display a strong relationship with the tectonic lineaments in the area. The Ol-Njorowa gorge, an erosional channel extending for ~16 km in total length, has been dated at about 9 ka BP (Clarke et. al., 1990). It is aligned roughly in a NE-SW direction and marks the boundary between the East and the Domes fields (Figure 10). Studies by Clarke and co-workers (1990) suggest the gorge to be a product of faulting and was later deepened by catastrophic southward overflow of Lake Naivasha when the lake level was much higher than at present. Numerous felsic dykes trending NNE-SSW and volcanic plugs (necks) are widely distributed along the gorge, strongly suggesting that faulting played a key role in its initiation (Otieno et al., 2014). Further evidence is provided by the active, boiling fumaroles, possibly attesting to reactivation of some of the faults along the gorge.

The arcuate alignment of rhyolitic domes in the eastern and south-eastern parts of Olkaria has been interpreted by Omenda (1998) to indicate the presence of a buried caldera. In his hypothesis, he proposed the arcuate alignment of rhyolitic domes and ridges to be products of a resurgence. Perhaps a more plausible explanation is that the ring structure resulted from magmatic stresses in the Olkaria magma chamber (Omenda, 1998). Nonetheless, there is no overwhelming evidence for any of the many possible explanations. As highlighted earlier, the exposure of geologic surface structures is limited in the Domes area and its immediate vicinity due to the cover of the surface by pyroclastic deposits. Most of the structures in this area are sub-surface and have been deduced through surface mapping along the deep gullies and well drilling operations. Evidence for buried faults, has been found through stratigraphic correlation of wells (e.g. Lagat, 2004) owing to the presence of excellent marker beds (Figure 9). Cave-ins and total loss of circulation returns during drilling operations, for instance in well OW-915B (KenGen, 2012), have also served as a clear indicator for the existence of sub-surface fault structures.

2.4 Hydrogeological setting

The hydrogeology of OVC, and to a greater extent the surrounding volcanic centres (i.e. Eburru, Longonot and Suswa) within the central sector of the KRS, is controlled primarily by the rift faults. Tectonic movements of the rift undoubtedly played a pivotal role both on a large-scale, by forming the regional faults, and on a small-scale, by creating the local fracture systems of enhanced permeability. These faults and fracture systems act as permeable pathways by channelling lateral groundwater flow from the recharge areas into the low-lying geothermal systems along the rift axis. Ordinarily, faults have the capacity to propagate fluid flow by providing zones of high permeability. Likewise, faults may simultaneously offset zones of relatively high permeability (Allen et al., 1989), in which case they cause compartmentalization of lateral flow.

Recharge into the geothermal field at Olkaria is exclusively of meteoric origin (Ojiambo and Lyons, 1993), derived from high altitude precipitation at the rift escarpments (Mau escarpment to the west and Kinangop plateau to the east) (Figure 11). The two highlands have a maximum elevation of 3080 m and 2740 m, respectively, and experience an annual rainfall of between 1200-1500 mm. On the other hand, Olkaria geothermal field and its environs receive an estimated average annual rainfall of about 826 mm (Allen et al., 1989). The structures controlling deep recharge within the system are the NW-SE and NNW-SSE trending faults (Figure 10). As previously reported (Ambusso and Ouma, 1991), the rejuvenated pre-Pleistocene, ENE-WSW trending Olkaria fault zone (Figure 10) is a major structural divide transecting the Northeast and West fields. Therefore, it is regarded as an important structure forming a hydrologic divide within the geothermal system. This, for instance, has been demonstrated by the presence of a liquid-dominated reservoir without a steam cap in the north and a liquid dominated two-phase reservoir overlain by a steam cap in the south of the fault (Ambusso and Ouma, 1991). Some water from the recharge areas also enters the Olkaria geothermal system through the late-Pleistocene, relatively young, tectonically reactivated N-S faults and fractures (e.g. Ololbutot fault and Olkaria fracture zone, respectively). These structures control the axial groundwater movement through the geothermal system, though have a shallower influence in comparison to the major rift faults that offer deep recharge (Omenda, 1998).

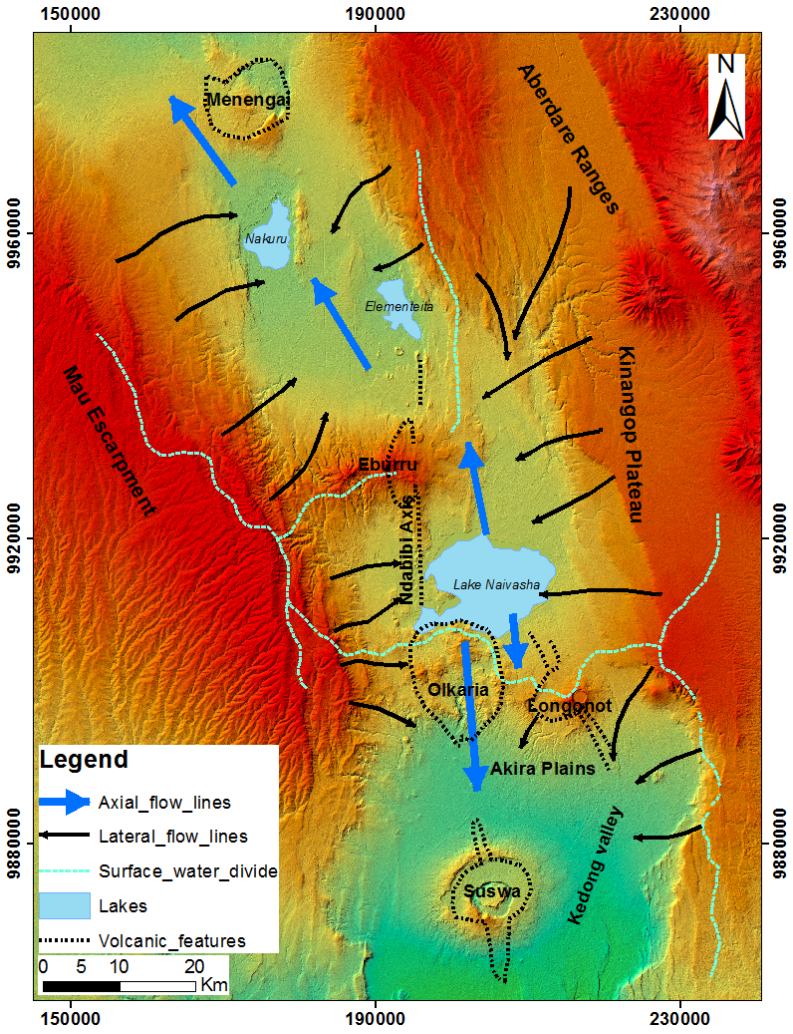

FIGURE 11: Piezometric map showing reservoir recharge areas for Olkaria and other surrounding geothermal fields along the rift axis (modified from Allen et al., 1990)

Other features which have been noted to enhance fluid flow within the Olkaria system, and, to a larger extent in the Domes area, are lithological interfaces and, jointed and fractured lavas. Similarly, stable isotope studies have been employed (e.g. Nkapiani, 2014) to determine the origin of thermal waters and the reservoir recharge areas of the Olkaria geothermal system. Based on hydrogen isotope studies, the reservoir fluid isotope composition of the thermal waters indicates two potential recharge zones for the system; the eastern rift flank ($\delta D = \sim$-24‰) and the western rift flank ($\delta D = \sim$-30‰). Results of hydrogen isotope determinations suggest the West, East and Northeast fields to be recharged by waters from the western escarpment. The Domes field obtains recharge largely from the eastern rift wall (Nkapiani, 2014). Whether or not sub-surface drainage from Lake Naivasha contributes to recharge of the Olkaria geothermal system has intrigued many researchers and is still a subject of debate (e.g. Allen et al., 1989).

2.5 Reservoir properties of Olkaria field

In this section, attention is focused principally on the most important features of the reservoir system of the Olkaria geothermal field. A comprehensive review of all the aspects of reservoir characteristics of the Olkaria geothermal field is beyond the scope of a single sub-section. The Olkaria geothermal reservoir has developed as a consequence of the OVC. Presently, the geothermal system supports ~654 MWe (installed capacity) through power stations operated by KenGen and Ormat Technologies (OrPower) (Table 1). It is a two-phase liquid dominated system overlain by a comparatively thin steam-dominated zone, ranging from 100 to about 200 m in thickness at 240^{o}C. The hydrogeological features of the field are distinguished by four up-flow zones in the general area. Extensive fluid circulation in the field is controlled by major faults and fracture zones as discussed earlier. The ultimate heat source of the system has been attributed to a deep-seated magma chamber, which peaks in several locations in the form of three main intrusions, possibly partially molten. Based on seismic studies by Simiyu and Keller (2000), the intrusions extend to shallower levels, approximately 6-8 km, and are suggested to lie beneath Olkaria Hill, Gorge Farm volcanic centre and in the Domes area. Temperature and pressure models supports this observation and, have identified four main up-flow zones related to these heat sources (Figure 12) (Mannvit Consortium, 2011).

The first up-flow zone feeds the Olkaria west fields and is linked to the Olkaria Hill (Figure 2) heat source body. The second up-flow zone, feeding the Northeast and East fields as well as the northwest corner of the Domes field, is connected to the heat source beneath the Gorge Farm volcanic centre (Figure 8). The final up-flow zone, associated with the ring structure, is visible in the southeast corner of the Domes field and is linked to the heat source suggested beneath the area. Reservoir chemistry data support the existence of the up-flow zones as defined by relatively high Cl^- concentrations and high Na/K temperatures within these zones (Mannvit Consortium, 2011). Above the steam zone, basaltic rocks, and to a lesser extent trachytes, form an impermeable caprock, subsequently marking the top of the reservoir. This proposition has been supported by reservoir modelling (Ambusso and Ouma, 1991), which reveals sharp temperature increases below this formation. The depth to the caprock, however, varies from one sub-field to another, but in many instances lies between 1900 and 1300 m a.s.l, as revealed by several stratigraphic correlations (e.g. Okoo, 2013; Mwania et al., 2013). The bulk of the reservoir rocks, save for in the West fields, are trachytes of Pleistocene age with well-developed fractures. The vertical extent of the reservoir is quite uncertain and varies from one sub-field to another. Ambusso and Ouma (1991) have suggested it to be of the order of several hundred meters. However, the presence of extensive intrusive bodies (e.g. syenite, granite, etc) at greater depths (e.g. below 2500 m) probably indicates proximity to the bottom of the reservoir.

2.6 Summary of drilling history

Well OW-922 is a vertical well drilled to a total depth of 2990 m from the cellar top (CT), to the east at approximately 2.5 km from the proposed ring structure. The well was spudded on 16th of April and completed on 19th of September, 2014, after a period of 156 days. This translates to 101 more days than planned, since the well had initially been expected to be completed on 12th June, 2014. The drilling stages comprised the surface, intermediate and production hole as well as a production section. Delays

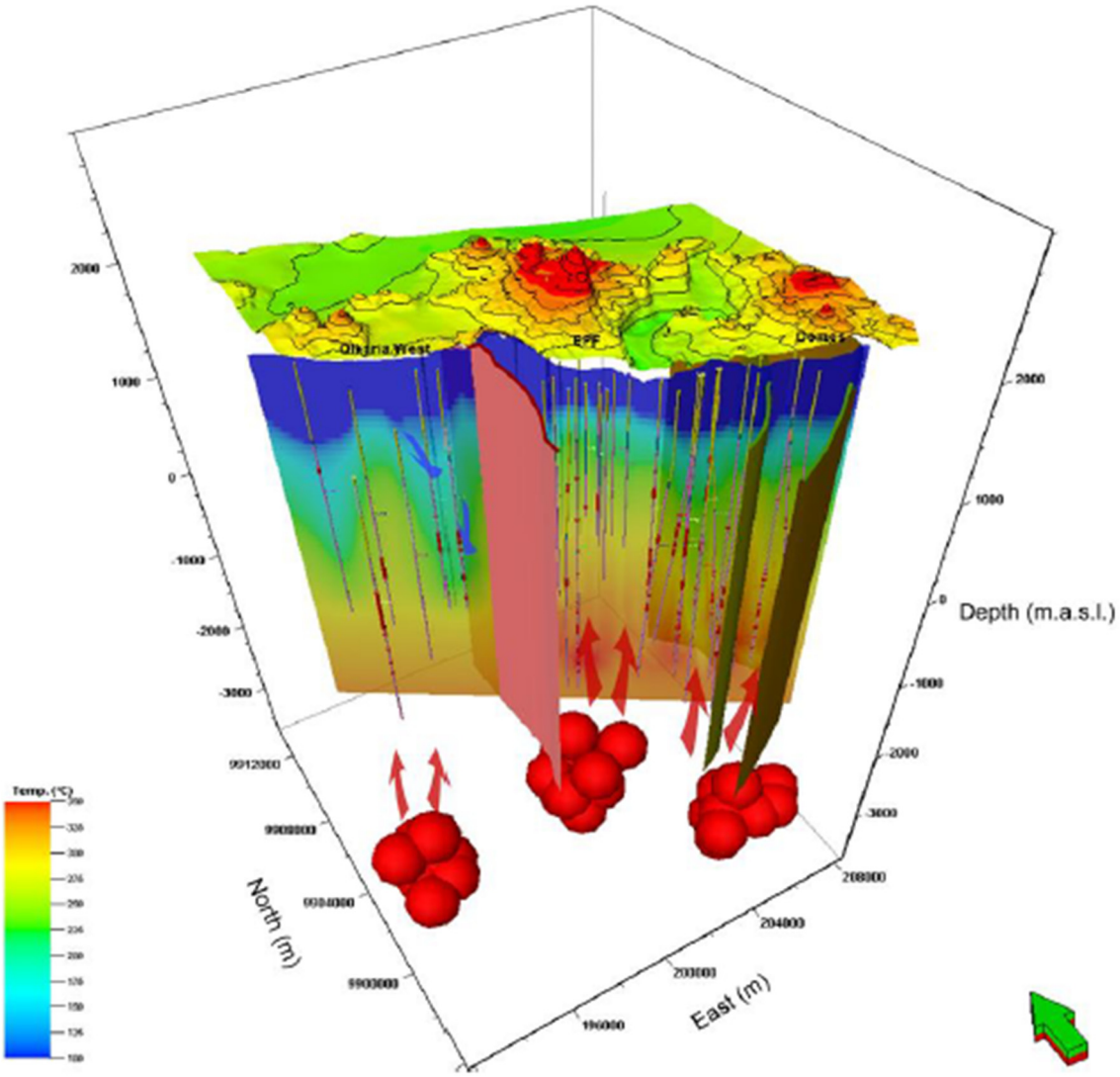

FIGURE 12: A vertical schematic sketch of the conceptual model of Olkaria geothermal system. The suggested heat sources, up-flow zones and temperature cross-section are shown. The green arrow is directed north (Mannvit Consortium, 2011)

in the drilling were occasioned by various challenges as outlined in the description of different phases. Casing depths were measured from the flange. A summary of the drilling phases and casing design of well OW-922 is illustrated in Table 2 and the drilling progress is shown in Figure 13.

TABLE 2: Drilling phases and casing design for well OW-922

Drill rig	Stage	Hole diameter (")	Depth (m)		Casing	
			From	To	Casing diameter (")	Type
GWDC-116	Phase 1	26	0	58	20	Surface
	Phase 2	$17^{1}/_{2}$	58	300	$13^{3}/_{8}$	Anchor
	Phase 3	$12^{1}/_{4}$	300	1200	$9^{5}/_{8}$	Production
	Phase 4	$8^{1}/_{2}$	1200	2990	7	Slotted liners

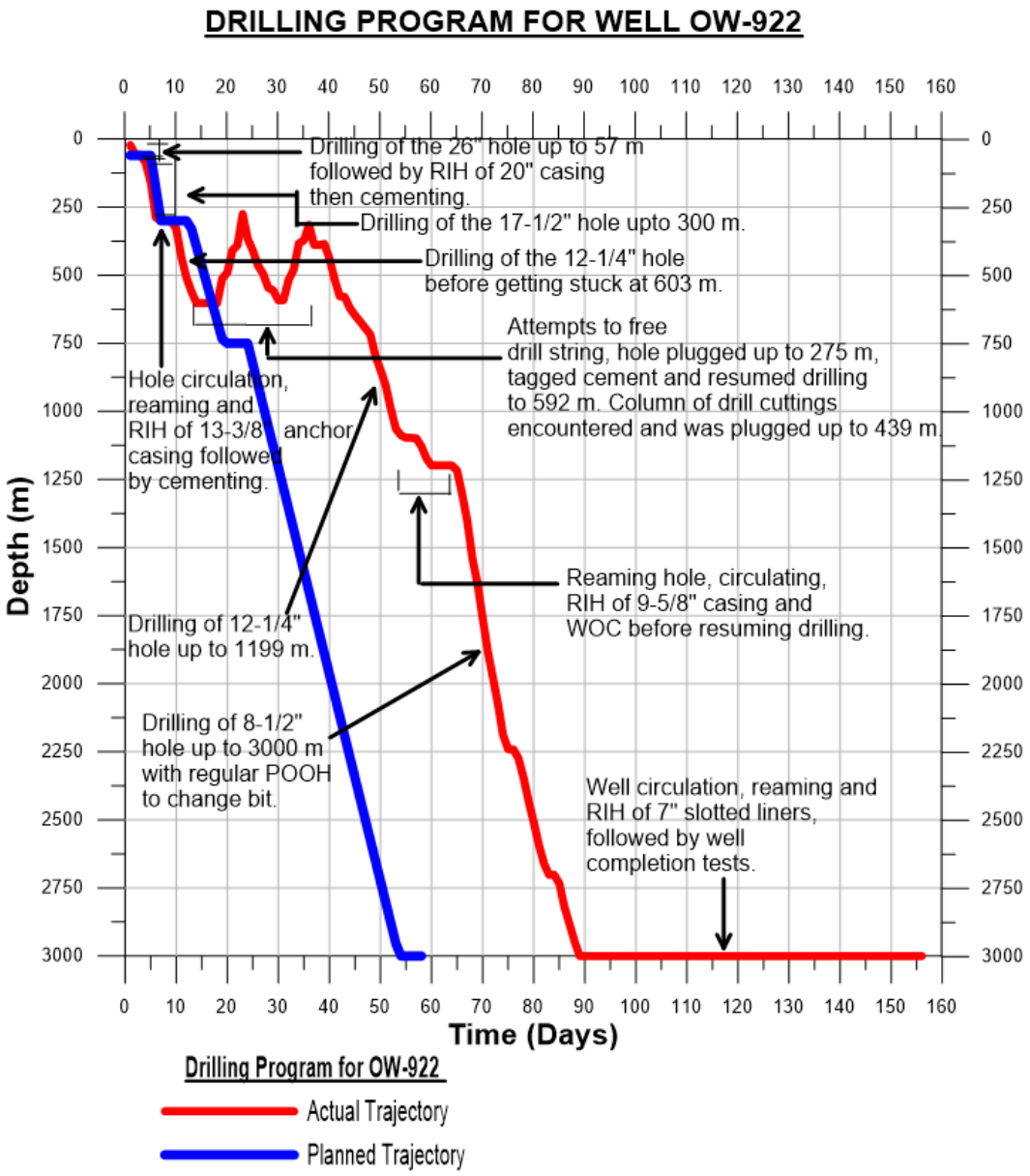

FIGURE 13: Drilling progress curve for well OW-922 (KenGen, 2014)

2.6.1 Phase 1: Drilling of the surface hole

Surface hole was drilled with a 26" roller cone milled tooth bit using high-viscosity bentonite based-mud to a depth of 58 m rotary kelly bottom (RKB). Full circulation returns occured at the surface throughout the drilling of this phase. The well was circulated to the bottom and no obstructions were detected. It was cased using a 20" outside diameter (OD) surface casing. Casing shoe was set at 57.1 m RKB and the casing column successfully cemented. This phase lasted 4 days.

2.6.2 Phase 2: Drilling of the intermediate hole

Drilling of phase 2 started on 20th April, 2014 using a $17^{1}/_{2}$" roller cone bit with aerated water and foam as the drilling fluid. Like during the drilling of the surface hole, full circulation returns were received on the surface down to the section total depth (TD) of 300 m RKB. The hole was circulated before the $13^{3}/_{8}$" anchor casing was run in hole (RIH) and casing shoe set at 299.19 m RKB. The casing column was cemented in place in three stages; the primary cementing and two backfills. Drilling of this phase was completed in 6 days.

2.6.3 Phase 3: Drilling of production hole

Drilling of this phase began on 26th April, 2014 with the use of a $12^{1}/_{4}$" roller cone bit. Drilling progressed reasonably well with aerated water and foam being used with good circulation returns realized at the surface. However, several unusual events occurred. On 29th April, the drill string got stuck at a depth of 603 m RKB. Several attempts to free the string, including pumping a mixture of PIPE-LAX and diesel, proved successful after 2 days. A decision was then made to pull out of hole (POOH) and inspect the drill strings, before RIH to continue drilling. Further attempts to proceed with drilling proved futile due to a second obstruction encountered at 520 m RKB. At this point in time, the well condition had become complicated. The crew embarked on reaming the wellbore from surface to bottom with aerated water and foam, receiving no circulation returns at the surface. This was done in an attempt to clear any obstructions along the well course.

While reaming almost reaching the bottom (603 m RKB), the drill string got stuck once again. Efforts to free the string were immediately initiated. This was on 1st May, 2014. To overcome this impediment, a decision was made to carry out a plug job. A total of 24 plug jobs were conducted around this section. The decision proved successful and the section was finally by-passed. Normal drilling commenced again on 29th May, with the use of mud and progressed smoothly to TD of 1200 m RKB. Circulation of the wellbore and a wiper trip were undertaken without any considerable challenges. RIH of the $9^{5}/_{8}$" OD production casings followed and the casing bottom was set at 1197.86 m RKB. The casing column was then cemented in place in three stages; the primary cementing and two backfills. Drilling of this phase lasted 55 days.

2.6.4 Phase 4: Drilling of production section (Main hole)

Drilling of the production section resumed on 20th June, 2014 with the use of a $8^{1}/_{2}$" roller cone bit, with aerated water and foam as the drilling fluid, resulting in intermittent circulation returns. Drilling progressed without any major hindrance before an obstruction was encountered at 1359 m RKB. This was successfully overcome after 1 day of reaming, and drilling continued smoothly with excellent circulation returns. On 8th July, (84th day) a tight hole was encountered at 1280 m RKB while RIH with a new drill bit. A decision was made to ream the wellbore with aerated water and foam before resumption of drilling, which proved fruitful. The final depth of 3000 m RKB was achieved on 13th July, 2014 (89th day). The crew embarked on circulation to unload the wellbore before RIH hole the 7" perforated liner. However, an obstruction was once again encountered at 1270 m RKB while conducting wiper trip prior to POOH and further reaming followed.

A possible reason for the development of obstruction between about 1200-1360 m RKB was thought to be the presence of swelling clays. XRD analysis (Appendix B) confirms the occurrence of swelling clays around this section. After a wide consultation, a decision was made to pump a mixture of 1.75 tonnes of sodium hexametaphosphate [$(NaPO_3)_6$] (a dispersant) and 10m^3 of water into the wellbore to help break the clay bonds. This proved successful. Eventually, the wellbore was successfully reamed to the bottom using aerated water and foam, receiving full circulation returns at the surface. A wiper trip was conducted and the drill string pulled out of the hole before the 7" slotted liner and 2 plain liner pipes were RIH and squatted at the bottom. This phase lasted 91 days.

3. SAMPLING AND ANALYTICAL METHODS

3.1 Sampling

Studies of various parameters in borehole geology require comprehensive and accurate sampling. The information obtained depends on the samples quality. Consequently, a systematic selection of samples is indispensable. Principally, this study involves sampling of drill cuttings (chips), measurements at discrete depths and laboratory analyses. Drill cuttings analysis is basically a visual method of semi-quantitatively describing the host rock characteristics from drill cuttings obtained during a drilling operation. The analyses are crucial in constraining the sub-surface conditions of the geothermal system (Reyes, 2000). These encompass, but are not limited to, lithostratigraphy, hydrothermal alteration rank and intensity, permeability, petrochemical characteristics and zonation patterns.

Unlike in the case of core samples, interpretation based on drill cuttings analysis is not without a fair share of its challenges, including imprecise sample location as a consequence of relatively large lag times. In other words, drill cuttings do not represent exact horizons, but a limited depth range. The time taken by drill cuttings to get to the surface is dependent on the type of circulation fluid, drillhole diameter, flow rate and circulation loss. In addition, chances of collecting unrepresentative samples caused by sample mixing as a result of drilling through soft formation are quite high. Further, grinding of cuttings to extremely fine grains (almost powdery) by the drill bit leads to loss of essential geological features. No cores were collected in well OW-922. Therefore, all the descriptions and interpretations in the present study are based solely on the analysis of drill cuttings. Uncertainty in sample depth does not substantially affect the conclusions reached in this study. Cuttings were collected at 2 m interval, except in cases of partial circulation returns. In such cases, it was carried out at 4 m interval. The sampling intervals along with total loss zone depths were constantly recorded in the rig geology notebook.

3.2 Analytical methods

To achieve the specific objectives of this study, several analytical techniques have been employed as discussed in a following section. The procedure and a summary of the analytical results obtained are presented in different appendices.

3.2.1 Binocular microscope analysis

The main parameters described by binocular microscope analysis include colour of the rock, grain size, rock fabrics, primary/original mineralogy, hydrothermal alteration rank and intensity, rock type and features that point to the possible occurrence of feed zones or intrusions. Samples were scooped up using a petri dish and washed to enhance visibility and reveal any obscured features. Binocular microscope analysis for this study was carried out at Iceland Geosurvey (ÍSOR) petrography laboratory using an Olympus, SZX12 binocular microscope. A detailed description of the lithology is presented in Appendix A.

3.2.2 Petrographic microscope analysis

With this analytical technique one can ascertain in much finer details the rock type and hydrothermal alteration grade based on the optical properties of minerals. Hydrothermal alteration intensity, paragenetic sequence and some other features not obviously discernible under the binocular microscope can be described in detail. A total of 70 thin sections were analysed at the University of Iceland petrographic laboratory, using, an Olympus BX51 and Leitz Wetzlar petrographic microscopes with a magnification range of between 4× and 50×.

3.2.3 X-ray diffraction analysis

The X-ray diffraction (XRD) analysis technique is concerned primarily with structural aspects of clay minerals and other minerals (e.g. zeolites, amphiboles, etc.). The diffractometry analysis is based on the

principles of Bragg's law. When a beam of X-rays is passed through a particular mineral and certain geometric conditions are achieved (Yoshio et al., 2011), the X-rays scattered from the crystalline sample can undergo constructive interference, thus producing a diffraction peak. A diffraction pattern (made by the diffractometer) records the X-ray intensity as a function of 2θ (incident angle of the X-rays) which is characteristic of a specific mineral. In this study, a total of 105 samples were analysed exclusively for clay minerals at the KenGen XRD laboratory. A summary of the XRD analytical results are presented in Appendix B.

3.2.4 Inductively Coupled Plasma-Optical Emission Spectrometry (ICP-OES) analysis

The ICP-OES method has today become a valuable tool for quantitative elemental analysis. The basic principle behind the method is that atoms of an analyte emit electromagnetic radiation at certain characteristic wavelengths when atomized (Rollinson, 1995). The wavelengths of the light emitted are then separated and measured in a spectrometer. This yields an intensity measurement that can be easily converted to an elemental concentration by comparison with calibrated reference standards (Rollinson, 1995). Actual analysis involves spraying the sample solution into the core of an inductively coupled argon plasma, generating temperatures of approximately 7,000-10,000 K. At such high temperatures, all analyte species are atomized, ionized and thermally excited, and can then be detected and quantified with an optical emission spectrometer (OES). The extremely high temperature ensures that the sample matrix does not produce any interfering components that might interfere with the analysis.

For this study, a total of thirty homogeneous samples from the study well were analysed for major and trace elements using the Spectro Ciros 500 ICP-OES equipment at the Faculty of Earth Sciences, University of Iceland. The major element oxides analysed are SiO_2, Al_2O_3, FeO, MnO, MgO, CaO, Na_2O, K_2O, TiO_2 and P_2O_5. Trace elements analysed include, Ba, Co, Cr, Cu, La, Ni, Rb, Sc, Sr, V, Y, Zn and Zr. Samples were analysed using the following USGS internationally recognized standards and error margins; (1) Basalts: multiple measurements of standard Basalt, Hawaiian Volcano Observatory (BHVO)-1 2σ (external reproducibility). Analysis for Si, Al, Fe, Mn, Mg, Ca, Na and P was done with 2σ <1.8%. The error margin for trace elements in basalts ranged between 4-8%, (2) Rhyolites: measurements of standard Rhyolite, Glass Mountain (RGM)-1. Elements were analysed with 2σ values as follows; Si and Mg ~ 1%, Ti <2%, Al, Ca, Fe, Na and K <4-6%, Mn and P <8%. The error margin for trace elements in rhyolites is the same as for basalt. A detailed description of the ICP-OES procedure for sample preparation, instrument set-up and data processing, is presented in Appendix C. Full analytical results are listed in Table 5.

3.2.5 Electron microprobe analysis

Electron microprobe (EMP) analysis is routinely used for characterizing the compositions and compositional variations of minerals within rock samples. The basic theory of EMP analysis relies on the production of electrons and X-rays during the interaction of the incident electron beam with the specimen (Schiffman and Roeske, 2014). Consequently, with the electron beam focused on a small area on a sample surface, characteristic X-rays are generated for qualitative or quantitative analysis at micrometre-scale spatial resolution. The volume of the electron-matter interaction varies directly with the accelerating potential of the electron beam (Schiffman and Roeske, 2014) and inversely with the mean density of the sample. Two key processes, namely, the generation of backscattered electrons and the generation of characteristic X-rays, are responsible for producing the main signals utilized in EMP analysis.

A total of 10 samples from the four wells (OW-905A, 910, 917 and 922) were selected for analysis of secondary minerals of interest. These represent four samples containing epidote and six samples containing chlorite. The cuttings were subsequently moulded in epoxy, polished, carbon coated and analysed using a JEOL JXA-8230 electron microprobe located at the Institute of Earth Sciences, University of Iceland. Elements analysed and the conditions under which the probe was run are described in Section 4.9. Prior to quantitative analysis with the electron microprobe, the minerals of interest, namely, chlorite and epidote, were first studied with a Hitachi TM 3000 Scanning Electron Microscope (SEM). Results for EMP analysis for chlorite and epidote are presented in Appendix D.

4. RESULTS

4.1 Lithology of well OW-922

Knowledge of the sequence, nature and architecture of the stratigraphy is of paramount importance for understanding the geothermal system around well OW-922. Analyses based on binocular and, petrographic observations and ICP-OES have revealed eight types of lithologies intersected by well OW-922. These comprise pyroclastics, tuffs, rhyolite, basalt, basaltic trachyandesite, trachyte, trachydacite and trachyandesite. No intrusions were intersected by the well. A description of all the lithological units encountered in the well are discussed below and presented in Figure 14. However, a detailed description of the various units and intervals of occurrence along the well profile is presented in Appendix A.

4.1.1 Pyroclastics

The pyroclastic formation is a member of the Upper Olkaria Volcanics according to the OVC stratigraphical classification scheme. The unit occupies the uppermost 302 m of the well column. The formation generally varies in colour from light grey to yellowish-brown, comparatively heterogeneous and indurated deposits dominated by ash-sized particles, volcanic glass, scoria, highly vesicular pumiceous and tuffaceous fragments. It is oxidized in all cases. The yellowish-brown unit are pyroclastics from Olkaria, whereas the light grey to grey in colour counterparts are pyroclastics derived from Longonot volcano. Longonot pyroclastics extend from the surface to ~ 96 m depth, whereas, Olkaria pyroclastics, derived from the early post-caldera activity (Op^2) are observed between ~ 190 and 302 m depth.

4.1.2 Tuffs

Tuffs in the well occur predominantly as interbeds and intercalations between lava flows, marking different eruption episodes. The units range in thickness between 2 and 52 m. Two distinct tuff varieties have been recognized in the well, lithic and glassy (vitric) types. The former is the dominant, varying in colour from light grey, grey to brown and, occasionally, pale green. The latter is due to alteration. Trachytic and basaltic fragments are the most common crystalline fragments, and are embedded within the lithic matrix. The phenocryst phases observed in optical petrography are quartz, sanidine and augite. Moderate to high vesicularity is a common feature of these tuffs, with majority of the vesicles being irregular in shape. Vesicles are filled by alteration minerals, primarily zeolites and chalcedony. Lithic tuff was noted occuring between 302-350 m, 362-364 m, 408-422 m, 476-498 m, 564-582 m, 726-744 m, 952-966 m, 1440-1600 m and 1600-1642 m. Vitric tuff, on the other hand, was only observed between 1260-1312 m. The vitric tuff is white in colour, and has a glassy matrix as observed under the petrographic microscope, with minor sanidine and quartz phenocrysts. Generally, the tuffs display moderate to high intensity of alteration, particularly in the basal rubble (contacts).

4.1.3 Rhyolite

The rhyolite encountered in this well is of granular type and ranges in colour from light grey to grey to pink. It is massive, holocrystalline, and generally sparsely to moderately phyric. Also, it is hard, probably due to intense silicification. The matrix has commonly quartz porphyries and subordinate sanidine phenocrysts. Small mafic mineral grains are disseminated in the aphanitic groundmass and have been proved through optical petrography to be riebeckite and oxides, probably magnetite. The formation is not extensive in the study well as compared to that observed in wells drilled along and within the proposed caldera structure. It is restricted to depths between 1046-1150 m, 1214-1224 m, and 2370-2592 m. Based on petrochemical data, the rhyolite is silica-rich with SiO_2 content ranging between 69 and 73 wt.%.

4.1.4 Basalt

The formation ranges in colour from dark grey to brown, with the brown varieties depicting high intensity of hydrothermal alteration. The dark grey basalt is fine grained and holocrystalline as observed between 498 and 504 m, 1198 and 1214 m and 1642 and 1654 m. In addition, it is dense and the predominant phenocryst phases are plagioclase and clinopyroxene (notably augite) as well as a large abundance of opaque oxides, mainly titanomagnetite. Olivine phenocrysts are rare and their prescence is disclosed by crystal outlines of the alteration products, e.g. calcite and chlorite. Plagioclase laths are also widespread in the holocrystalline matrix and outweigh clinopyroxene in all cases. On the other hand, vigorous alteration has completely obliterated the primary mineral phases and original texture in the brown coloured basalt. The latter occurs between 1150 and 1198 m. Nevertheless, vesicles are observed largely filled with calcite and variably green clays in both cases.

4.1.5 Basaltic trachyandesite

This rock type of intermediate composition is scarce in the well, and generally along the EARS system based on petrochemical data from previous studies (e.g. Peccerilo et al., 2007). It was identified between 1654 and 1700 m through petrochemical analysis. The rock is mostly brown to grey (probably as a result of intense alteration), though it occasionally appears light grey (e.g. between 1662 and 1666 m and between 1680 and 1682 m). It is aphyric to slightly phyric with minor plagioclase phenocrysts. Other phenocryst phases observed are amphiboles and clinopyroxenes. The latter occur characteristically as slender green needles. Mafic silicates in most cases (~ 80%) display more or less complete replacement by brown clays.

4.1.6 Trachyandesite

Like basaltic trachyandesite, this rock type is also scarce in this well and was confused for trachyte during the initial binocular analysis. The unit was identified through petrochemical analysis as occurring only between 2780 and 2784 m. The rock has a composition intermediate between trachyte and andesite and represents less fractionated magma. The notable phenocryst phases observed in thin section are plagioclase, sanidine and pyroxenes, mainly aegerine-augite.

4.1.7 Trachydacite

This unit was identified at 1700-1730 m, 2186-2210 m, 2326-2370 m and 2592-2780 m through petrochemical analysis. The rock has a composition intermediate between trachyte and dacite. The colour varies from pale grey to grey, to pink. It is aphyric to poorly phyric, and contains clinopyroxene and sanidine as the principal phenocrysts. Vesicles are rather scarce, but where present are filled by calcite, chlorite and secondary quartz.

4.1.8 Trachyte

This is the dominant lithology in the well and the main sequence is ~ 1200 m thick, as observed between 1700 and 2900 m. It is the reservoir rock of the geothermal system around well OW-922. This unit is predominantly grey, though colour ranging from pale green to brown is also noticed. In most cases, the unit is phyric with sanidine, subordinate feldspars and quartz phenocrysts as well as specks of mafic minerals such as pyroxenes and amphiboles. The pyroxenes are in many cases aegerine-augite while the dominant amphibole is dark blue riebeckite, recognised through petrographic analysis. Occasionally, the formation is observed mixed with basaltic and tuffaceous fragments (e.g. between 1248 and 1260 m and 2156 and 2292 m), suspected to have fallen from above during drilling. Trachytic texture with flow banding is a characteristic feature of these trachytes with sanidine laths aligned in a particular direction. In addition, elongated vesicles are abundant, a display of the direction of lava flow.

4.2 Hydrothermal alteration

Hydrothermal alteration is a metasomatic process involving recrystallization of rock forming/primary minerals and deposition of secondary minerals in voids, to a new authigenic mineral assemblage due to interaction with thermal fluids. The new mineral assemblage is more stable, or at least metastable, at a specific temperature, pressure and fluid composition range within a particular geothermal system. The stability of the hydrothermal minerals is determined by their solubility and the rock dissolution process. Hydrothermal alteration involves interaction of the hot aqueous fluids with the host rock (a process popularly known as *water-rock interaction*), resulting in a change both in the composition of the fluids and the rocks (Brown, 1978). Circulation of thermal fluids through the geothermal system is a consequence of the heat generated by magma or hot crustal rocks.

During ascent to the surface along permeable structures, the thermal fluids circulating within the geothermal system directly deposit dissolved mineral constituents in vesicles, vugs or veins. Correspondingly, the thermal fluids dissolve ions from the host rocks, consequently forming secondary minerals. By observing alteration overprints or the sequences of hydrothermal minerals deposited in the veins or vugs, it is possible to unravel the prevailing reservoir temperature, permeability and fluid composition (Reyes, 2000). According to Mielke et al. (2015), hydrothermal alteration is defined by both its grade and intensity. The term grade implies a definite assemblage of hydrothermal minerals present. Intensity of alteration, on the other hand, defines whether the alteration is incipient, partial, or complete. Accordingly, alteration is described using qualitative terminology such as low, medium, or high, depending on if a primary constituent is incipiently, partly, or completely altered in that order (Reyes, 2000).

Formation of hydrothermal minerals is generally dependent on the temperature, pressure, reservoir permeability, protolith, fluid composition (especially pH), and duration of fluid-rock interactions (Brown, 1978). Although pressure has little direct effect on hydrothermal alteration, an important aspect is that it controls the depth at which boiling occurs, and thus separation of vapour and gases. Some of these factors listed are so intimately interconnected that, at first sight, it is often impossible to separate one from another (Brown, 1978). Products of hydrothermal activity in the geothermal system in the vicinty of well OW-922 occur both as replacement of unstable primary components or glassy matrix of the rocks (Table 3) and as open space fillings in veins, fractures, and vesicles.

TABLE 3: Alteration of primary minerals and order of replacement in well OW-922 (adapted from Brown, 1984)

Order of replacement	Susceptibility	Primary phases	Alteration products
↓		Volcanic glass	Clays, calcite
		Olivine	Clays, chlorite, calcite, quartz
		Plagioclase	Albite, clays, zeolites, calcite
		Pyroxenes, amphiboles	Clays
		Sanidine	Adularia, clays, calcite
		Fe-Ti oxides (opaques)	Titanite, pyrite, haematite

4.3 Distribution of hydrothermal alteration minerals

Hydrothermal alteration minerals in well OW-922 were observed to occur both as replacement of primary minerals, and as deposition as veins and as fracture and vesicle fillings. The distribution of alteration minerals in well OW-922 was determined with binocular, petrographic and XRD analyses. The main hydrothermal minerals encountered in the well include: zeolites (mesolite, scolecite and wairakite), chalcedony, haematite, titanite, calcite, albite, pyrite, clays (smectite, illite, chlorite and mixed-layer clays (MLCs)), quartz and epidote. This is presented in Figure 14 and discussed further below.

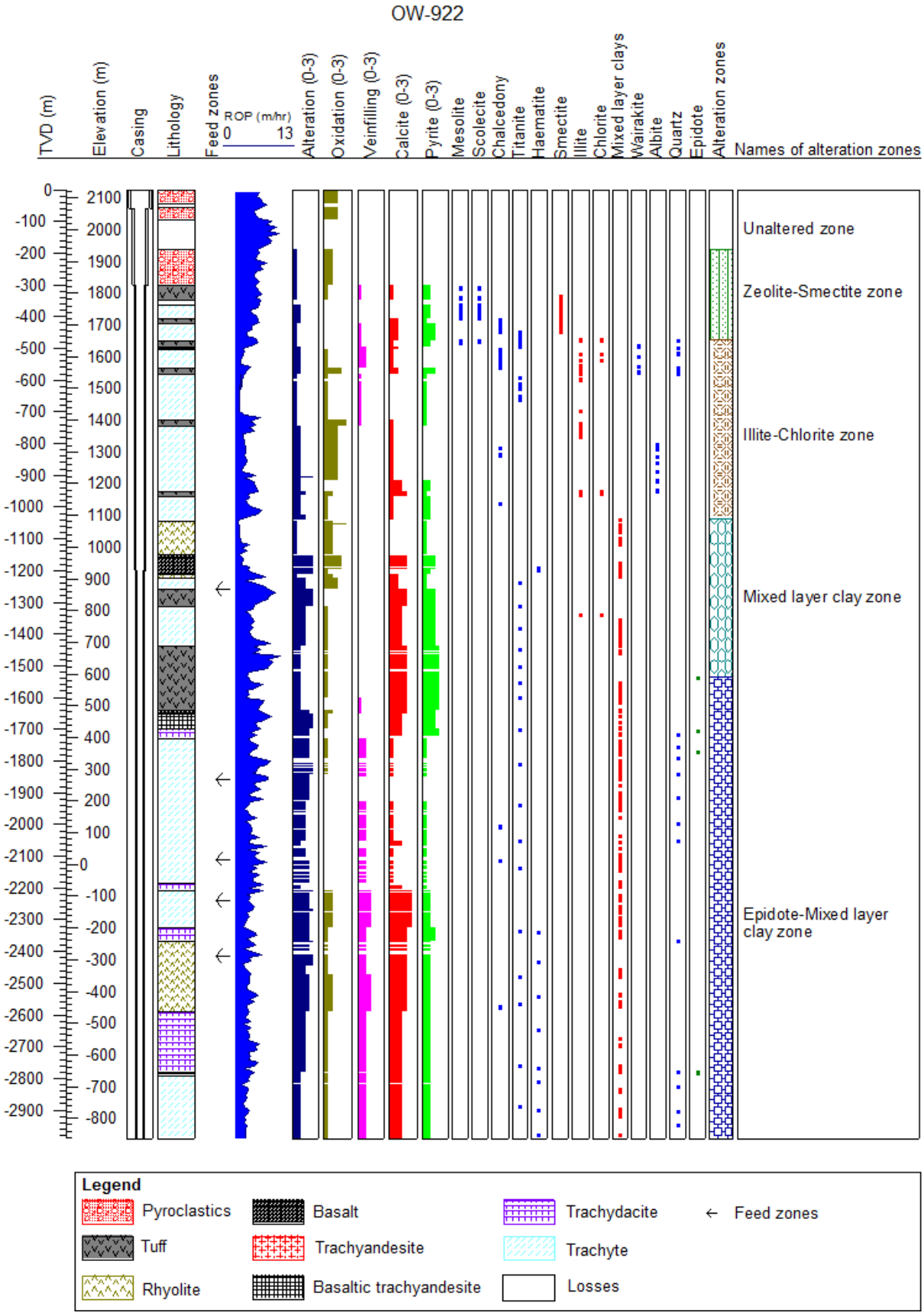

FIGURE 14: Lithology, location of feed zones, distribution of alteration minerals and alteration zones of well OW-922

Zeolites are hydrated aluminosilicate minerals structurally characterized by a framework of linked tetrahedra, each consisting of four oxygen atoms surrounding a silicon or aluminium cation. This three-dimensional network has open cavities in the forms of channels and cages (Wise, 2005), which are occupied by water molecules and non-framework cations. Occurrence of zeolites in geothermal environments is usually typified by three different fabrics, namely, fracture and vesicle fillings, as replacement products of relict feldspars, and, as recrystallization products of siliceous or glassy groundmass of volcanic rocks (Wise, 2005). Most zeolites, with the notable exception of wairakite, are low-temperature minerals which, are thermodynamically unstable at temperatures >110^{o}C.

Unlike in most wells in the Olkaria geothermal system, the occurrence of zeolites in this well is restricted only to two low-temperature types, *mesolite*, a high-silica zeolite, and *scolecite*, a low-silica zeolite. Both were observed largely as vesicle infillings in tuffs at 302-350 m, 362-364 m and 408-422 m, and in trachyte at 364-408 m. *Mesolite* was identified by the occurrence of white, thin, needle-like crystals, which radiate away from the base, forming spiky ends. By contrast, *scolecite* was in most cases colourless and formed clusters radiating from a central point of growth.

Wairakite, a calcium-rich zeolite, was first observed in a vesicular tuff between 494-496 m. It occurs in association with hydrothermal quartz and more rarely with calcite. It is characterised by a colourless to murky white colour with aggregates of subhedral crystals, coating fractured surfaces. It is also identified filling out the abundant pore spaces in pumiceous fragments at 574-578 m. The occurrence is nonetheless sporadic. The first appearance of *wairakite* at 494 m in well OW-922 signifies a temperature of about 200^{o}C and it seems to be the only zeolite stable above that particular temperature (Kristmanndóttir, 1979).

Chalcedony is a cryptocrystalline variety of quartz, characterized by a translucent white to grey to light blue, and in some instances shades of brown. The mineral was first observed at 412 m as a white thin-layered lining in a vesicle. It is also found intermittently and occurs in the deeper sections of the well, for example between 2576-2578 m. Chalcedony forms at temperatures from 150^{o}C to as high as about 180^{o}C (Kristmanndóttir, 1979), but gradually recrystallizes to hydrothermal quartz with increasing temperature (e.g. between 2114-2116 m).

Haematite is a low-temperature Fe-oxide whose occurrence is associated with the incursion of cold groundwater and other oxidizing conditions in a geothermal system (Brown, 1978). The mineral was observed by binocular analysis as a silver-grey, brown to reddish brown in colour. It was noted in moderate amounts between 1192 and 1200 m, and occurs irregularly from 2342 to 2982 m.

Titanite is recognized as white coloured mineral, usually as a replacement of the mafic silicates. The mineral is very common in this well and was first observed between 422 and 476 m, occurring sporadically to the well bottom. In petrographic analysis, titanite is identified by its high relief, brown to dark brown colour and shows dusty-cloud discoloration formed by the alteration of the ferromagnesian minerals.

Calcite is ubiquitous in the well and occurs in all the hydrothermal mineral alteration zones. The occurrence is particularly prevalent at 1120-1730 m and 2210-2990 m, where it is rated at a scale of between 2 and 3 (Figure 14). The latter indicates high abundance, whereas, the former signifies moderate abundance. The mineral is noted as a replacement of primary forming minerals, especially plagioclase and pyroxene phenocrysts, and discrete silicic volcanic glass. This process inevitably requires introduction of CO_3^{2-} ions from the geothermal fluids (Steiner, 1977). In addition, calcite is observed as precipitates in veins and vesicles (e.g. at 520-522 m, 1600-1646 m) and as platy calcite (e.g. at 1646-1648 m and 1944-1946 m), possibly indicating deposition through mixing of fluids with different compositions. However, in some rare cases, it is noted as a complete groundmass replacement. In active geothermal systems, calcite is usually regarded to be stable over a broad temperature, ranging from ~ 50 to about 300^{o}C (Simmons and Christenson, 1994).

Pyrite is a hydrothermal mineral whose presence in significant amounts has traditionally been associated with permeable zones in most geothermal systems. It was first observed at 302 m in a tuff. Like calcite,

pyrite occurs pervasively to the well bottom. The occurrence varies between 1 to 3, implying low and high abundance, in that order. In binocular analysis, the mineral was recognized by euhedral cubic crystals with a shiny brass yellow lustre, predominantly disseminated and, in other instances, embedded in the rock matrix. On rare occasions, for example between 1312 and 1420 m, the mineral is seen filling veinlets. The cubic crystal nature was equally applied while distinguishing pyrite from the other opaque minerals in petrographic analysis. According to Steiner (1977), pyrite is a product of the replacement of magnetite (Equation i) or result from the attack of FeO in ferromagnesian minerals with H_2S gas (Equation ii); such processes are known to occur in other geothermal systems.

(i) $Fe_3O_4 + 6H_2S \leftrightarrow 3FeS_2 + 4H_2O + 2H_2$

(ii) $FeO + 2H_sS \leftrightarrow FeS_2 + H_2O + H_2$

Furthermore, the Fe in the pyrite is suggested to be possibly introduced by the geothermal fluids, which commonly contain minute amounts of Fe (Steiner, 1977). An alternative interpretation is that the Fe may be leached from neighbouring rocks and transported perhaps only for a short distance before being converted to pyrite. Pyrite also occurs over a broad temperature, ranging from ~50°C to about 300°C (Brown, 1978).

Hydrothermal quartz is observed mainly as an open-space filling mineral in veinlets, vesicles, vugs and interstices of fractured rocks. It is generally colourless to occasionally white coloured, hexagonal shaped, commonly found as subhedral to euhedral crystals that rarely exceed ~ 2 mm in length. The mineral was first noted between 476 and 478 m filling vesicles in a tuff, designating formation temperature in excess of 180°C (Reyes, 2000). The occurrence is however, sporadic to the well bottom. In many cases, it is found in association with wairakite, pyrite and titanite. In thin section, quartz was easily identified by the undulating extinction, lack of cleavage and low interference colours. Petrographic evidence unequivocally shows that quartz to a greater extent precipitated or was introduced by geothermal fluids as opposed to crystallised from SiO_2 released during alteration of silicic glass and/or feldspar phenocrysts and ferromagnesian minerals.

Albite. The term albitisation in this context is reserved for the replacement of primary K-feldspar (specifically sanidine in this case) and plagioclase phenocrysts by hydrothermal albite. The upper limit of this mineral in the well is at 802 m and it occurs irregularly but disappears totally below 952 m depth. The mineral was identified during binocular investigation by its cloudy white and striated surfaces. The mineral grains vary largely between anhedral to subhedral in all cases. Albite is formed at a temperature of 180°C or higher (Brown, 1978), and its presence implies zones of low permeability.

Epidote was first noted at 1542 m through petrographic analysis from its high relief, pale green to pale yellow and greenish brown pleochroism, in addition to parallel extinction. The interference colours are distinctively bright (second order). Generally, epidote is sporadically distributed in this well and is found more commonly as a replacement mineral of the primary feldspars (plagioclase and sanidines) and to a lesser extent the pyroxenes. It occurs at discrete depths and disappears completely below 2784 m. The minerals that were commonly found in association with epidote include mixed-layer clays (MLCs), secondary quartz, calcite, pyrite and titanite. In drill cuttings analysis, epidote was identified by its conspicuous yellow to greenish yellow colour. Pure crystalline epidote is rarely present and in most instances (e.g. at 2234-2236 m and 2570-2580 m) the mineral was observed only as a faint coloration. In most geothermal systems, the appearance of epidote indicates temperatures equal to or above 240°C (Bird and Spieler, 2004).

Clay minerals

The ubiquitous nature of clay minerals as a function of physico-chemical environment of crystallization has enabled their application as markers of paleo-conditions in active geothermal systems. Geothermal systems are especially fruitful places to study clay minerals genesis since these environments serve as natural laboratories where fluid-rock interactions occur under measurable conditions (Steiner, 1968). The distribution of clay minerals in active geothermal fields depends on the ability of the fluid to approach equilibrium with host rocks at any scale during the hydrothermal processes. Clay mineral transformations are governed by the Ostwald Step Rule (Moore and Reynolds, 1997). According to the

rule, clay mineral paragenesis evolves through the formation of successive metastable phyllosilicates that progress towards the state of stable chemical and textural equilibrium. The minerals have proved to be particularly useful for temperature estimations (mineral geothermometers) based either on modifications of crystal structure (crystallinity, interstratification, order-disorder, etc.) or modifications of crystal chemistry (layer charge, substitutions, etc.) of the crystallites (Moore and Reynolds, 1997). Clay minerals in well OW-922 occur largely as replacement products of volcanic glass, feldspars, ferromagnesian minerals and rarely as depositional products in veins and vesicles. In the latter cases, the minerals are found in association mostly with hydrothermal quartz. Identification of the clay minerals was primarily based on the position of d-spacings determined with XRD after air-drying, saturation with ethylene glycol and heat treatment. X-ray diffraction analysis of drill cuttings from well OW-922 revealed four distinct minerals of the phyllosilicate group as discussed below. Representative X-ray data for clay minerals observed in this well are compiled in Appendix B, and selected X-ray diffractograms shown in Figures 15 and later in Figure 18.

Smectite

Smectite, also known as ‘‘swelling clay” is a low-temperature clay alteration mineral and was first noted at 338 m depth through XRD analysis. It forms at comparatively low temperatures, up to 120°C, though generally not exceeding about 200°C (Brown, 1984). In the study well, the occurrence of smectite is widespread, occurring at shallow depths of the well (338-450 m) and extending to depths between 1138 and 1166 m. The mineral is noted largely replacing volcanic glass and ferromagnesian minerals. In binocular analysis, the mineral was identified by its extremely fine-grained and poorly crystallized nature, particularly in the uppermost 450 m. The colour varies from light to dark green to brown. According to Steiner (1968), smectite is commonly the first clay mineral phase to replace volcanic glass and likely represents a metastable phase of reaction progress involving glass and hydrothermal fluids. Diffraction patterns of the untreated air-dried samples show broad d(001) peaks ranging from 12.4 Å to 15.0 Å (Figure 15). The basal diffraction peak is quite sensitive to ethylene-glycol treatment and invariably widens to higher spacing, ranging from 16.9 Å to 17.5 Å. However, the peak irreversibly collapses upon heating to about 9.97 Å (Figure 15), corresponding to the theoretical spacing for ideal smectite. The observed changes of the first-order, basal reflection, d-spacing between peaks is caused by variation of interlayer water molecules.

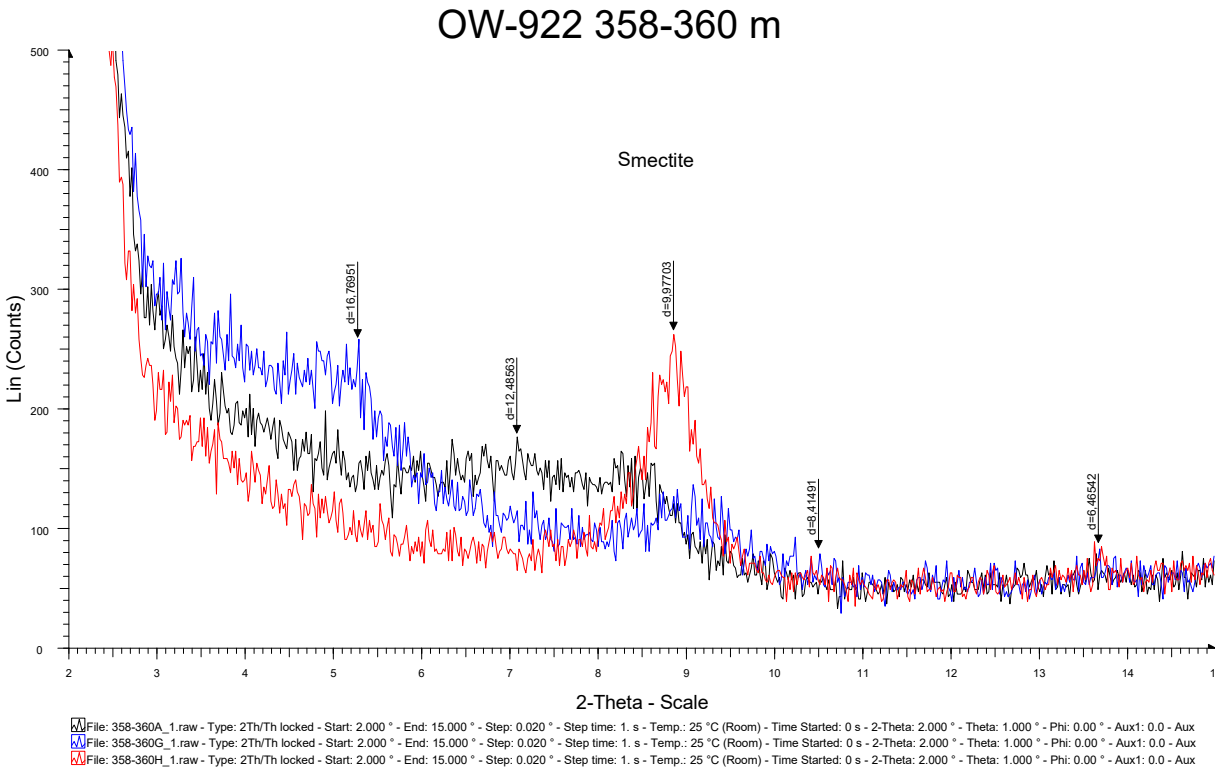

FIGURE 15: X-ray diffractogram of air dried, glycolated and heated sample of smectite

Laird (2006), observed that smectites swell by absorbing water or polar organic solvents between smectite quasicrystals and/or between the individual layers within quasicrystals. Such swelling occurs when the clay is dispersed in a solvent, or when the clay is in direct contact with an atmosphere having a high vapour pressure of the solvent. Smectite is associated with a secondary mineral assemblage consisting principally of pyrite, zeolites and quartz. In many geothermal systems (Steiner, 1968), smectite has been noted gradually transforming to illite in response to increasing temperature or depth through a series of progressively more ordered smectite/illite interlayer structure. In contrast, cases of illite converting back to smectite have equally been observed in other geothermal fields, e.g. in Wairakei (Steiner, 1968), particularly where there is an inversion of temperature.

Mixed-layered clays (MLCs)

The term MLCs is synonymous with interlayered or interstratified clay minerals. Essentially, MLCs represent clay minerals derived from two or more kinds of intergrown layers as opposed to physical mixtures (Moore and Reynolds, 1997). Most often, MLCs contain smectite as a swelling/expanding component. The interlayering is defined by three particular types, i.e. regular (ordered), random or segregated (Moore and Reynolds, 1997). In well OW-922, these clays mark the transitional stage from swelling to non-swelling varieties. They are noted as the most predominant clay mineral phases, occurring regularly to the bottom of the well. MLCs apparently can form in many possible combinations of different layers. However, the common varieties in this case are smectite/illite, smectite/chlorite and the three component type, smectite/illite/chlorite. The latter is the most abundant and widespread form, occurring to the well bottom. It is characterised by a d-spacing of 15.4-12.2 Å for untreated samples and 17.8-16.5 Å for ethylene glycol solvated samples. The expanded layers collapse to about 9.98 Å upon heating. The chlorite component is indicated by the 7 Å peak which collapses totally as a result of oven heating. MLCs were not identified in binocular analysis but were recognized by the relatively more yellowish to green colour, stronger pleochroism and brighter birefringence colours (Figure 16) relative to chlorite in optical petrography. MLCs were first noted at 1038 m through XRD analysis (Appendix B). EMP analysis (analyses not shown) show relatively higher K_2O (7.7-9.8 wt.%) for MLCs compared to chlorite (0.12-0.62 wt.%). These clays are normally stable at temperatures ≤ 220°C.

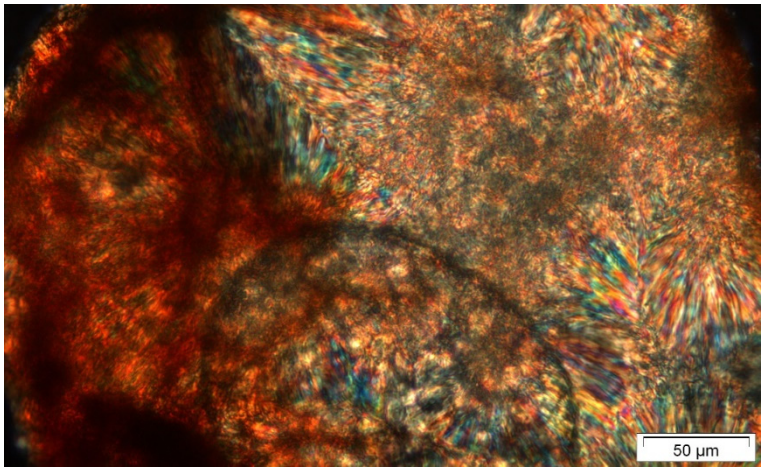

FIGURE 16: Cross polarized image of mixed-layer clay depicting high interference colours at a depth of 2782 m

Illite

Illite was first noted at 474 m through XRD analysis. The mineral occurs at temperatures of approximately 200°C or more. It is observed to form mostly from the alteration of feldspars, even though precipitates in veins and vesicles are also noted in small quantities. The mineral is associated with a mixture of secondary minerals including variable but generally trace amounts of hydrothermal quartz, chlorite, and pyrite. In thin section, illite is colourless to yellowish brown, with the texture varying between fine to coarse. In many cases (e.g. between 1238 and 1240 m), it was observed as matted flakes or fibrous aggregates. In XRD analysis, the diffraction patterns for the untreated sample show a first order basal reflections at ~10 Å and do not show significant departure from the 10 Å integral series upon ethylene glycol solvation and heating.

Chlorite

Chlorite is a common clay mineral in the Olkaria geothermal system whose occurrence indicates reservoir temperatures exceeding 220° C (Kristmanndóttir, 1979). In well OW-922, chlorite formed as a replacement product of ferromagnesian minerals (mostly pyroxenes) and feldspars (sanidine and

plagioclase), and also as densely packed aggregates filling vesicles. It occurs preferentially in basalts and trachyte and is associated with mineral assemblages of quartz, calcite and pyrite, and rarely, epidote. According to the XRD results, pure chlorite is seldom found as an individual phase, but in many cases the mixed-layer clays has chlorite structure layers along with smectite and illite layers (Appendix B). The colour varies widely from green to bluish green as observed in binocular investigation. In thin section, the mineral is fibrous and displays light to dark green colours, weakly pleochroic from yellow green to green (Figure 17). In addition, it has low interference colours (first order gray). Occasionally, the mineral occurs in minute amounts forming spherulites.

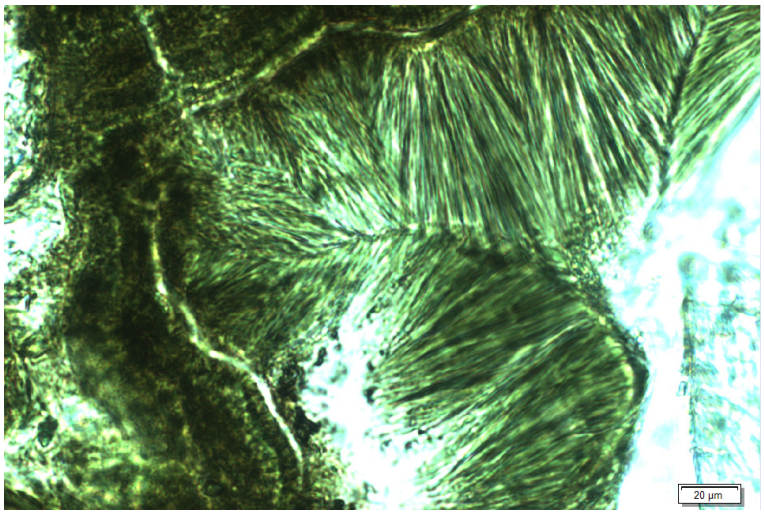

FIGURE 17: A plane polarized image of fibrous chlorite filling a vesicle at 1826 m

In XRD analysis, the spacings of the first order d(001) basal reflections at ~12.4-14.7 Å are not affected by air drying, glycol solvation or heat treatment. This peak however, is obscured in most samples in this well (e.g. Figure 18), leaving the second order reflections d(002) stable at ~7.0-7.1 Å for untreated and glycol treatment as the only conspicuous peaks. The latter, totally disappears upon oven heating though. Previous studies (e.g., Otieno and Kubai, 2013) have termed this chlorite as an unstable variety and it is the most common chlorite type in many wells in the Olkaria sub-fields. A widely quoted hypothesis by Moore and Reynolds (1997) suggests this kind of chlorite to be Fe-rich. EMP analysis results for chlorite, discussed in section 4.9, are fully in agreement with this observation. Based on their argument, the Fe-rich component in the chlorite is introduced by prolonged interaction between the adjacent host rocks and the altering solution.

4.4 Hydrothermal alteration zonation

Many high-temperature geothermal systems of the world are, divisible into different zones based on changes in alteration assemblages. Different alteration minerals become stable or metastable within a particular temperature range and with certain fluid compositions. Thus, by mapping the mineral sequences as well as the alteration minerals, it is possible to deduce the thermal evolution and conditions of a specific geothermal system (e.g. Mortensen et al., 2014). Alteration zones are characterised by an abundance of particular minerals corresponding to increased temperature and depth. The top of each alteration zone is defined by the depth of the first appearance of a mineral. Four alteration zones, namely zeolite-smectite, illite-chlorite, mixed-layer clay zone and epidote-mixed-layer clay zone, were distinguished below the unaltered zone based on optical petrography and binocular observations. Representative alteration mineral assemblages of each zone are listed as well. Identification of the different clay types in this well relied largely on XRD results (Figure 14), and to a lesser extent on electron microprobe analysis.

0-190 m depth: Unaltered zone: This is the lowest grade alteration zone in this well. It is composed of relatively fresh rocks, mainly pyroclastics with no alteration signature related to geothermal activity, an indication that the temperatures have been < 50°C. Volcanic glass constitutes the bulk of the rocks and are conspicuous both in binocular and petrographic observation. The unaltered zone is characterised primarily by oxidation, which supposedly is related to the interaction between the host rocks and the comparatively oxygen-rich descending cold groundwater. Total loss of circulation between 96 and 190

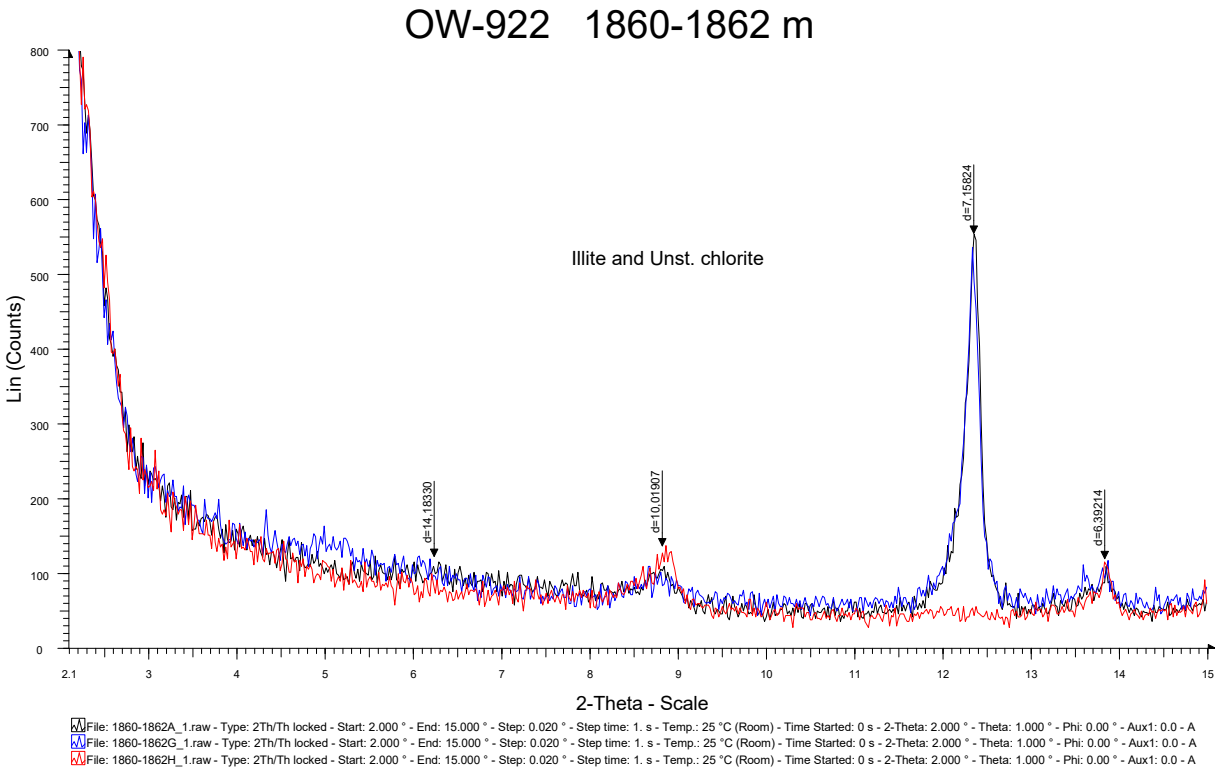

FIGURE 18: X-ray diffractogram of illite and unstable chlorite showing obscured peak of 14.18 Å for the three treatments and 7.15 Å peak for air dried and glycol solvation; the latter peak totally collapses upon heating

m (Appendix A) made it impossible to locate precisely where this zone terminates within the specified depth range.

190-474 m depth: *Zeolite-smectite zone*. The alteration mineral assemblages in this zone are characterised by low-temperature zeolites, smectite clay and trace quantities of pyrite and calcite. Other notable minerals include chalcedony and titanite. The low-temperature zeolites present in this zone are mesolite and scolecite. Smectite was first recognized by XRD analysis at 338 m (Appendix B), suggesting that the temperatures in this zone are < 180-200ºC.

474-1038 m depth: *Illite-chlorite zone*. The concurrent appearance of illite and chlorite at 474 m defines the top boundary of this zone, signifying that the formation temperature is gradually increasing with depth and is in excess of 200ºC. In conjunction with this, the zeolites (mesolite and scolecite) show indications of instability and completely disappear at 482 m. Quartz and wairakite appear and are first identified at 476 and 494 m, respectively. According to XRD analysis, the chlorite is an unstable variety. Other alteration minerals found in this zone are chalcedony, titanite, calcite, albite and pyrite. Calcite is ever-present as open-space and matrix fillings, while pyrite is prevalent as patchy disseminations in the rock groundmass.

1038-1542 m depth: Mixed layer clay (MLC) zone. The characteristic feature of this zone is the first appearance of MLCs, in the form of smectite/chlorite at 1038 m. Based on the discussion under MLCs, temperatures in this zone are ≤ 220ºC. Common assemblages continue to include pyrite, calcite, haematite and titanite.

1542-2990 m depth: Epidote-mixed layer clay zone. Epidote first occurs at 1542 m and defines the top of this zone. It is the largest zone extending to the well bottom. The first appearance of epidote indicates that the formation temperature has been at or higher than 240ºC. The occurrence of this mineral is very sparse in comparison to MLCs. Epidote is observed to occur until about 2784 m, after which it totally disappears to the bottom of the well. In addition to MLCs, epidote, quartz, titanite, chalcedony,

haematite and pyrite, calcite is by far the dominant mineral phase. The mineral is observed overprinting epidote at 2782 m.

4.5 Distribution of alteration mineral zones in the Domes area

Alteration mineral zones are basically the result of diagnostic alteration minerals present within a particular geothermal system, and can give reliable indications of the reservoir temperature. The formation of hydrothermal minerals, as discussed above is not solely a function of temperature, but also fluid composition, initial composition of the rock system, permeability, etc. (Brown, 1978). In Figure 19, the distribution of alteration mineral zones in the study well is compared with results of previous studies (e.g. Musonye, 2015; Mwangi, 2012). From this figure, it is evident that zones indicative of high temperatures, e.g. illite-chlorite-epidote and chlorite-epidote-actinolite, marked by the first appearance of epidote and actinolite, respectively are present at relatively shallow depths (between 1280 and 1440 m a.s.l., and 800 and 1240 m a.s.l., respectively) in wells OW-910, 916 and 914.

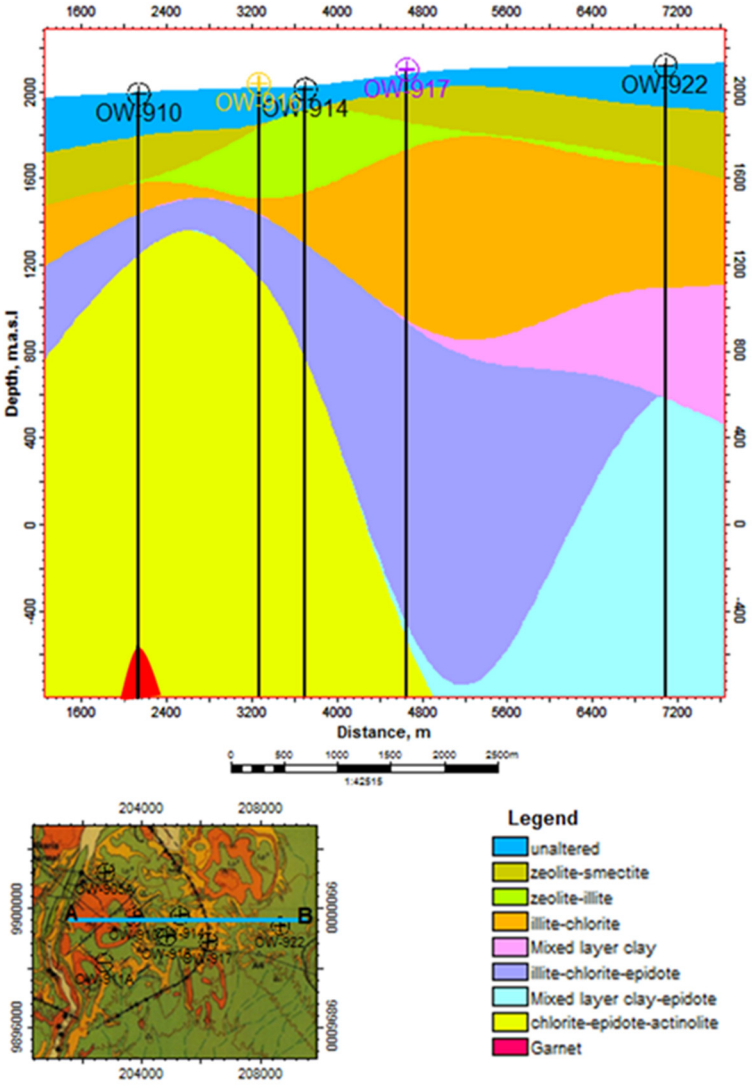

FIGURE 19: Distribution of alteration mineral zones across a section of the Domes area, along the traverse A-B

The same zones appear at relatively greater depths in well OW-917. However, in well OW-922, the two zones are conspicuously absent, even though it is known from hydrothermal mineralisation that the first appearance of epidote in this well occur at even much greater depth, i.e. at 458 m a.s.l. according to Figure 19. Observations made for the distribution of alteration mineral zones across a section of the Domes field positively correlate with the model for measured formation temperature distribution across the same field (see Figure 35 later). High formation temperatures are observed at comparatively shallow depths in wells OW-910, 916 and 914, whereas, at greater depths in well OW-917. In contrast, well OW- 922 is generally characterised by low temperatures.

4.6 Feed zones

Feed zones are basically water-saturated regions in the sub-surface which produce an economically feasible quantity of water to a well. The primary goal of drilling a geothermal well is to intersect as many permeable and hot feed zones as possible, below the production casing, so as to maximise the well productivity. For locating feed points during drilling, one can rely on a combination of observations, including, circulation losses or gains, intrusive boundaries, lithological contacts, changes in alteration

mineralogy patterns, appearance of highly fractured formations, changes in circulating fluid temperatures, as well as temperature recovery logs. In the Domes area, the location of feed points from previous studies (e.g. Mwangi, 2012; Ronoh, 2012; Lagat, 2004) have been inferred primarily from lithological boundaries, highly fractured lavas, sudden increase in the rate of penetration and variation in alteration patterns.

In drill cuttings analysis of the study well, fluid "feeder" zones below the production casing were deduced from lithological interfaces, alteration intensities and drilling parameters (i.e. rate of penetration (ROP)). Observations of circulation losses have equally played some role, but not to a large extent since most of the loss zones encountered range between 2 and 14 m, and in most cases are principally attributed to a change in stand-pipe pressure during POOH to change a drill bit. Temperature and pressure recovery were determined by four heat-up profiles, i.e. after 9 hours and, 12, 21 and 49 days. Pre-injection temperature and pressure profiles were taken prior to the recovery tests. However, it is worth noting that no injection tests were conducted since the well got filled up with water during injection, which argues against the existence of any major feed zone(s). As a consequence, no injectivity index was measured for this well. Another key point to highlight is that the temperature recovery over a period of only 49 days is not sufficient for the geothermal system near the well to reach stable conditions following the long drilling time (Figure 13).

Step pumping was conducted between 19th September and 6th November, 2014. The first pumping rate was set at 1000 l/min, and then subsequently increased to 1300 l/min, 1600 l/min and finally 1900 l/min. Traditionally, this is the pumping rate, which has been adopted during step pumping of the Olkaria wells. During all pumping rates, temperature and pressure measurements were carried out at 100 m interval from the surface to 1200 m, which is the production casing depth. Afterwards, the interval was reduced to 50 m to the well bottom. These intervals are constant for all wells. However, the change from 100 to 50 m is subject to the casing depth, which is quite variable from one well to another. Pressure logs measured in this well (Figure 20) display no intersection of the various pressure recovery profiles, commonly referred to as the "pivot point".

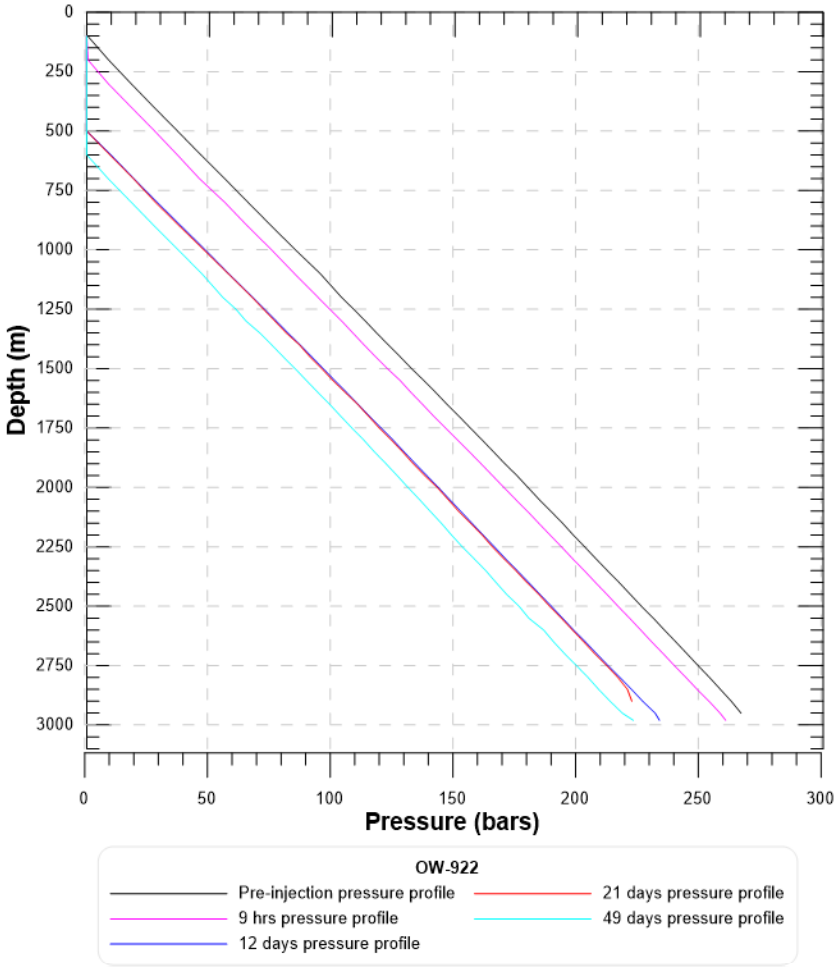

FIGURE 20: Downhole pressure recovery logs for well OW-922

From the temperature recovery logs (Figure 21), it is observed that temperature increases from the surface to about 2250 m at an average rate of 4.5° C/100 m depth. This is followed by a more or less constant temperature between 2300 and 2500 m depth. Below 2500 m, a steady decline (~ 3° C/100 m) is noted in all the five temperature logs to the bottom of the well. The increase in temperature from the surface to about 2250 m depth coincides with the trend of increasing alteration grade. A prograde change

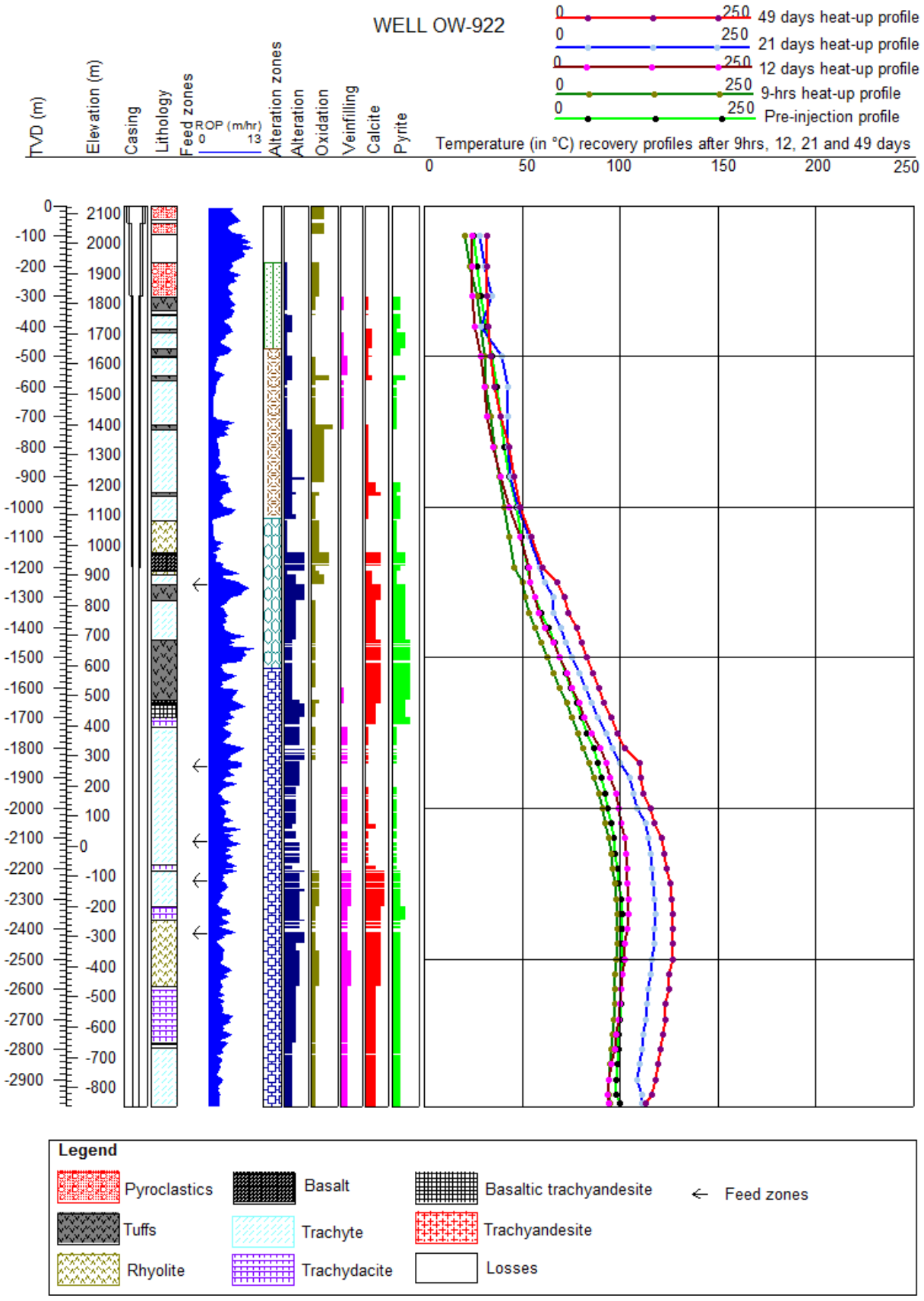

FIGURE 21: Feed zones in well OW-922 as deduced from temperature recovery logs, drilling parameters and geological observations

in alteration grade, cutting across different alteration zones, is observed to a depth of about 1798 m. This is consistent with the transition from the low-temperature alteration minerals, zeolites, smectites and

chalcedony to relatively high-temperature minerals, such as quartz, albite, wairakite, illite, chlorite and epidote (Figure 14).

Five small feed zones have been recognised from the study well. The classification criterion is based on the relative size of kink in temperature recovery logs and the extent of geological observations. These are located below the production casing at depths of 1260-1312 m, 1840-1900 m, 2070-2162 m, 2210-2276 m and 2360-2444 m. The feed zones are clearly evident from the kinks in temperature logs (Figure 21), and are supported by both drilling and geological observations. Feed zones noted above the production section (e.g., between 96-190 m) are of no consequence since this region has been completely cased off. However, such feed zones are costly to the drilling operations because they require large tonnes of cement to seal. Therefore, it is necessary to map and note their geological extent as a precaution to subsequent wells planned to be drilled on the same well pad. The feed zone between 1260 and 1312 m is hosted within a highly vesicular and altered tuff, marked by extensive pyritization. A remarkably high rate of penetration (4.8-10.2 m/hr) is observed within this zone, lending support to the geological observations.

Feed zone between 1840-1900 m, is hosted within a highly altered and extensive trachytic formation (Figure 14), characterised by numerous loss zones. Also, a deflection both in the temperature profile and ROP profile is noted within this zone. Feed zones between 2070 and 2162 m, and 2210 and 2276 m are located within highly vesicular and moderately to highly altered trachyte, characterised by several minor (2-10 m) loss zones. The final feed zone between 2360 and 2444 m is located at the lithological interface of trachydacite and rhyolite. It is also characterised by moderately to highly altered rhyolite, intense calcite deposition and several loss zones, ranging in size between 2 and 14 m. Temperature recovery profile indicates the highest formation temperature (127^{o}C) measured in the well, occur within this interval, despite the zone being associated with scarcity of high temperature alteration minerals. The observed feed zones are summarized in Table 4.

TABLE 4: Interpreted permeable zones based on geological observations

Depth (m)	Evidence based on geological observations	Size
1260-1312	Highly altered and vesicular tuff. Prevalence of pyrite deposition	Small
1840-1900	Highly altered trachyte. Numerous circulation losses	Small
2070-2162	Highly altered and vesicular trachyte. Numerous circulation losses	Small
2210-2276	Highly altered and vesicular trachyte. Numerous circulation losses	Small
2360-2444	Lithological interfaces between trachydacite and rhyolite. Moderate to high alteration intensity. Several circulation losses. Intense calcite deposition	Small

4.7 Alteration and measured formation temperatures

Studies of temperature dependent alteration minerals, temperature logging (direct down-hole measurements) and fluid inclusion homogenization temperatures (T_h) have successfully been applied to assess the physico-chemical conditions and temporal evolution of geothermal reservoirs in active geothermal fields (e.g. Marks et al., 2010). A hydrothermal alteration sequence provides significant insights into the history of a geothermal system. There is always some uncertainty whether the observed alteration mineral assemblages reflect the present formation temperatures or are related to some past thermal events. Like in many geothermal systems, hydrothermal alteration minerals in the Olkaria geothermal field have successfully served as important indicators of sub-surface thermal changes (e.g., Lagat, 2004; Mwangi, 2012; Okoo, 2013).

A correlation of the three methods leads to reconstruction of a more plausible and realistic model of a geothermal system. Fluid inclusion measurements were, however, not conducted on samples from the study well. As a result, reconstruction of the thermal history of the geothermal system around well OW-922 is based exclusively on inferred alteration and measured formation temperatures (Figure 22). Alteration temperature is used to present temperature in a geothermal system, and in many cases is

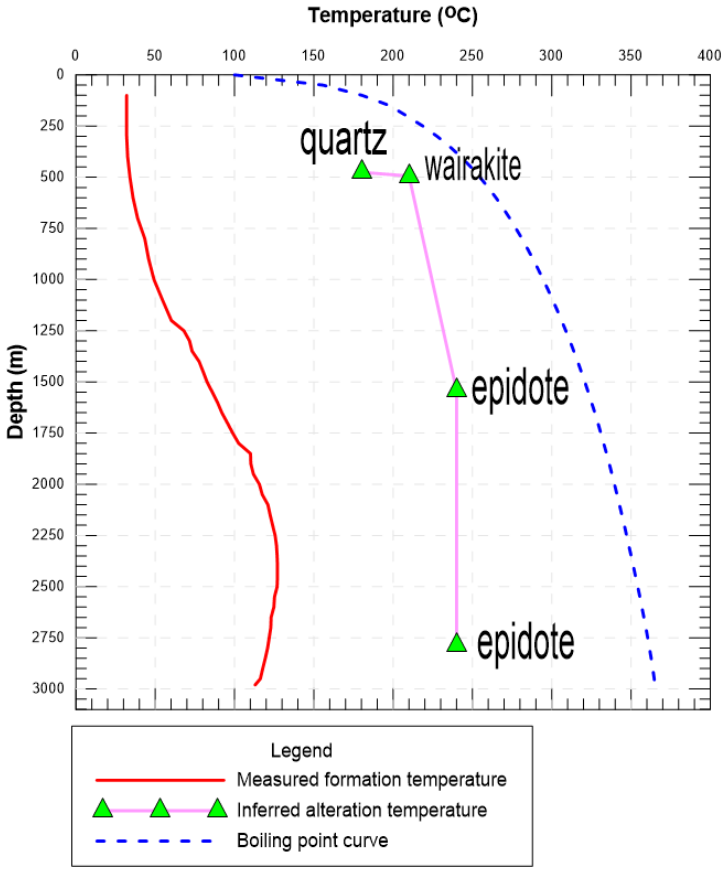

FIGURE 22: Comparison of inferred alteration and measured formation temperatures along with boiling point curve for well OW-922

assumed to represent the maximum long-term temperature state. In contrast, measured formation temperature represents the current state of the system. Alteration mineral curve plotted in Figure 22 relied on the first appearance of alteration minerals observed, namely quartz, wairakite and epidote. The three minerals have their first appearance at depths of 476, 494 and 1542 m, respectively. Temperature profile was plotted based on a 49-day heat-up period, i.e. the last temperature profile measured in the well.

4.8 Whole-rock chemistry

Bulk-rock chemical analysis is important in understanding the chemical diversity of the samples from the study well and the conditions under which the magma was generated. To achieve this, plots have been made, including TAS diagram, Al_2O_3 vs. FeO and several Harkers' variation diagrams based on the chemical analytical results. Generally, any sample has two types of elements: major and trace (including rare earth elements).

4.9 Major and trace element compositions

Thirty representative samples were analysed for whole-rock chemistry (major and trace elements) in the study well. Concentrations of 10 major element oxides and 13 trace elements were determined using the ICP-OES procedure outlined in Appendix C.

4.9.1 Major elements

Rocks in well OW-922 exhibit significant variations in major element compositions. Mafic and intermediate rock suites have striking similarities, depicting a homogeneous trend for FeO, MgO, and CaO, all showing a continuous decrease with increase in SiO_2 content for most of the samples (Figure 23). FeO shows a limited range (10.2-10.6 wt.%) in the mafic and intermediate rocks and, slightly low abundance (3-8 wt.%) in the highly evolved rocks. MgO is highly depleted in the highly evolved rocks (0.03-0.7 wt.%), whereas, the content ranges between 3-6 wt.% in the mafic and intermediate rocks. CaO has a more or less similar pattern to FeO, depicting a restricted range of between 6-11 wt.% in the mafic and intermediate rocks and declining significantly to an average of about 1 wt.% in the most silicic rocks.

TiO_2 exhibits a limited range in the mafics and intermediate rocks (1.83-2.08 wt.%) and decreases rapidly with increasing SiO_2 content (Table 5). P_2O_5 displays considerable scatter and no obvious variation trend, even though its contents are observed to decrease with increase in SiO_2 concentration. The scatter is more pronounced in the basic and intermediate fields. Like TiO_2, P_2O_5 is marked by a narrow range in the mafic and intermediate rocks (0.18-0.60 wt.%). The contents decrease from about 0.60 wt.% in the mafic rocks to just under 0.04 wt.% in the more silicic rocks, that is at approximately

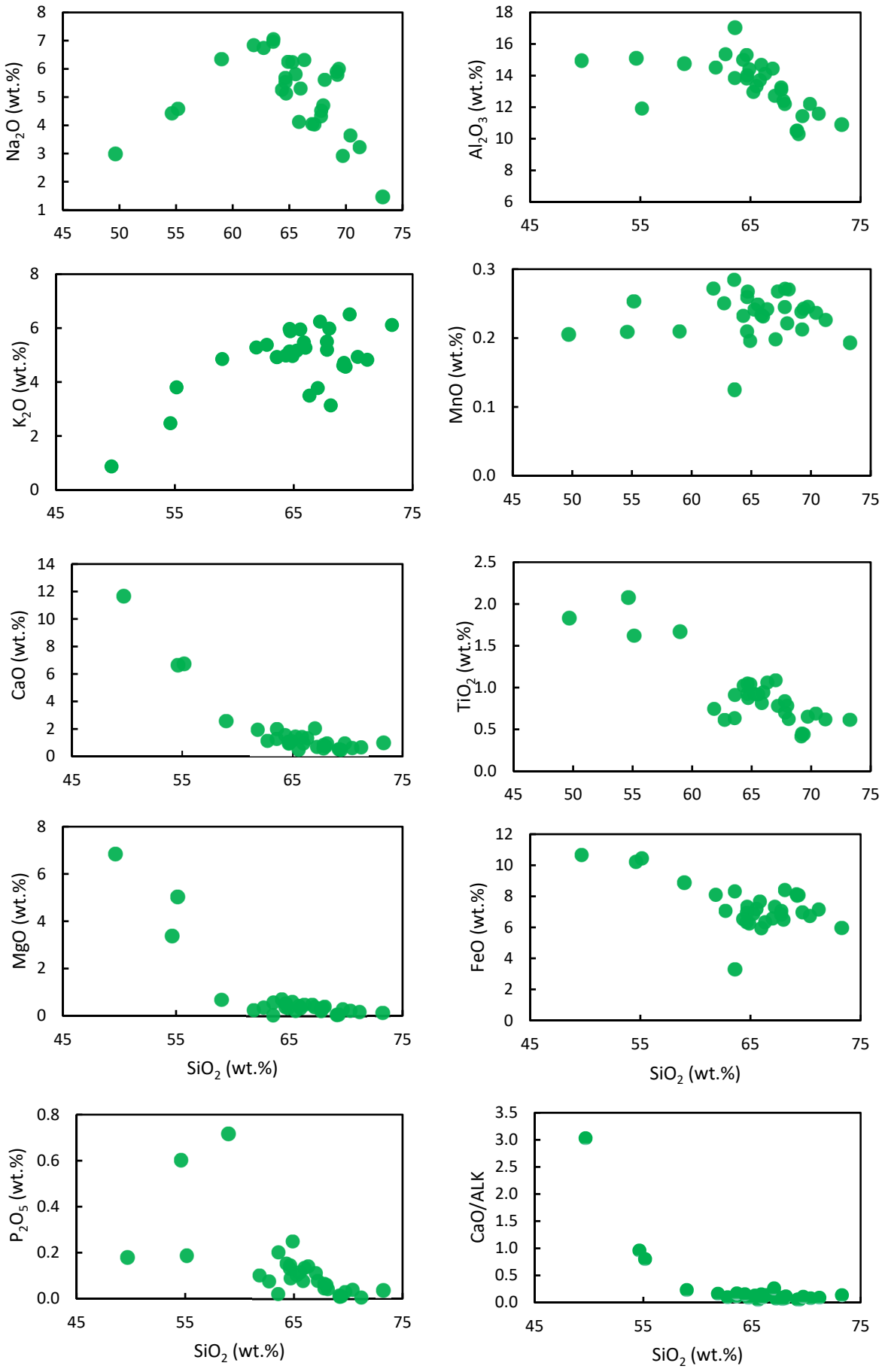

FIGURE 23: Harker diagrams showing major element oxides and CaO/ALK variations against SiO_2 for samples from well OW-922

69-73 wt.% SiO_2. On the other hand, MnO shows a nearly flat trend without any systematic variation with SiO_2 (Figure 23). The elements' contents are fairly constant between 0.13 and 0.28 wt.%. As a result, little emphasis is given on this element in interpretation of the data.

Al_2O_3 contents range from 10.3-17.04 wt.% in all the rock types. The element initially exhibits a more or less similar picture as MnO, but displays modest decline with increasing SiO_2 contents for most of the samples. Na_2O and K_2O correlate positively with SiO_2 at the initial stage. The two oxides have a very similar pattern even though sodium increases relatively more than potassium. The concentration of the two oxides increases and attains a peak at approximately 68 and 64 wt.% SiO_2 for potassium and sodium, respectively, followed by a slight decrease with increasing SiO_2 contents. The decrease is more prominent in sodium, particularly for the samples at the greatest depths (i.e. between 2420 and 2990 m) in the well. In contrast, K_2O content appears to flatten out with a further increase in SiO_2 concentration. The two elements are generally lower in the mafics and intermediate rocks compared to the evolved rocks. In particular, Na_2O concentration is distinctly higher than K_2O, with the exception of a few samples in the trachytes and trachydacites. The composition of the two elements in rhyolites is, however, quite variable. Also, the CaO/ALK (ALK = total alkali) ratio for the analysed samples decreases markedly as SiO_2 content increases. Peralkalinity index (i.e. P.I. = mol. [Na+K]/Al) of the samples analysed ranges between 0.26 and 1.03.

4.9.2 Trace elements

The term trace element lacks a rigid definition, even though several authors (e.g. Hardarson, 1993) have used this term in many instances to refer to those elements present in rocks in concentrations of a few parts per million (ppm). The significant features of the trace element concentrations observed from the variation diagrams (Figure 24) as differentiation progresses from the mafic to silica rich rocks are: (1) the progressive depletion in the concentrations of the transition metals, Sc, Co, V, Cr, Ni, and, Sr with increase in SiO_2 contents, (2) Incompatible trace elements (ITEs), such as the HFSE, Y and Zr; Rb and LREE, La, show significant enrichment with increase in SiO_2 contents.

Vanadium decreases approximately from 300 ppm to 168 ppm from the mafic to intermediate rocks. Subsequently, an abrupt drop in V content down to 0.5 ppm is observed in the highly evolved rocks. Cr content is high in the mafic rocks (132 ppm) but exhibit a remarkable decline in the intermediate rocks (17-59 ppm). The concentration further decreases to between 2 and 27 ppm in the silicic rocks. Sc vs. SiO_2 plot shows a small but consistent decrease in Sc content between the mafic and intermediate suites (47-25 ppm) until about 69 wt.% SiO_2 where the drop is rather steep (0.2-0.3 ppm). The rhyolitic rocks are more depleted in Sc compared to the other evolved rock suites. A fair amount of scatter is apparent in Sr concentration in the mafic and intermediate rocks as well as in two trachytic samples (1878 and 1922 m). The element shows a decrease from 376 ppm to 256 ppm as SiO_2 increases to about 55 wt.%. A significant decrease to about 8 ppm, thereafter follows in the more evolved derivatives. Two trachytic samples at 1878 m and 1922 m depth, however, contain anomalous Sr contents, 307 and 344 ppm at relatively high SiO_2 contents, i.e. 58 and 63 wt.%, respectively.

Rubidium shows high abundance (123-226 ppm) with increase in SiO_2 (64-73 wt.%). A significant decline ($\leq$ 78 ppm) is observed in the mafic and intermediate rocks, characterised by SiO_2 range of between 49-55 wt.%. Y displays a very similar trend to Rb, showing a gradual increase with increasing SiO_2 concentration. In particular, it is more enriched (101-304 ppm) between 67-73 wt.% SiO_2. La follows similar pattern as Rb and Y. The element shows a concentration of between 110 and 424 ppm at SiO_2 content of between 63-73 wt.%. The contents, however, fall to < 80 ppm in the mafic and intermediate rocks. Zr shows significant increase with increasing SiO_2 content but scatters mostly between 2793 and 2995 ppm. Ba, on the other hand exhibits wide scattering in whole-rock compositions with no well-defined trend. The element occurs in considerable abundances in the intermediate rocks, even though exceptionally high abundances (1775-2238 ppm) are observed in the trachytes. However, Ba is strongly depleted in the rhyolites, in most cases falling below 20 ppm. Results of major and trace element concentrations are presented in Table 5.

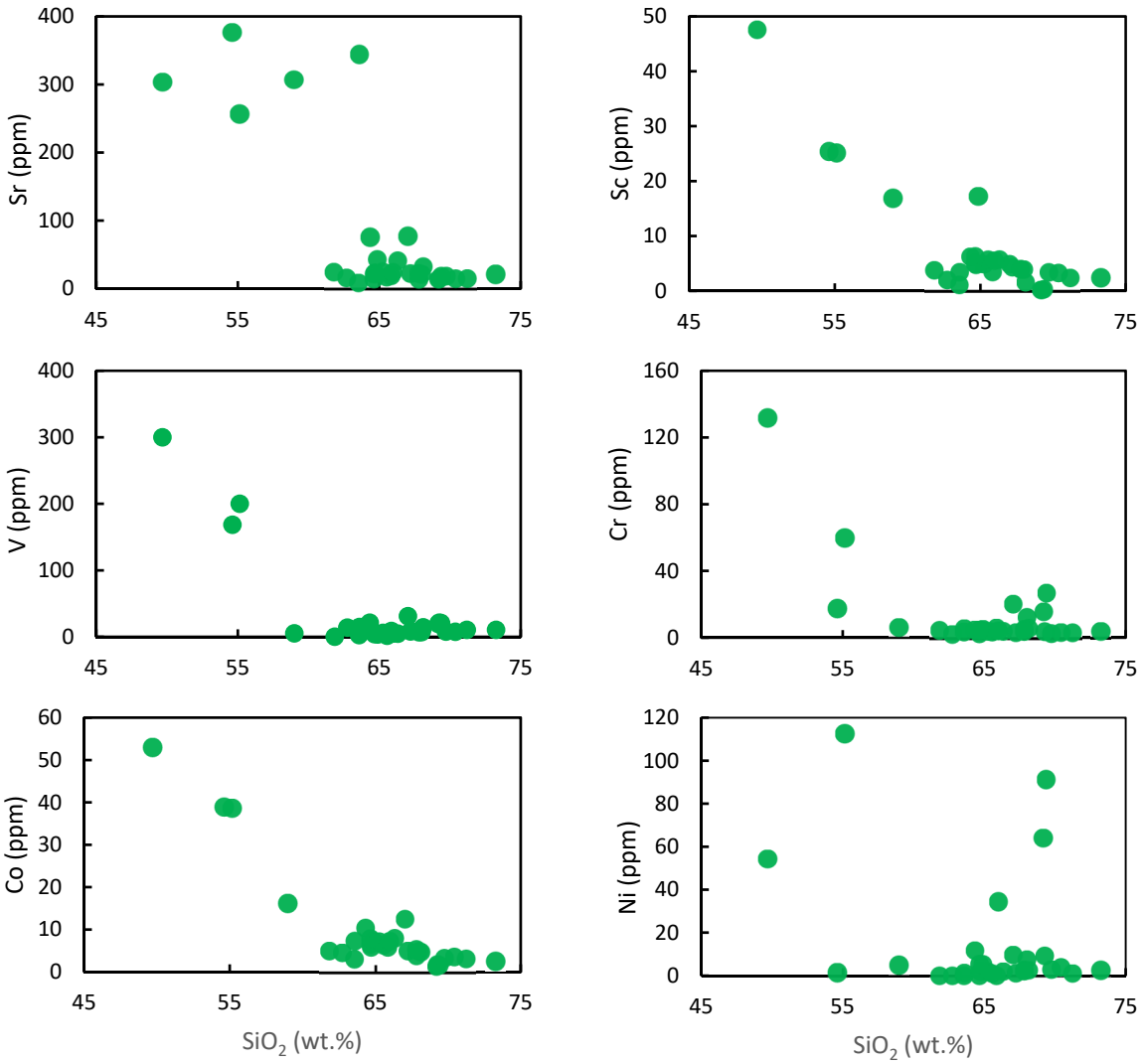

FIGURE 24: Variation diagrams for a range of trace elements plotted against the index of differentiation, SiO_2 for samples from well OW-922

4.10 Classification of rock types

Petrologists have devised several schemes for the chemical classification of non-pyroclastic volcanic rocks. In spite of that, none has been found fully satisfactory. Many systems were in use before classification based on the amount of alkali ($Na_2O + K_2O$) versus silica (SiO_2) diagram in igneous rocks, popularly known as the "TAS diagram" (Figure 25), was eventually accepted by the International Union of Geological Sciences (IUGS). The variation of silica and total alkalis is a highly useful discrimination technique. The total alkali axis essentially distinguishes alkaline from sub-alkaline rocks types, whereas the silica axis distinguishes between evolved and primitive rock types. An important contributing factor that led to the acceptance of this method was its simplicity, which is an essential aspect of a classification scheme for volcanic rocks (Le Bas et al., 1986).

Generally, the compositional variation seen on a TAS diagram may be regarded as a result of two basic processes, namely partial melting and fractional crystallisation, even though magma mixing can be important in some cases. In this respect, decreasing degree of partial melting results in increased total alkalis and lower SiO_2. Fractional crystallisation, on the other hand brings the rocks to both higher alkali and silica content (e.g. Hardarson, 1993). In this section, petrochemical results from the study well are presented and compared with the results of the previously studied wells (Musonye, 2015) aimed at understanding the chemical composition and petrogenetic mechanisms responsible for the evolution of

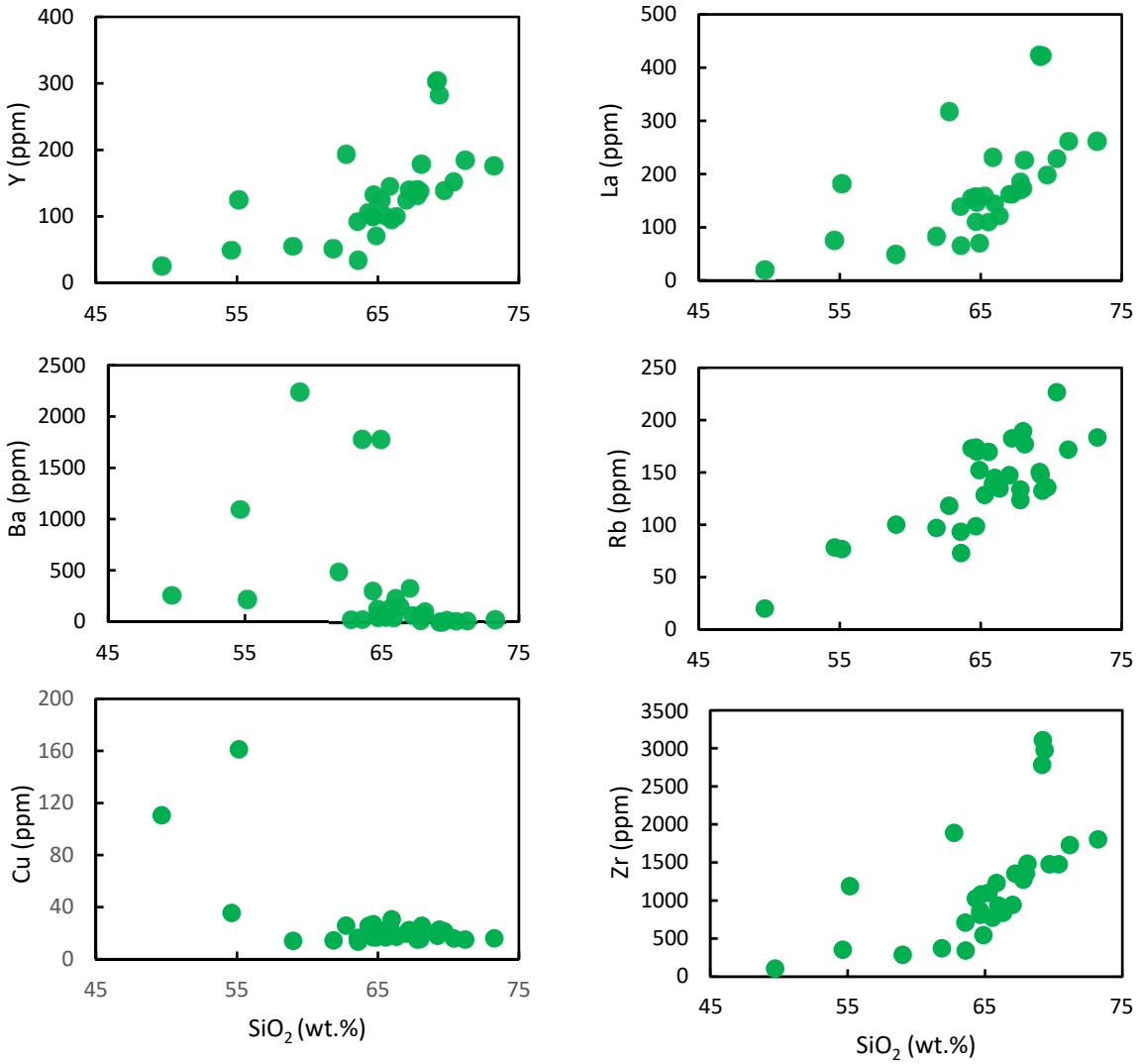

FIGURE 24 (continued): Variation diagrams for a range of trace elements plotted against the index of differentiation, SiO_2 for samples from well OW-922

OVC sub-surface rocks. Additionally, the results are compared with the findings for surface samples for Olkaria and the minor eruptive centres surrounding the complex.

4.10.1 TAS classification

In the TAS classification scheme, the concentrations of the major elements have been re-calculated to 100% on a volatile-free basis to ensure comparability and are plotted as such in the variation diagrams. From the classification of the rocks in the TAS system shown in Figure 25, it is apparent that rocks from well OW-922 show a range of compositions. The sub-alkaline rocks vary from basalt through trachydacite to rhyolite, whereas, the alkaline rocks range from basaltic trachyandesite through trachyandesite to trachyte.

The prevalence (~ 85-90%) of evolved rocks is noticeable, depicting a relatively wide range in SiO_2 (59-73 wt.%). Basic and intermediate rocks constitute about 10% of the intersected succession, and have a SiO_2 range of between 49.7-55 wt.% (Table 5). A large volume of the salic differentiates cluster to a great extent in the trachydacite, rhyolite and trachyte fields, with the latter being the dominant rock type. A few samples are, however, transitional in composition, falling along the boundary separating the alkaline from sub-alkaline series.

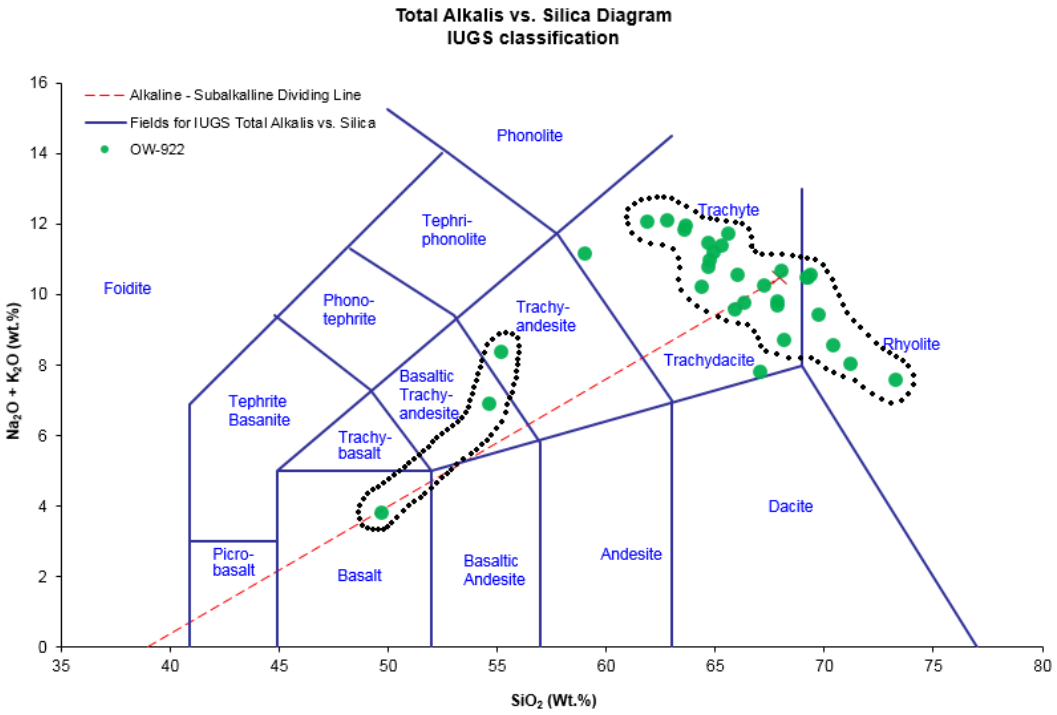

FIGURE 25: TAS diagram showing the compositional range for sub-surface rocks from well OW-922, according to Le Bas et al. (1986)

Based on petrographic analysis, the rocks from well OW-922 are variably porphyritic with plagioclase and clinopyroxene as the dominant phenocrysts phases, together with olivine and opaques (Fe-Ti oxides) in the mafic to intermediate samples. In the more salic varieties, K-feldspar (sanidine) is the predominant phenocryst phase, although plagioclase and clinopyroxene (aegerine-augite) are also noted in considerable amounts.

4.10.2 Al2O3 vs. FeO classification scheme

This is a classification scheme put forward by Macdonald (1974), using the correlation between alumina and total iron (as FeO) plot to evaluate the relationship of the samples based on the degree of peralkalinity. Peralkaline rocks are basically divided into comendites, pantellerites, comenditic trachytes and pantelleritic trachytes (Macdonald and Scaillet, 2006). By definition, comenditic rocks refers to the mildly peralkaline varieties, whereas, the pantelleritic counterparts, refers to more strongly peralkaline and more Fe-rich rocks ($FeO>Al_2O_3$) (Macdonald, 1974). None of the analytical samples fall under the definition of pantelleritic, as in all cases, Al_2O_3 is observed to be greater than FeO (Table 5).

Based on this classification scheme (Figure 26), it is evident that rocks from the study well traverse the division between comenditic trachyte, pantelleritic trachyte and pantellerite, with the last one being the dominant variety. No samples plot within the comendite field. Most of the trachytes plot in the comenditic trachyte field, with a few exceptions plotting as pantelleritic trachyte and pantellerites. Rhyolites, on the other hand plot within the pantellerites field. From the Al_2O_3 vs. FeO plot, it is clear that the

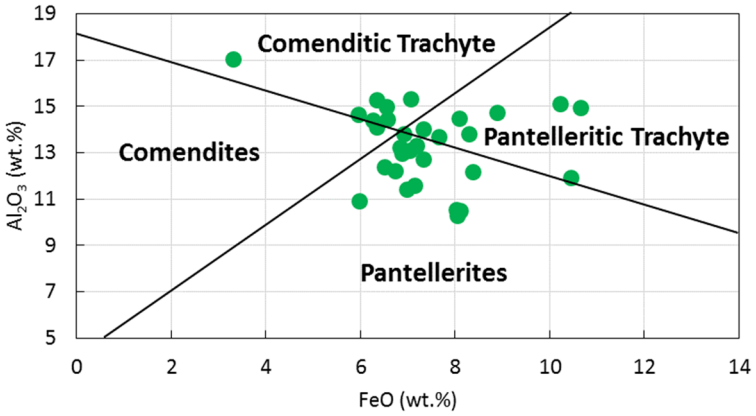

FIGURE 26: Al_2O_3 vs. FeO classification (modified from Macdonald, 1974) of sub-surface rocks from well OW-922

differentiation trends for these samples are appreciably variable.

4.11 Comparison of well OW-922 with surface and other sub-surface samples

This section presents a comparison of the geochemical results from well OW-922 with surface samples from Olkaria and other minor eruption centres located along the periphery of the complex (Figure 8). Surface data from Olkaria, together with the minor eruption centres were acquired from previous studies of Macdonald et al. (2008), Marshall et al. (2009) and Clarke et al. (1990). Majority of the surface samples are considered quite fresh and apparently devoid of alteration. Additional sub-surface whole-rock chemistry data have been obtained from Olkaria, published by Musonye (2015).

4.11.1 Comparison with surface samples

From Figure 27, it is immediately evident that samples from wells OW-922, 905A, 910 and 917 plot in more or less similar fields to the surface samples from Olkaria and neighbouring minor eruption centres. The Lolonito, Ndabibi and Akira basalts (Figure 7) plot in a similar field to basalt and basaltic trachyandesite from the study well and the other three wells. Equivalently, the Gorge Farm and Broad Acres rhyolites, Olkaria comendites (Figure 8) and Tandamara trachytes (Figure 7), plot mostly in a similar position as the trachyte and rhyolites from well OW-922.

4.11.2 Comparison with other sub-surface samples

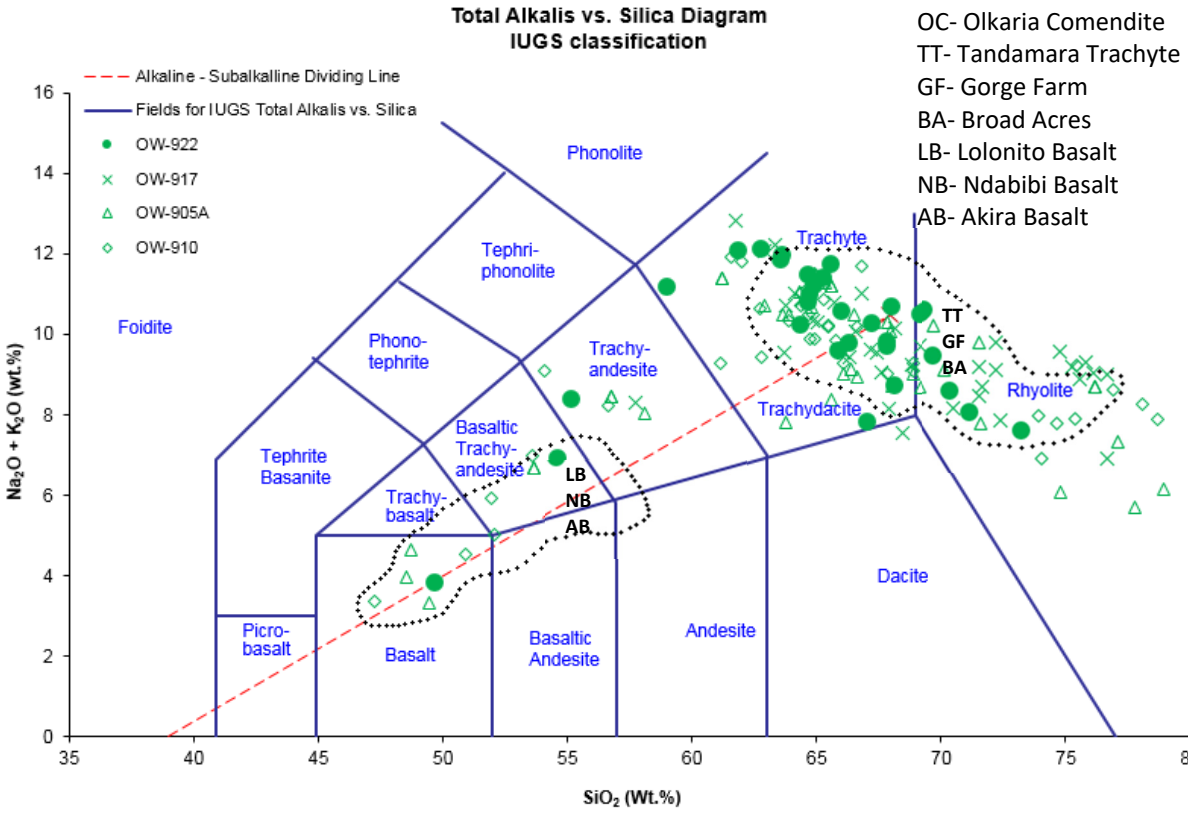

FIGURE 27: TAS classification scheme showing comparison of sub-surface samples from wells OW-922, 905A, 910 and 917 and, surface samples from Olkaria and neighboring minor eruption centres (represented by broken lines)

Using selected major element oxides and trace element variation diagrams (Figures 28 and 29), a comparison has been made to check for any connection in the evolution mechanism(s) between wells 905A, 917, 910 and 922. Once again, SiO_2 has been used as the index of differentiation. It is noticeable that the ferromagnesian major element oxides (FeO, MgO, CaO) as well as TiO_2 and P_2O_5 in the other

three wells behave in a manner akin to well OW-922 (Figure 23), showing a gradual decline with increasing SiO_2 values. For K_2O and Na_2O, the trend starts with a positive slope and bends to a negative one at ~ 65 wt.% and ~ 62 wt.% SiO_2 respectively. The change in slope is far more pronounced in Na_2O than K_2O. Similarly, V, Sr, Sc and Co are anti-correlated with SiO_2 (Figure 29), and show a very similar overall picture to the ferromagnesian major oxides, pointing to their compatible behaviour. On the other hand, La, Y, and Zr exhibit positive correlations with SiO_2. It was observed that rocks from wells OW-905A, 910 and 917 are slightly more enriched in SiO_2 (44-80 wt.%) than corresponding rocks from the study well (49-73 wt.%). In summary, comparison of the geochemical results for the selected major and trace elements for the four wells demonstrate a perfect overlap across the whole range of compositions.

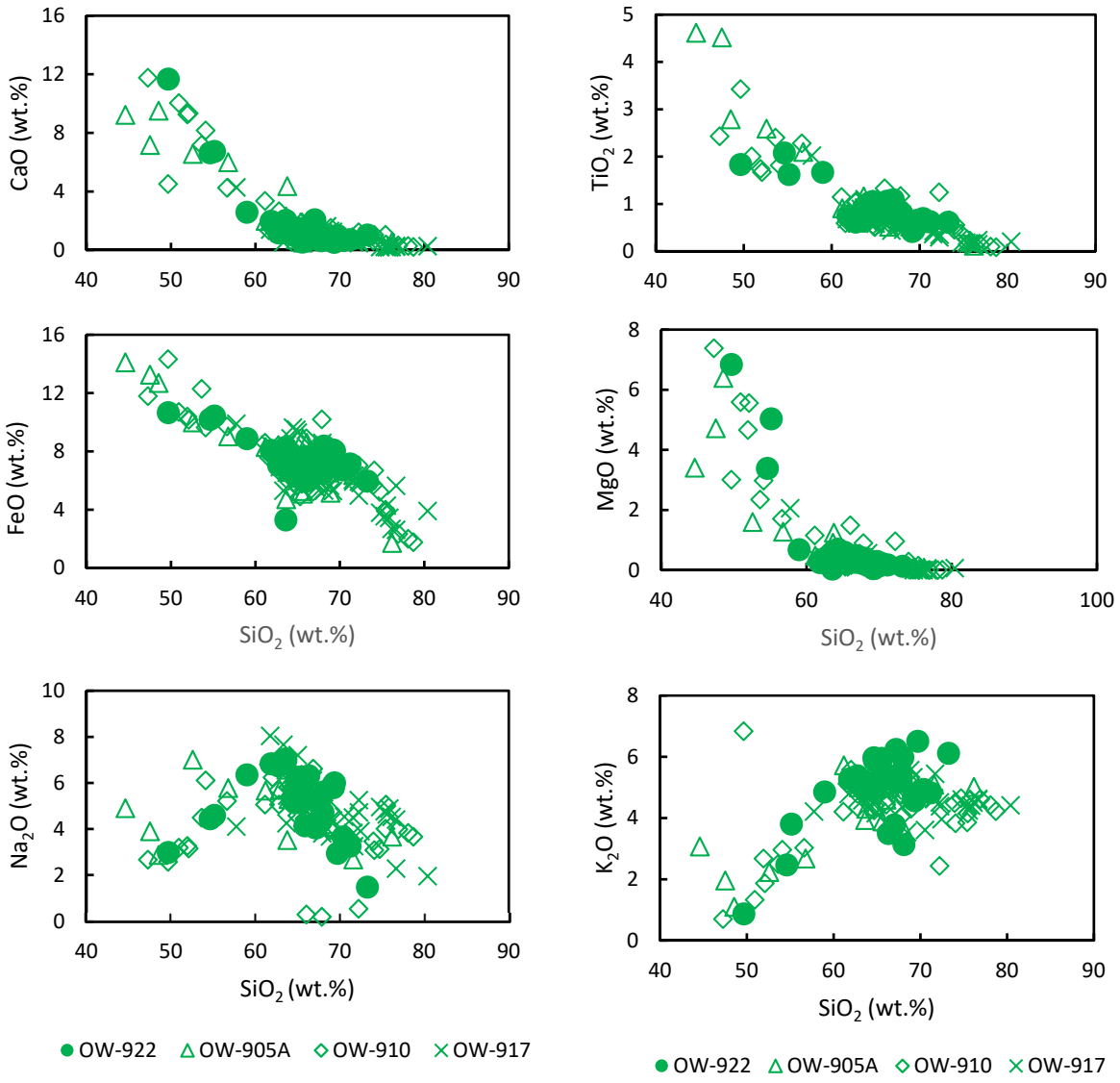

FIGURE 28: A comparison for variation in concentration of selected major element oxides for wells OW-922, 905A, 910 and 917

TABLE 5: Major and trace element results for well OW-922 based on ICP-OES analysis

Major elements (wt.%)															
Depth	**864 m**	**966 m**	**1106 m**	**1142 m**	**1208 m**	**1332 m**	**1672 m**	**1704 m**	**1734 m**	**1808 m**	**1878 m**	**1922 m**	**1966 m**	**2056 m**	**2088 m**
SiO_2	61.85	63.57	69.17	69.36	49.67	62.74	54.62	65.85	64.65	64.89	63.59	58.99	64.71	65.26	65.55
Al_2O_3	14.50	13.84	10.50	10.30	14.94	15.34	15.10	13.70	15.30	14.40	17.04	14.76	14.02	12.96	13.32
FeO	8.08	8.29	8.11	8.05	10.66	7.06	10.21	7.65	6.34	6.26	3.31	8.88	7.32	6.87	7.18
MnO	0.27	0.28	0.24	0.24	0.21	0.25	0.21	0.23	0.21	0.20	0.13	0.21	0.27	0.24	0.25
MgO	0.25	0.03	0.05	0.06	6.84	0.35	3.38	0.42	0.37	0.33	0.56	0.68	0.51	0.59	0.22
CaO	1.96	1.31	0.57	0.53	11.67	1.17	6.64	1.44	1.10	1.14	2.02	2.58	1.02	1.47	0.54
Na_2O	6.83	6.95	5.90	6.00	2.98	6.73	4.44	4.14	5.69	6.25	7.04	6.35	5.13	6.23	5.81
K_2O	5.28	4.93	4.61	4.57	0.87	5.38	2.47	5.47	5.14	4.97	4.93	4.85	5.88	5.17	5.95
TiO_2	0.75	0.64	0.42	0.44	1.83	0.62	2.08	0.82	0.93	1.04	0.91	1.67	0.88	0.93	0.92
P_2O_5	0.10	0.02	0.01	0.01	0.18	0.08	0.60	0.08	0.13	0.25	0.20	0.72	0.09	0.10	0.11
Total	99.87	99.87	99.58	99.56	99.85	99.72	99.76	99.79	99.85	99.72	99.73	99.68	99.82	99.82	99.85
Trace elements (ppm)															
Ba	482.52	26.48	0.00	0.00	255.88	24.22	1094.92	41.20	55.68	1775.59	1777.61	2238.54	42.70	45.74	131.01
Co	5.05	3.15	1.45	1.72	52.93	4.63	38.92	5.91	6.59	7.30	7.39	16.15	5.91	7.23	6.38
Cr	4.77	3.85	15.75	26.69	131.78	2.33	17.39	6.16	2.72	5.41	5.77	6.20	4.87	4.21	3.80
Cu	14.41	16.34	20.83	22.69	110.58	25.71	35.54	24.57	16.78	16.81	13.50	14.04	18.61	20.50	16.80
La	82.72	139.07	424.45	422.93	19.76	317.50	75.51	231.23	158.38	70.42	65.98	48.92	146.52	159.60	110.13
Ni	0.00	0.00	64.13	91.44	54.37	0.00	1.38	0.00	0.00	5.32	1.35	4.81	1.92	1.85	1.00
Rb	97.11	93.39	150.54	132.69	20.08	118.30	78.42	139.10	98.73	152.38	73.15	100.18	170.05	128.52	169.74
Sc	3.75	1.09	0.20	0.30	47.57	1.99	25.40	3.43	4.98	17.24	3.41	16.81	4.73	4.87	5.67
Sr	24.23	8.66	13.94	18.36	303.93	15.71	376.84	18.81	14.28	42.69	344.45	307.00	23.05	24.74	17.10
V	0.56	2.79	19.56	20.94	300.20	14.13	168.63	9.16	5.71	3.85	14.98	5.58	5.64	6.15	1.93
Y	51.47	92.92	302.93	282.72	26.18	193.71	49.68	145.25	100.40	71.72	34.64	55.36	133.06	124.64	101.08
Zn	136.74	179.65	358.59	368.48	97.19	222.95	126.65	224.30	165.60	126.90	65.26	134.52	193.55	199.89	175.22
Zr	368.19	706.84	2793.51	2984.86	100.40	1895.18	349.16	1230.88	863.51	541.83	340.04	283.14	1080.77	1102.87	773.63
Total	1271.53	1274.23	4165.89	4373.81	1520.84	2836.36	2438.43	2080.02	1493.34	2837.47	2747.52	3231.27	1831.38	1830.80	1513.49

TABLE 5 (continued): Major and trace element results for well OW-922 based on ICP-OES analysis

Depth	2190 m	2234 m	2288 m	2300 m	2348 m	2360 m	2420 m	2482 m	2522 m	2570 m	2600 m	2668 m	2782 m	2802 m	2982 m
Major elements (wt.%)															
SiO_2	66.32	64.66	67.21	67.99	67.02	68.11	73.26	71.19	70.38	69.71	67.80	67.79	55.14	65.98	64.33
Al_2O_3	14.10	13.81	12.72	12.39	14.43	12.20	10.92	11.59	12.21	11.44	13.11	13.24	11.92	14.67	14.99
FeO	6.34	6.92	7.32	6.50	6.58	8.37	5.97	7.15	6.74	6.97	7.05	6.82	10.43	5.96	6.54
MnO	0.24	0.26	0.27	0.22	0.20	0.27	0.19	0.23	0.24	0.25	0.27	0.25	0.25	0.23	0.23
MgO	0.47	0.52	0.38	0.35	0.47	0.39	0.13	0.17	0.22	0.28	0.21	0.32	5.03	0.33	0.69
CaO	1.36	0.98	0.74	0.78	2.06	0.99	1.02	0.71	0.66	0.99	0.88	0.63	6.73	0.99	1.58
Na_2O	6.31	5.53	4.05	4.72	4.06	5.61	1.47	3.25	3.66	2.94	4.53	4.33	4.59	5.31	5.27
K_2O	3.50	5.97	6.24	5.98	3.78	3.13	6.12	4.83	4.93	6.51	5.20	5.50	3.81	5.28	4.98
TiO_2	1.06	1.05	0.78	0.79	1.09	0.63	0.62	0.62	0.69	0.65	0.70	0.84	1.62	0.95	1.03
P_2O_5	0.14	0.15	0.08	0.06	0.11	0.04	0.04	0.01	0.04	0.03	0.05	0.07	0.19	0.13	0.15
Total	99.84	99.84	99.78	99.78	99.79	99.75	99.73	99.74	99.76	99.77	99.80	99.79	99.71	99.82	99.79
Trace elements (ppm)															
Ba	149.58	127.92	64.01	58.13	325.68	100.83	20.24	12.19	10.05	18.94	13.73	69.62	214.55	229.35	299.50
Co	8.01	7.94	5.05	4.97	12.48	4.78	2.58	3.22	3.64	3.36	3.93	5.43	38.67	7.32	10.41
Cr	4.16	4.99	3.45	12.34	20.22	5.93	3.90	3.37	3.52	2.88	5.28	4.05	59.80	4.49	5.08
Cu	17.22	26.86	22.41	15.38	19.64	25.67	16.05	15.08	15.86	21.31	15.04	16.59	161.25	30.68	25.51
La	121.69	110.69	162.27	172.77	162.11	226.33	261.40	260.69	228.78	198.92	185.74	169.70	181.88	144.24	155.43
Ni	2.00	5.38	1.15	7.55	9.71	2.54	2.35	1.10	3.92	2.90	2.74	2.11	112.51	34.59	11.70
Rb	134.79	173.93	182.65	189.47	147.49	176.99	183.63	171.98	226.73	135.79	133.92	123.74	76.88	144.93	173.04
Sc	5.71	6.28	4.30	3.92	4.86	1.58	2.34	2.38	3.27	3.38	3.95	3.92	25.14	5.53	6.23
Sr	40.72	21.41	22.16	20.88	77.13	32.11	20.81	14.97	14.72	18.34	13.76	22.37	256.51	23.65	76.20
V	5.10	4.23	8.24	7.46	31.38	14.51	10.84	10.79	7.96	8.21	7.25	9.06	200.34	5.18	21.44
Y	100.80	99.82	140.46	137.88	124.71	178.46	176.06	185.15	151.88	139.13	131.22	141.02	125.19	95.25	106.83
Zn	148.91	175.62	230.49	199.54	201.56	283.65	210.56	227.88	214.70	245.66	215.22	203.28	248.31	162.09	153.31
Zr	837.44	810.00	1355.26	1357.33	943.30	1487.53	1807.54	1733.52	1479.58	1479.69	1275.09	1365.92	1189.73	934.39	1027.02
Total	1576.14	1575.07	2201.89	2187.62	2080.27	2540.91	2718.29	2642.31	2364.62	2278.52	2006.88	2136.81	2890.78	1821.69	2071.70

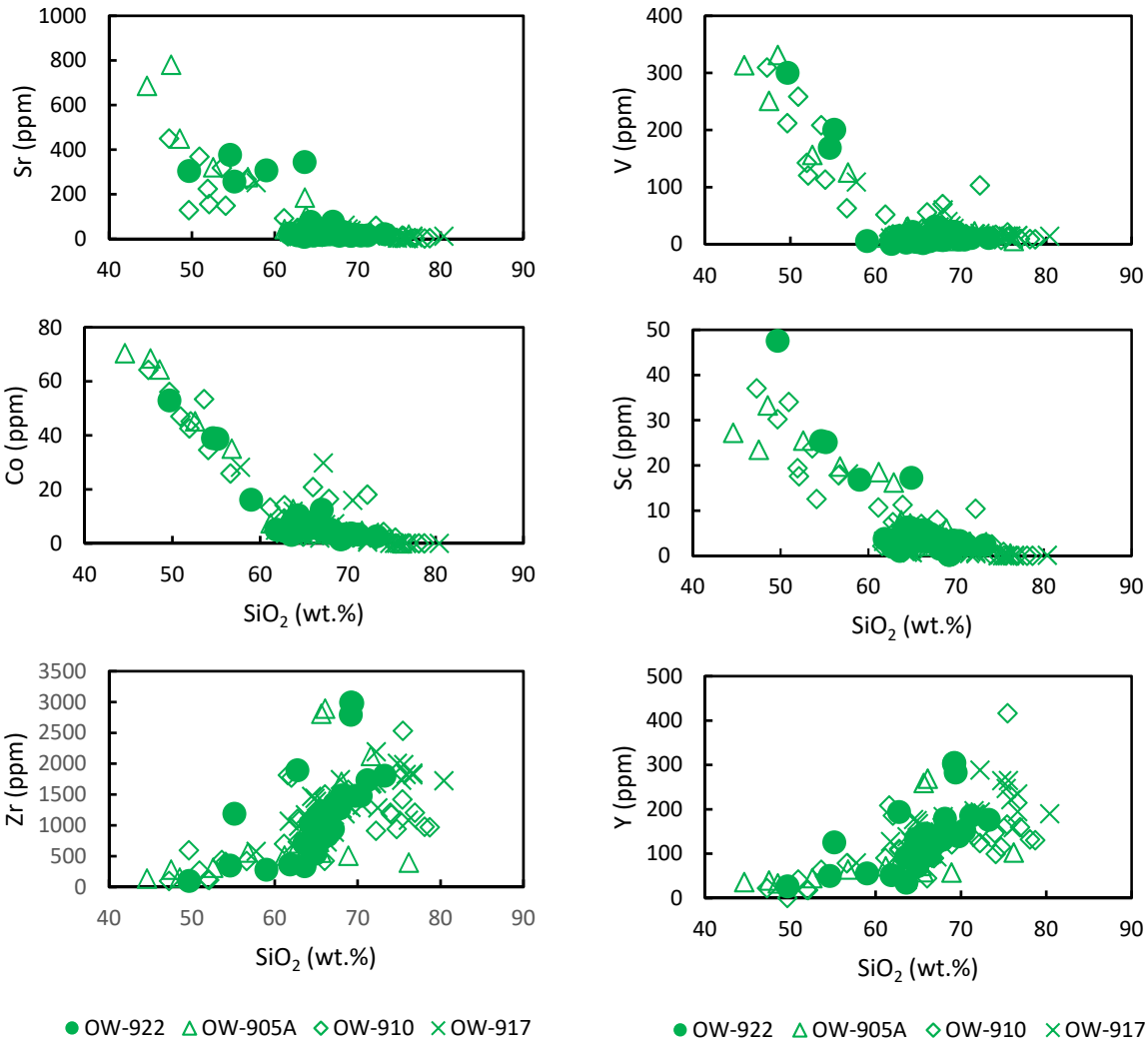

FIGURE 29: A comparison for variation in concentration of selected trace elements for wells OW-922, 905A, 910 and 917

4.12 Microprobe analysis

Selected samples of epidote and chlorite from wells OW-922, 905A, 910 and 917 were analysed with an electron microprobe (EMP). An important aspect of this analysis is to assess the chemical composition and the compositional range of epidote and chlorite in the mentioned wells. Interpretations made have been correlated with compositional ranges observed in other geothermal systems (e.g. Bird et al., 1988; Marks et al., 2010; Lonker et al., 1993; Bragason, 2012; Bird and Spieler, 2004). The first appearance of epidote and chlorite has commonly been used as a criterion for setting production casing in production wells in the Olkaria geothermal field. The selected epidote and chlorite samples analysed in the present study occur either as open space fillings in vesicles and fractures or as a replacement of original rock forming minerals, mostly plagioclase and sanidine. Associated alteration minerals were separated and not simultaneously analysed alongside these two minerals.

The mineral analyses were performed with a JEOL JXA-8230 electron microprobe located at the Institute of Earth Sciences, University of Iceland using carbon coated finely polished thin sections. The elements analysed were Si, Ti, Al, Fe, Mn, Mg, Ca, Na, K and Sr. Quantitative analyses with wavelength-dispersive spectrometers (WDS) were performed at an accelerating voltage of 15.0 keV, a cup current of 5.0 nA, and a beam diameter of between 5 and 10 µm. Counting time on peak was 40 seconds for all elements, except Na (30 seconds). Background counting time varied for different

elements. In the case of chlorite Si, Al, Fe, Mn and Mg backgrounds were counted for 20 seconds, those of Ti, Ca, Sr and K for 40 seconds and Na 15 seconds. Background counting times for epidote analyses were 20 seconds for Si, Al, Fe, Mn and Ca, 40 seconds for Ti, Mg, K and Sr, and 15 seconds for Na. Standards used were natural mineral standards. Structural formulae were calculated on the basis of 24 oxygens. It should be noted that Fe is calculated as ferrous and ferric iron in chlorite and epidote, respectively, and in all cases, Mn is calculated as divalent. Additional data sets for this study are shown in Appendix D.

Epidote [$Ca_2Fe_xAl_{3-x}Si_3O_{12}(OH)$] is an important index mineral in geothermal systems. The first appearance of this mineral demonstrates convincingly temperatures equal to or in excess of 240ºC. Detailed analysis of epidote compositions has been carried out in a number of geothermal systems, e.g. Salton Sea, Cerro Prieto, Los Azufres, Reykjanes, just to name a few with high level of success. However, no quantitative analysis of epidote have been done in the Olkaria geothermal system despite epidote being such an important mineral. The ability to accurately determine element concentrations of epidote by EMP analysis is crucial for a complete understanding of the chemical composition and changes in the compositional range.

There are three octahedral sites, M(1), M(2) and M(3), in monoclinic epidote where significant exchange of Fe^{3+} and Al^{3+} occurs. Ferric iron readily substitutes for Al^{3+} in both the M(1) and M(3) sites. Several studies (e.g. Arnason et al., 1993) have indicated that Fe^{3+} is preferentially incorporated in the energetically larger and more distorted M(3) site and, to a lesser degree, in the smaller and more regular M(1) site. At relatively low temperature, site M(2) is nearly free of Fe^{3+} and mostly contains Al^{3+}. It is only at high temperature that ferric iron enters the M(2) site.

The compositional range of most natural epidotes in active geothermal systems is closely described as a binary solid solution between the end-members clinozoisite [$Ca_2Al_3Si_3O_{12}$ (OH)] and pistachite [$Ca_2Fe_3Si_3O_{12}(OH)$]. Hence, the composition variation is dominated by the substitution of Fe^{3+} and Al^{3+} in the octahedral sites (Marks et al., 2010). Epidote composition is commonly expressed as the mole fraction of the pistachite component. The notation Xps has been adopted to denote the mole fraction of pistachite [$Xps = n_{Fe} / (n_{Fe} + n_{Al})$] where n_{Fe} and n_{Al} designate cation proportions in each formula unit.

Epidote paragenesis is controlled by a variety of intensive and extensive thermodynamic variables characterising hydrothermal systems. These include CO_2 and O_2 fugacities (fCO_2, fO_2), coexisting mineral assemblages, changes in fluid chemistry, bulk rock composition and temperature (e.g. Bird and Spieler, 2004). The functional relationships between epidote solid solution compositions and changes in these variables depend on the stoichiometry of reactions and enthalpies (Arnason et al., 1993).

Epidote was analysed in four different samples in this study; two samples derived from two different depth intervals in well OW-910 and, one sample from a single depth range in each of wells OW-905A and 922. No epidote sample was identified in well OW-917 for microprobe analysis. It is important to note that, due to the paucity of epidote samples analysed from wells OW-922 and 905A, it has not been possible to correlate the stratigraphy in the three wells on the basis of major and minor element contents. Such comparison would have been of great interest so as to enable critical assessment of the compositional range. Therefore, the compositional range discussed in the succeeding sections is based largely on analytical results from well OW-910. Epidote samples analysed were noted to occur in association with chlorite, titanite, magnetite and albite (e.g. Figures 30 and 31). A representative selection of chemical analyses illustrating the range in the composition of epidote is shown in Table 6. As iron in epidote is dominantly in the trivalent state (Fe^{3+}), total Fe is reported as ferric iron (Fe_2O_3) as mentioned earlier. Low totals are at least partly caused by the presence of the hydroxyl ion (OH^-) in the epidote structure, which is not detected by the microprobe. The molar proportion of pistachite in epidote from the three wells ranges between 0.23-0.65, as shown in the table below.

Chemical analyses presented in Table 6 indicate that the epidotes are relatively Al-rich types, with the exception of epidote from 1236 m in well OW-910, which is Fe-rich. There is a slight inhomogeneity in composition with respect to the Fe^{3+}/Al^{3+} ratio of the epidotes analysed. A narrow intragrain chemical compositional change exists for the major and minor oxides for the three wells. However, intergrain

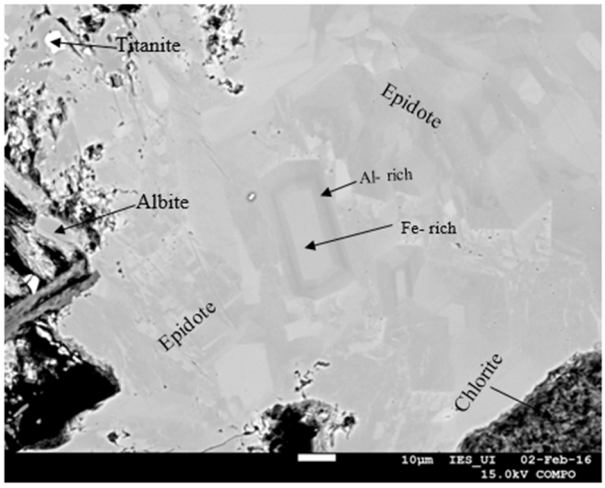

FIGURE 30: BSE image of epidote from 864 m in well OW-910. Compositional heterogeneity is clearly seen in this figure with Al-rich sections appearing darker and Fe-rich sections lighter in colour. Numerous compositional zonation patterns are represented by Al-rich rims and Fe-rich cores. Also, note the titanite inclusions in epidote

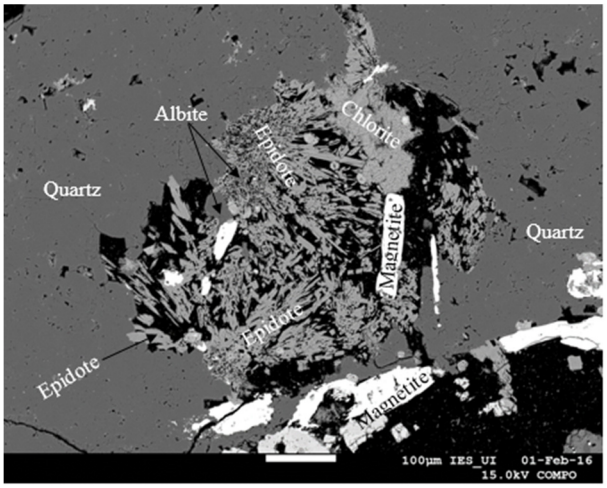

FIGURE 31: BSE image of epidote filling a vesicle from 1560 m in well OW-905A. Epidote is observed occurring as aggregates of small columnar crystals. Quartz is also noted growing in the vesicle. Black areas in the lower right hand corner, at the centre and within quartz are epoxy

TABLE 6: Representative EMP analyses of epidote from wells OW-922, 910 and 905A

Well	**OW-922**	**OW-922**	**OW-910**	**OW-910**	**OW-910**	**OW-910**	**OW-905A**	**OW-905A**
Depth	**2782 m**	**2782 m**	**864 m**	**864 m**	**1236 m**	**1236 m**	**1560 m**	**1560 m**
Analysis as Oxides, wt.%								
SiO_2	37.48	37.50	37.32	38.14	36.16	35.77	37.12	36.39
TiO_2	0.00	0.03	0.24	0.02	0.47	0.49	0.14	0.08
Al_2O_3	24.62	24.71	22.21	25.57	8.03	7.23	23.10	23.48
Fe_2O_3	12.71	12.48	16.14	11.86	19.91	21.11	14.86	13.78
MnO	0.11	0.17	0.14	0.04	0.48	0.39	1.53	1.05
MgO	0.11	0.05	0.09	0.06	0.35	0.29	0.05	0.02
CaO	22.97	22.81	23.21	23.15	32.59	33.05	21.50	22.16
Na_2O	0.02	0.03	0.00	0.00	0.02	0.01	0.00	0.01
K_2O	0.04	0.04	0.00	0.01	0.03	0.05	0.01	0.01
SrO	0.36	0.32	0.10	0.22	0.00	0.01	0.05	0.01
Total	98.43	98.13	99.46	99.08	98.04	98.41	98.35	97.00
Structural formulae based on 24 Oxygens								
Si	5.694	5.707	5.681	5.721	5.961	5.916	5.693	5.647
Ti	0.000	0.003	0.028	0.002	0.058	0.061	0.016	0.010
Al	4.409	4.432	3.984	4.521	1.559	1.409	4.175	4.295
Fe^{3+}	1.454	1.429	1.849	1.339	2.471	2.628	1.715	1.609
Mn	0.015	0.021	0.018	0.005	0.067	0.055	0.199	0.139
Mg	0.024	0.012	0.021	0.014	0.086	0.070	0.011	0.005
Ca	3.740	3.720	3.785	3.721	5.756	5.857	3.534	3.684
Na	0.006	0.010	0.000	0.001	0.005	0.004	0.000	0.002
K	0.008	0.007	0.001	0.002	0.006	0.010	0.001	0.002
Sr	0.032	0.028	0.009	0.020	0.000	0.001	0.004	0.001
Total	15.382	15.370	15.375	15.346	15.970	16.012	15.348	15.393

chemical compositional change is more pronounced in well OW-910, based on two samples derived from two different depth intervals (864 m and 1236 m). Here, a systematic change in the composition of epidote with increasing depth is clearly noticeable. This is illustrated by the change in the contents of the two dominant elements, i.e. Al and Fe, that predominantly dictate the variation in the composition of epidote (Figures 32 and 33). Al_2O_3 contents show a significant decline from ~ 24 to ~ 8 wt.% on average, whereas, Fe_2O_3 contents display a gradual increase from 14 to ~ 21 wt.% on average with depth. This is consistent with increasing average molar ratio of pistachite component with depth (Table 7).

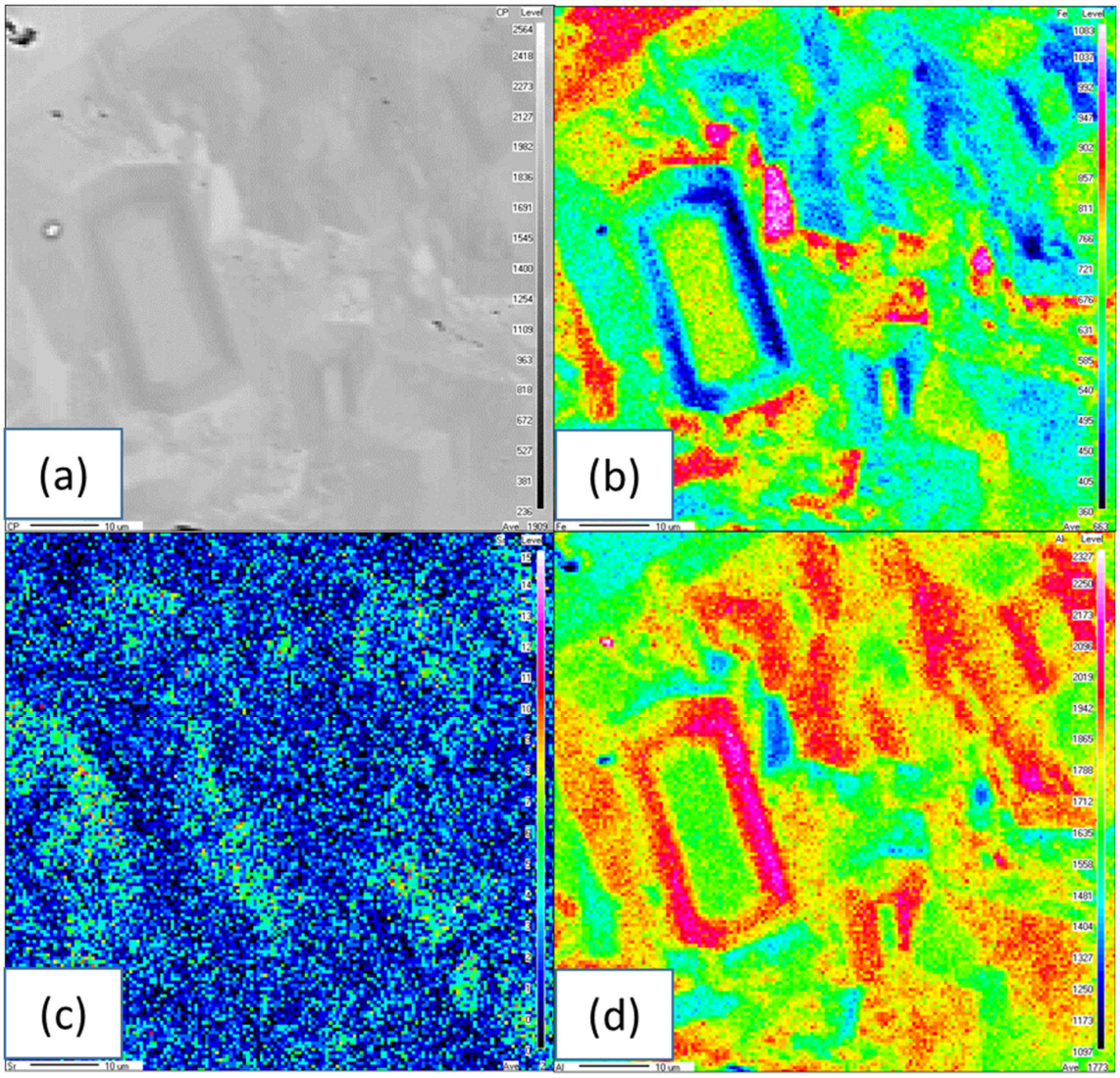

FIGURE 32: A WDS elemental map showing typical compositional zoning of epidote from 864 m in well OW-910. Grayscale map (a) represent the original composition, whereas, maps (b), (c) and (d) denote Fe, Sr and Al levels respectively

TABLE 7: Range and average molar proportion of pistachite (Xps) component in epidote

Well	Depth (m)	Molar ratio of pistachite $n_{Fe} / (n_{Fe} + n_{Al})$	
		Range	Average
OW-922	2782	0.23 – 0.24	0.235
OW-910	864	0.23 – 0.32	0.275
OW-910	1236	0.61 – 0.65	0.630
OW-905A	1560	0.29 – 0.27	0.280

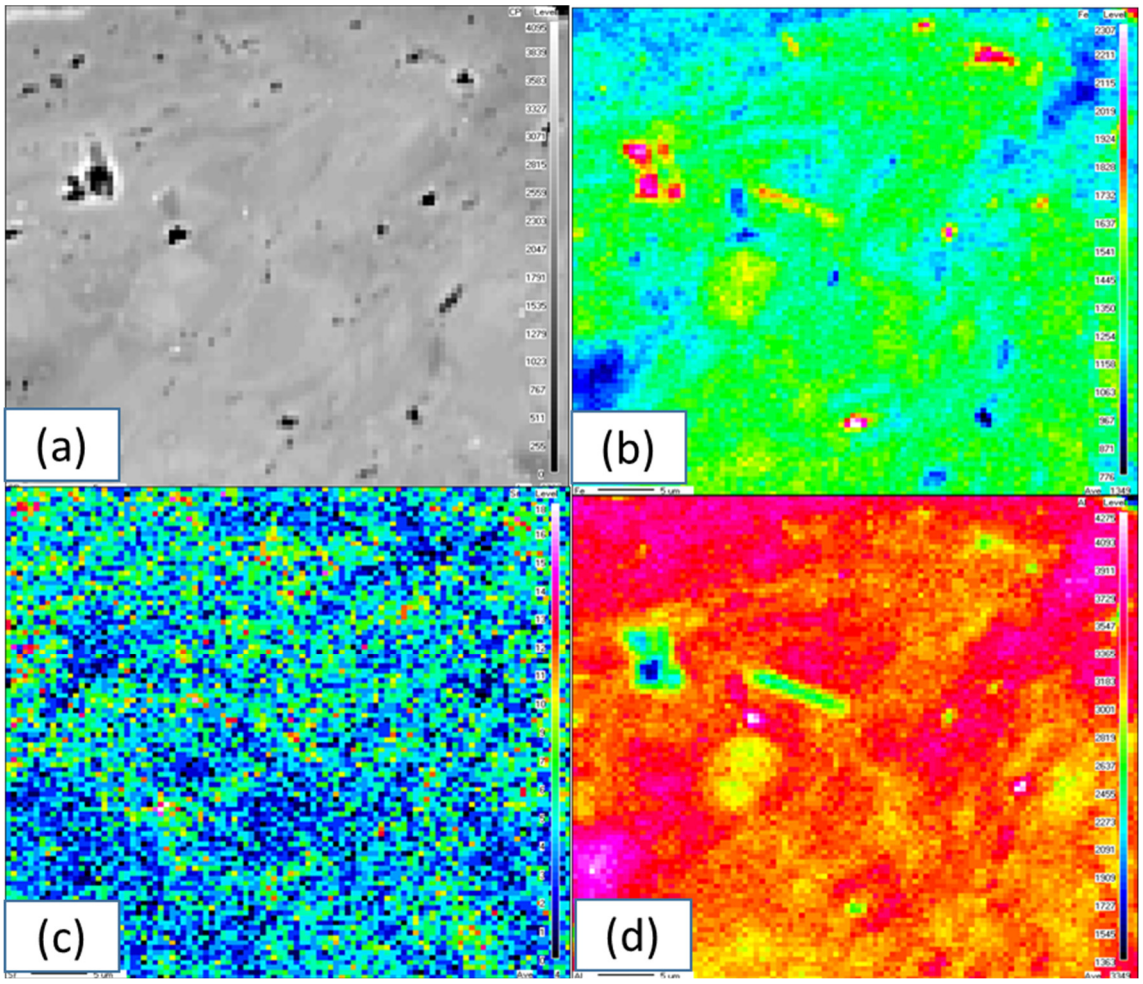

FIGURE 33: A WDS elemental map showing Fe (b) and Al (d) distribution within a single epidote grain from 2782 m in well OW-922. The darker and lighter sections in the original compositional map (a) indicates Al and Fe-rich regions, respectively. Map (c) shows Sr levels. Compositional zoning is not obvious as is the case in Figure 32

Compositional zoning, caused by variable Fe^{3+}-Al^{3+} substitution and representing phase disequilibrium, is a common feature of epidotes analysed in geothermal systems (Arnason and Bird, 1992). Other minor elements of importance observed to be in variable concentration in epidote, though, to a lesser extent, are Sr and Ti. These elements, like Al and Fe, are enriched on the rims and cores of epidote, respectively, and are clearly visible on intragrain zonation.

Chlorites are basically hydrous silicates of aluminium, magnesium and/or iron, represented by the structural formula $(Mg,Al,Fe)_{12}\,(Si,Al)_8\,O_{20}\,(OH)_{16}$. Common cation substitution involves replacement of Si^{4+} by Al^{3+} in a tetrahedral site, and, a limited substitution of R^{2+} by Al^{3+} in the octahedral site to preserve charge balance, where R^{2+} essentially is a summation of Mg^{2+} + Fe^{2+} + Mn^{2+}. Analyses of chlorite for this study were made from six samples, two each derived from different depth intervals in wells OW-922 and 910. From wells OW-905A and 917, one sample was analysed, representing a single depth range in each case. Representative chemical analyses of chlorite are presented in Table 8. A review of chlorite analyses (e.g. Dubois and Martinez-Serrano, 1998) shows that ferric iron typically constitutes < 5% of total Fe. Therefore, it is appropriate to report Fe as divalent.

It should be noted that chlorite has a strong tendency to form very fine-grained mats of needle-shaped mineral grains (e.g. Figure 34). This along with the relatively rough, uneven surface of the chlorite mats results in relatively poor analyses. As chlorite is highly hydrated, totals will always be low, but this can also mean that the mineral is relatively unstable under the electron beam, even with a relatively low probe current and wide beam diameter. Hence, the results of the EMP analyses of chlorite have to be interpreted with some caution. Most published studies (e.g. Lonker et al., 1993) have shown that

TABLE 8: Representative EMP analyses of chlorite for wells OW-922, 910, 917 and 905A

Well	OW-922	OW-922	OW-910	OW-910	OW-917	OW-905A
Depth	**2236 m**	**2782 m**	**864 m**	**1236 m**	**1870 m**	**1560 m**
Analysis as Oxides, wt.%						
SiO_2	22.20	22.12	25.02	30.45	19.58	25.61
TiO_2	0.10	0.06	0.03	0.11	0.04	0.00
Al_2O_3	14.86	13.85	12.95	16.90	16.33	19.16
FeO	30.50	32.97	12.60	17.62	34.55	34.41
MnO	0.12	0.33	0.19	0.28	0.70	2.02
MgO	5.38	5.38	17.58	15.59	5.30	7.87
CaO	0.10	0.16	0.31	0.44	0.07	0.11
Na_2O	0.75	0.18	0.03	0.09	0.47	0.02
K_2O	0.32	0.13	0.02	0.01	0.58	0.02
SrO	0.03	0.00	0.00	0.02	0.00	0.02
Total	74.35	75.18	68.73	81.50	77.62	89.26
Structural formulae based on 24 Oxygens						
Si	5.050	5.150	5.446	5.634	4.417	4.821
Ti	0.017	0.011	0.006	0.015	0.007	0.000
Al	3.985	3.727	3.323	3.686	4.342	4.250
Fe^{2+}	5.803	6.296	2.294	2.726	6.518	5.418
Mn	0.023	0.064	0.035	0.043	0.133	0.322
Mg	1.824	1.831	5.703	4.298	1.783	2.209
Ca	0.024	0.039	0.073	0.087	0.017	0.023
Na	0.329	0.080	0.013	0.031	0.207	0.009
K	0.092	0.039	0.005	0.004	0.167	0.005
Sr	0.004	0.000	0.000	0.002	0.000	0.003
Total	17.151	17.236	16.898	16.526	17.591	17.060

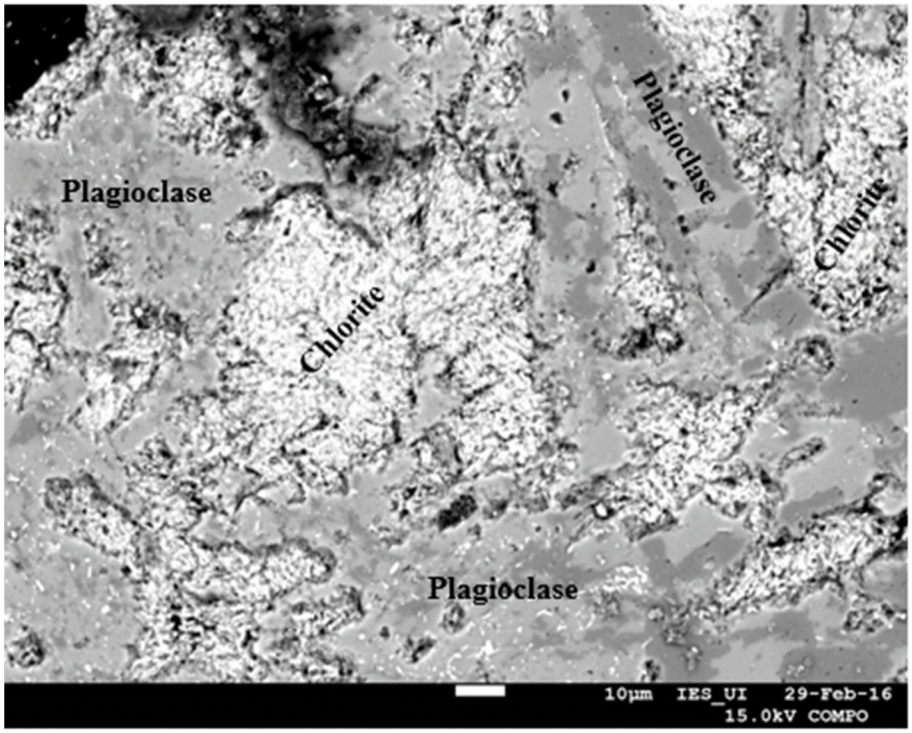

FIGURE 34: BSE image of chlorite replacing plagioclase at 1870 m in well OW-917

Chemical analyses of chlorites from the four wells indicate that they are Fe-rich varieties except from 864 m depth in well OW-910 (Table 8). Most of the chlorites fall in the brunsvigite compositional field going by the classification scheme proposed by Dubois and Martinez-Serrano (1998). Si, Al, Fe and Mg are in appreciable amounts in chlorite in the four wells, whereas Ti, Mn, Ca, Na, K and Sr are present as minor or trace elements. Variations in Fe^{2+} / (Fe^{2+} + Mg) ratio in chlorite from hydrothermally altered rocks (Table 9) has in many cases (e.g. Lonker et al., 1993) been applied to infer permeable zones in a well.

TABLE 9: Molar ratio of chlorite from wells OW-922 and 910

Well	**Depth (m)**	**Molar ratio of chlorite n_{Fe} / (n_{Fe} + n_{Mg})**
OW-922	2236	0.76
OW-922	2782	0.77
OW-910	864	0.29
OW-910	1236	0.39

5. DISCUSSION

5.1 Lithological units

Well OW-922 is a step-out vertical well drilled to a total depth of 2990 m CT to the east, in the plain between Olkaria Domes field and Longonot volcanic centre. The main purpose of drilling the well was to appraise the geothermal resource potential in the area, so as to expand production drilling outside the already congested proposed Olkaria caldera structure. This, also comes at a time of renewed focus by the Kenyan government on accelerating development and utilisation of geothermal resources for electricity generation in the country. Based on analysis of drilling cuttings through binocular and petrographic microscopy and ICP-OES, the sub-surface strata penetrated by the investigation well comprise pyroclastics, tuffs, rhyolite, trachyandesite, basaltic trachyandesite, basalt, trachydacite and trachyte. From the existing geologic well logs (KenGen in-house data), it is evident that no other well drilled in Olkaria has intersected such thick sequence of pyroclastic deposits, extending continuously for about 300 m, as is the case with the study well. The observation is perhaps caused by the well's proximity to the Longonot volcanic complex.

Stratigraphically, the Longonot pyroclastics (light grey to grey in colour) overlie the Olkaria pyroclastics (yellowish brown in colour), attesting that the former are younger in age. Like in most Olkaria wells, trachyte is still the dominant rock unit in the study well, in some cases extending steadily downward to reach a thickness of about 1200 m (e.g. between 1700-2900 m). The unit forms the reservoir rock in the study well. Clearly, the rhyolites are markedly less abundant in the study well relative to wells OW-905A, 910 and 917, perhaps caused by the well's location being outside the main Olkaria volcanic zone. As a result, rhyolitic volcanism seems to have been majorly confined to the proposed Olkaria caldera structure. No intrusive rocks were intersected by the well. Intrusives result from the injection of magma into the overlying country rock and commonly serve as a source of heat to shallow levels of the geothermal system. Based on this observation, it is probable that pre- and post-caldera magmatism associated with the OVC had minimal effect in the area surrounding the well. Lack of intrusive rocks in the well further attests to the location of the well, being outside the main Olkaria volcanic zone.

5.2 Hydrothermal alteration

Hydrothermal alteration sequences provide a significant insight into the history of a geothermal system. Hydrothermal alteration observed in the study well is essentially made up of two components: (a) replacement of primary components in the rocks by alteration minerals, and (b) precipitation of alteration minerals into open spaces (veins, fractures and vesicles) in the rock. Generally, there is scarcity of high-temperature alteration minerals in well OW-922. The top most zone of the well (0-190 m) contains relatively fresh rocks, including a sequence that do not show any indication of geothermal interaction and at the most show moderate oxidation due to groundwater circulation. The subsequent zone between 190 and about 450 m is dominated by relatively low-temperature alteration mineral assemblages (e.g. zeolites, smectites, chalcedony), signifying that inferred alteration temperatures are < 200^{o}C. Petrographic examination of the rock samples between this interval indicate that the primary phases replaced are mostly volcanic glass and olivine, as seen in Table 3. A prograde mineralogical change, marked by transition from secondary quartz, wairakite, albite, illite, chlorite and epidote is evident between 476 m to about 1798 m depth. The occurrence of epidote, which is regarded as one of the most important greenschist alteration mineral assemblages (e.g. Bird and Spieler, 2004) is relatively spasmodic. In most cases, the occurrence of the mineral is observed as faint colouration, possibly reflecting that equilibrium between the host rocks and reservoir fluids was seldom achieved. It is worth noting that certain minerals, including calcite and pyrite form at both low and high temperatures (i.e. between ~ 50-300°C), thus cannot be totally relied upon as accurate temperature indicators (Brown, 1978). Below 1038 m depth to the well bottom, mixed layer clays (MLCs), occurring in different combinations (smectite/illite, smectite/chlorite and smectite/illite/chlorite), and calcite are the dominant alteration mineral phases.

Clay mineralogy in the study well differs somewhat from clay alteration commonly observed in other Olkaria wells. In particular, the persistence of MLCs to the bottom of the well possibly reflects modification of the composition of hydrothermal fluids. This is in agreement with reports of various authors (e.g. Steiner, 1977; Kristmannsdóttir, 1979) who found out that the distribution of clay minerals in geothermal areas depends on the fluid chemistry and thermal structure of the field. Studies of chemical composition of the fluids are, however, required to prove the case. In previous studies in Olkaria (e.g. Mwania et al., 2013; Musonye, 2015), it is observed that the occurrence of MLCs is mostly restricted to depths above 1500 m. MLCs in this well are characterized by well developed smectite peaks at greater depths, for example at 2616, 2840 and 2918 m depth, just to mention a few, perhaps indicating that temperatures are not high enough. The association of MLCs with haematite and abundant calcite, particularly towards the bottom of the well could reflect that temperatures are relatively low in this region.

5.3 Permeability and comparison of temperatures

Feed zones below the production casing in a well can either be cold or hot. Cold feed zones, depending on the size, may ultimately cool the well, rendering it less productive. On the other hand, hot feed zones in many cases are known to maximise well productivity. In the study well, feed zones inferred demonstrate a relationship between geological observations, variations in drilling parameters and kinks in temperature recovery logs. However, it is key to point out that intrusion related feed zones, which are common in wells OW-905A, 910 and 917 are not present in well OW-922 as already discussed. Based on analysis of the feed zones in relation to the indicators mentioned above, it is noted that most of the feed zones are small, leading to the conclusion that permeability in the well is limited. This observation is also supported, for example by the failed injection test where the well did not accept water, absence of clear pivot point and total failure of the well to discharge after 49 days of heat-up. The pivot point is fundamental in the sense that it is ordinarily used to infer the best feed zone in a well. At this point, the pressure is nearly constant. Moreover, it is probable that intense calcite deposition, particularly towards the bottom of the well, clogged the once present primary and secondary fluid channels. It is also observed that a correlation between secondary mineralisation and identified feed points is restricted, and the values of key indicators of water/rock interaction (i.e. Na_2O and K_2O) do not show any large shift within and in the vicinity of the feed zones as would be expected.

A comparison of measured formation and alteration temperatures (Figure 22) indicates that the geothermal system around the study well has substantially been disturbed. It is apparent that the inferred alteration temperature plots higher than the measured formation temperature. This demonstrates that past temperatures were substantially higher than the present measured ones. Temperature profile argues in favour of this observation, showing a maximum temperature of 127^{o}C between ~2400- 2500 m depth (Figure 21), below which there is a reversal in temperature gradient to the well bottom. This is inconsistent with the inferred alteration temperature of about 240^{o}C, denoted by the presence of epidote. It is necessary though to mention that the measured formation temperature was taken only after 49 days recovery period. As a result, the formation temperature may not be representative enough, since the geothermal system had likely not fully stabilized following the long drilling time of the well. An up to date temperature log would provide a true reflection of the current state of formation temperature in the well. It is, therefore, likely that significant cooling has occurred in the geothermal system around well OW-922 over time.

Other possible indications of cooling in the well are demonstrated by the extensive deposition of calcite (e.g. Figure 21), especially towards the well bottom (i.e. ~ 2240-2990 m). A reasonable explanation for the intense calcite deposition, which is consistent with the argument of Simmons and Christenson (1994), implies heating of the colder peripheral fluids entering the geothermal system by the host rocks, consequently favouring carbonate precipitation. This observation is also in accord with the interpretation put forward by Musonye (2015) to explain intense calcite deposition in well OW-917. The latter was drilled along the proposed caldera structure (Figure 3) and exhibits more or less similar hydrothermal alteration features to well OW-922. Cases of calcite superimposed on epidote (e.g. at 2782 m depth) have been observed by several authors (e.g. Mortensen et al., 2014; Franzson et al., 2008) and interpreted

to reflect carbonate deposition during cooling of the system by influx of colder fluids into the reservoir. However, fluid inclusion studies would be necessary to provide detailed insights about the temporal evolution of the geothermal system around the study well.

Equally, haematite is observed in moderate amounts (i.e. at level 2 on the scale of 1-3) between 2342 and 2982 m depth. In this case, the occurrence of haematite can be interpreted to suggest influx of oxygen-rich cooler groundwater into the system. The geothermal system around the study well can therefore, be described as episodic rather than continuous. An episodic geothermal system refers to a system where some changes (either heating or cooling) has occurred over time based on differences between inferred alteration and measured (or calculated) formation temperatures. On the other hand, a continuous system is where the inferred alteration and measured (or calculated) formation temperatures are more or less in a state of equilibrium (Brown, 1978).

Figure 35 shows a possible conceptual model based on the outcome of the study.

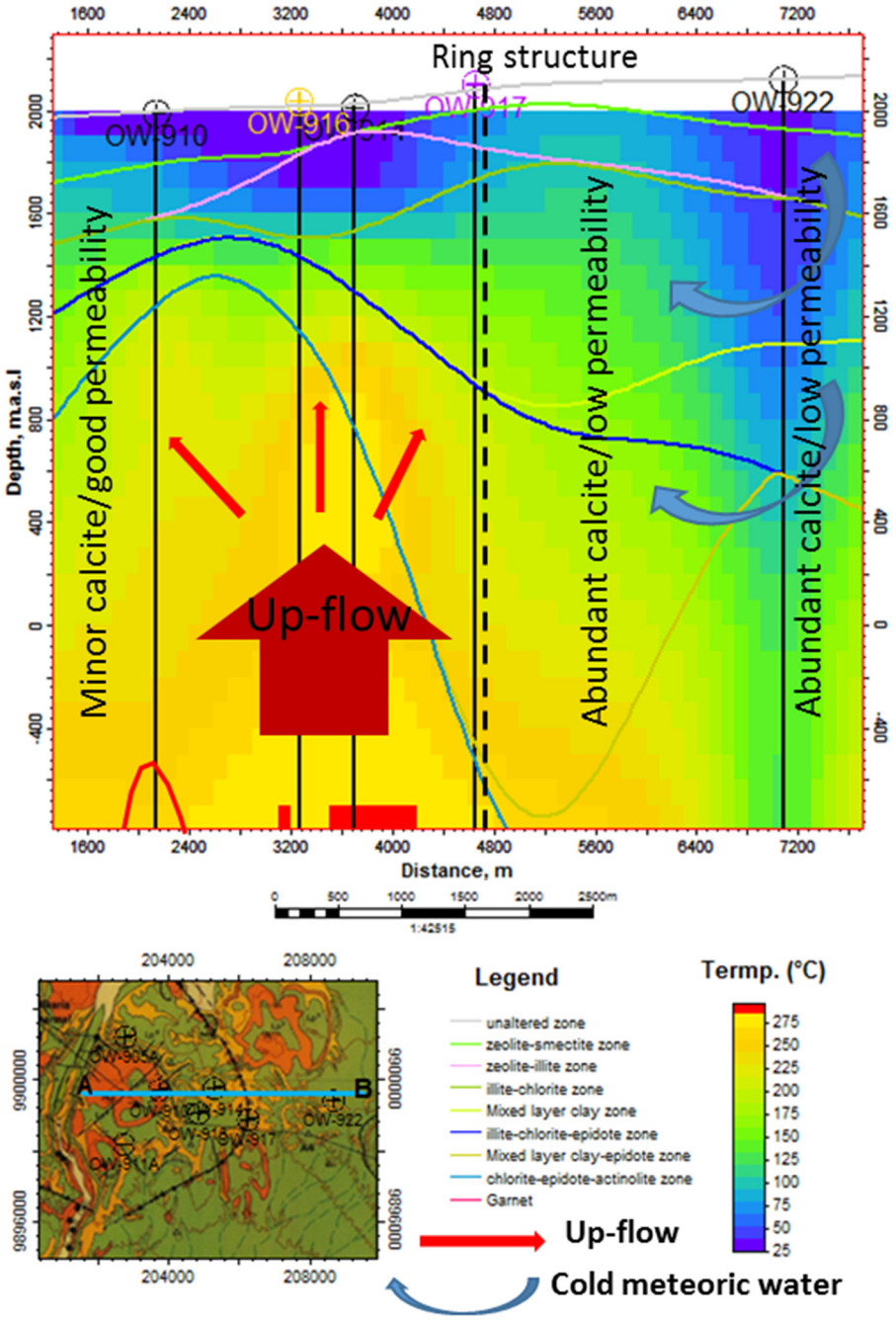

FIGURE 35: A possible conceptual model based on outcome of the study, along the traverse A-B

5.4 Rock composition

Rocks from the study well show a complete range of compositions from basalt to trachyte or rhyolite. The dominance of evolved rock suites relative to mafic and intermediate rocks implies high degree of differentiation of the parental magma. Peccerilo et al. (2007) observed that the relative scarcity of the intermediate rocks are related to their high viscosity, which inhibits them from erupting. Even though the more silicic magmas (pantellerites and comendites) still have high viscosities, they tend to be associated with much lower density. This feature, alongside the high volatile contents (e.g. CO2, H2O, Cl and F) of silicic magmas, helps to drive them out after high degrees of fractional crystallisation from the magma reservoirs (Ronga et al., 2009). Based on the TAS classification scheme, the prevalence of trachytes is in accord with the general stratigraphy of Olkaria, which is composed primarily of trachytes, except for the Olkaria west fields.

5.5 Hydrothermal alteration effects on rock chemistry

Interaction of high-temperature fluids with host rocks (hydrothermal alteration) in the geothermal system around well OW-922 has produced changes in the rocks. Essentially, hydrothermal alteration is a very complex process involving a chemical, mineralogical and textural changes of the host rock. The process results from the interaction of the wall rock with hot aqueous fluids (Pirajno, 1992). These fluids deliver the chemical reactants and take away the aqueous reaction products. The complex water-rock interaction process has undoubtedly changed contents of the chemical elements in the altered rocks. In this case, a direct method, based on comparison of elemental concentrations has been applied to determine the effects of hydrothermal alteration on selected major and trace elements. Even though this method serves the purpose to some extent, a distinct disadvantage is that it does not put reliable constraints on the effect of alteration on element mobility in altered rocks.

Other methods, such as the statistical approach (e.g. Student t-tests) and mass balance calculations, are known to yield more coherent results. Quantification of alteration effects on an element is based on the concept of element mobility. The amount of hydrothermal alteration is very often correlated with an element's ionic potential (charge/radius ratio) (e.g. Verma et al., 2005). Consequently, highly mobile elements are characterised by low ionic potential (< 0.03 pm^{-1}) and tend to be easily leached away by the geothermal fluids as hydrated cations. These elements exhibit large variations (scatter) as a consequence of the alteration process and are exemplified here by Na, K, Ba, Sr, and Rb. In contrast, most immobile elements are characterised by high ionic potential (> 0.10 pm^{-1}) and tend to be retained in the host rocks since they are not easily leached away by hydrothermal fluids. In this study, these elements include Ti, P, Zr, Y, Sc, La and the transition metals (Co, Cr, Ni, V).

5.5.1 Effects on major element geochemistry

Selected major elements have been plotted against SiO_2 to decipher alteration effects on major element geochemistry (Figure 36). SiO_2 has been used as the reference or independent variable because it is a nearly conservative element (oxide) during hydrothermal alteration processes. This view has been advocated by Verma et al. (2005), who have presented convincing experimental and theoretical results. The authors suggest that SiO_2 contents of most geothermal waters are generally low ($< 0.15\%$). As a result, the SiO_2 contents of the altered rocks should be more or less unaffected, and hence, the use of Si or SiO_2 as a conservative independent element or oxide for assessing alteration behaviour of other elements (or element ratios) is widely accepted.

The variation of selected major elements vs. SiO_2 indicates that hydrothermal alteration has had insignificant effect on Al_2O_3 and MnO in comparison with Na_2O and K_2O. Na_2O and K_2O display some scattering, which is more pronounced in K_2O and, are traditionally known to be highly mobile during hydrothermal alteration (e.g. Verma et al., 2005). These elements are the dominant constituents in alkali feldspar, which is a primary rock forming mineral in trachytes and rhyolites. Consequently, this raises the possibility that, as the two elements are highly mobile, they have been affected by post-magmatic alteration processes. The preferential mobility of the alkalis compared to aluminium during

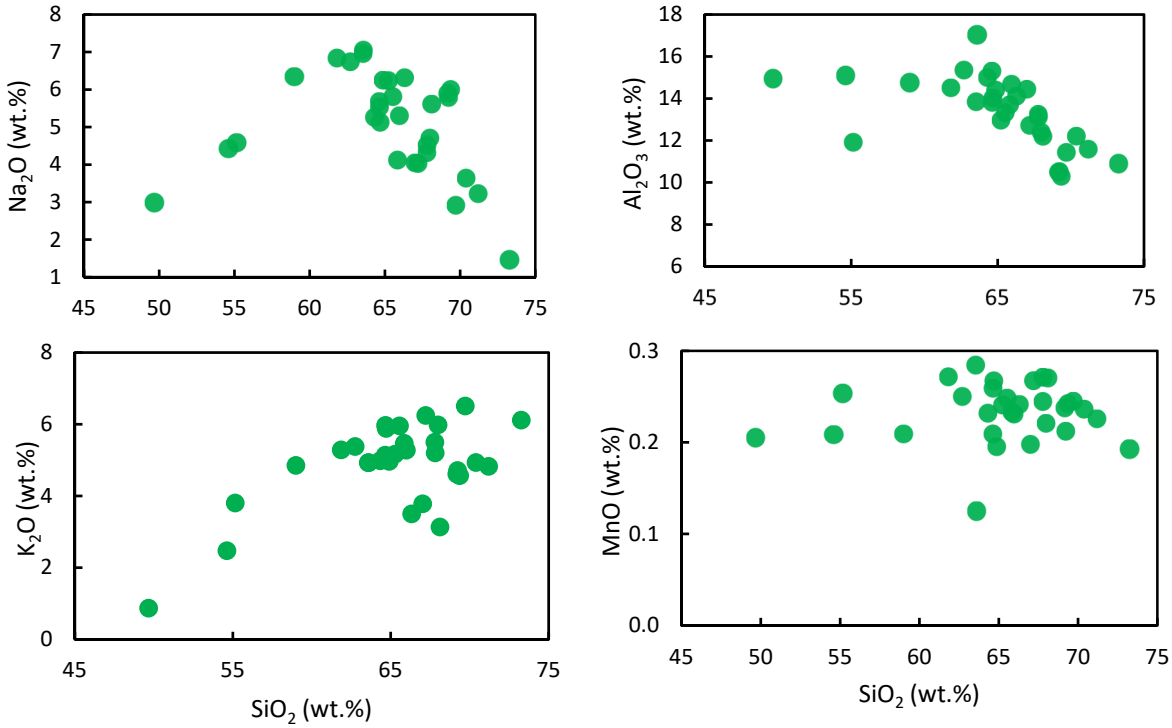

FIGURE 36: Variation diagrams showing the concentrations of Na_2O, Al_2O_3, K_2O and MnO against SiO_2

hydrothermal alteration, could also be responsible for the marked metaluminous character of a majority of the samples in the study well. This is expressed by molar proportions $Al_2O_3 > Na_2O + K_2O$. The cause of scattering of MnO is not intuitively obvious, but seems to be related to variable degrees of fractionation as opposed to a true scatter. Another possible explanation could be the result of background noise introduced by using analyses of highly porphyritic samples (e.g. Wilson, 1989).

5.5.2 Effects on trace element geochemistry

A plot of selected trace elements against Zr (Figure 37) have been used to assess the alteration effects on trace element geochemistry. Zr has been used as an independent variable owing to its large range of variation and being regarded as a highly immobile element in volcanic rocks (Franszon et al., 2008).

From the selected trace element vs. Zr. plots, it is evident that hydrothermal alteration has the least effect on Sr, Ni and Ba, but has severely mobilised Rb, as shown by large scattering. La and Y are comparatively inert and not much affected by hydrothermal alteration processes. In previous studies (e.g. Verma et al., 2005), the two elements have been considered as typical fluid-immobile elements. Rb is an alkali metal and, is a major constituent of alkali feldspars. The element is highly mobile and is easily leached from the rocks by fluid components of the hydrothermal alteration process. Sr, even though normally considered mobile, has been least affected by alteration.

It must be emphasised that the ICP-OES analysis did not include measurement of loss on ignition (LOI). The latter has been used in many cases (e.g. Franszon et al., 2008) to monitor alteration. Highly altered rocks tend to have high LOI values, whereas, the unaltered or slightly altered rocks are characterised by low LOI values. In addition, Verma et al. (2008) observed that high LOI are associated with low Na_2O abundances, strongly indicative of Na loss during alteration processes.

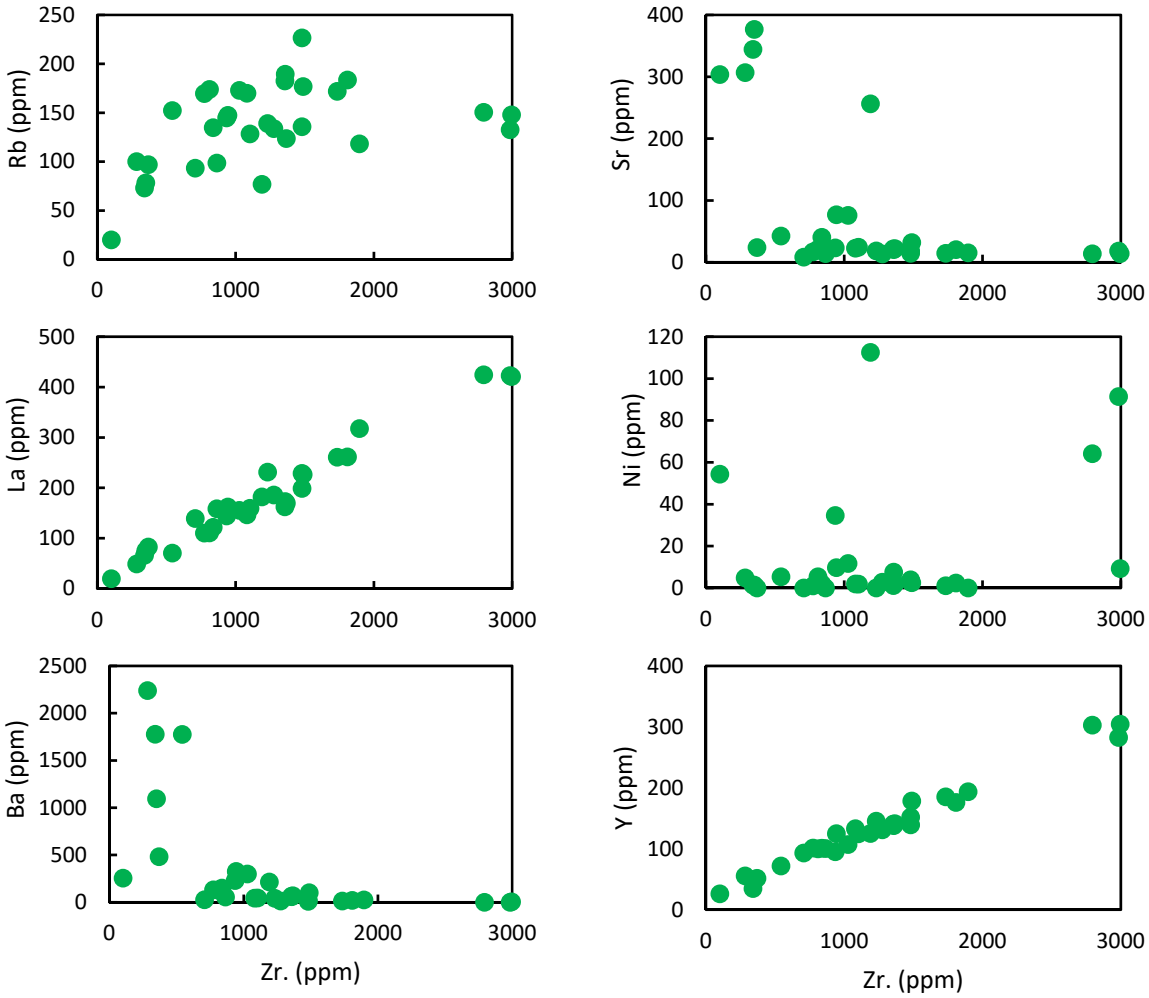

FIGURE 37: Variation diagrams showing the concentrations of Rb, Sr, La, Ni, Ba and Y against Zr

5.6 Magmatic differentiation processes

Magma differentiation or segregation processes are central to understanding the origin of sequences of volcanic rocks exhibiting systematic variations in composition, despite being obtained from a likely analogous source component. Insights into these processes are derived from studies of lavas or intrusions exposed on the surface or obtained through drilling of the sub-surface geological formations, as is the case in the present study. Importantly, the rocks provide excellent opportunity of tracing changes in major and trace elements during magmatic evolution. Models of magma differentiation, including magma mixing/mingling, crustal contamination, partial melting and fractional crystallisation, have been tested by many authors (e.g. Wilson, 1989; Omenda, 1997; Peccerillo et al., 2007).

To decipher the differentiation mechanisms for the sub-surface rocks in well OW-922, SiO_2 was chosen as the abscissa or index of differentiation owing to its abundance and wide concentration range (59-73 wt.%). Consequently, it can be used to observe the progress of differentiation processes. In spite of the wide range of SiO_2 contents, it is pertinent to note that majority of the samples have silica values clustering between 63 and 73 wt.%. All the major oxides and trace elements have been plotted against SiO_2 on Harker diagrams (Figures 23 and 24) and the interpretations discussed below.

5.6.1 Major elements

Progressive depletion in major element oxides, such as FeO (total iron expressed as ferrous oxide), MgO, CaO, TiO_2 and P_2O_5 show curved to near-curved trends in the variation diagrams. Whole-rock

SiO_2 contents are negatively correlated with these elements, indicating that simultaneous fractional crystallisation process of mafic mineral assemblages from a basaltic parental magma is a possible cause. The inverse trend observed between FeO and MgO vs. SiO_2 (Figure 23) can be interpreted as implying the separation of ferromagnesian mineral phases (olivine and clinopyroxene) from the melt during early stages of crystallisation (e.g. Hardarson, 1993). Similarly, the decrease in CaO content strongly suggests that the mafic to intermediate magmas evolved by fractionation of an assemblage dominated by plagioclase and clinopyroxene.

The interpretation of TiO_2 vs. SiO_2 could be related to fractionation of Fe-Ti oxides (e.g. ilmenite and/or titano-magnetite) from the intermediate to silicic rock suites. According to Wilson (1989), TiO_2 is incompatible in the main minerals of basalt. As a result, its concentration generally increases significantly in the residual liquid after crystallisation of olivine and plagioclase during early stages of crystallisation. The decrease in P_2O_5 as SiO_2 content increases is ascribed to the beginning of apatite crystallisation in the intermediate to silicic rocks, resulting in a less phosphor content of the melt.

The down-turn in Na_2O abundances in samples containing greater than 64 wt.% SiO_2 (Figure 23) denotes the point at which plagioclase fractionation becomes a controlling factor in the compositional evolution of the residual liquid. This observation is consistent with the gradual decline in Al_2O_3 contents, which would only require fractionation of plagioclase, and to a lesser extent alkali feldspar (Weaver et al., 1972). The trend observed for CaO/ALK ratio against SiO_2 (Figure 22) is consistent with a fractional crystallisation model (e.g. Weaver et al., 1972). In general, the different slope of trends for the major oxides vs. SiO_2 is likely influenced by the fractionating minerals and their proportions. Low P.I. (0.26-1.03) of the samples analysed could probably be attributed to significant loss of the alkalis which are easily leached away during hydrothermal alteration processes as discussed earlier. Based on this observation, it is reasonable to suppose that the loss of Na_2O and K_2O in this well was sufficient enough to make all but two samples (i.e. 1106 and 1142 m) appear metaluminous (i.e. $Al_2O_3 > Na_2O + K_2O$).

5.6.2 Trace elements

The relative enrichment and/or depletion of trace elements offers valuable insights about the source characteristics or petrogenetic process of any volcanic rocks suite. It is important to note that trace elements do not form any major rock forming minerals themselves but mostly enter crystallographic sites in the most common mineral phases by substitution. Various mineral phases may either accept (compatible) or largely exclude (incompatible in such phases) these elements into their crystal structure. Consequently, the use of trace elements to diagnose petrogenetic processes leads to better understanding of the nature and composition of the mineral assemblages with which the magma may have previously equilibrated. Although the trace elements graphics generally show more scattering (Figure 24) compared to the major element oxides (Figure 23), systematic variations with SiO_2 contents are clearly evident.

The decrease in Co, Cr, Ni and V with increasing SiO_2 content (Figure 24) can be interpreted to signify fractional crystallisation of mafic mineral assemblages (olivine and clinopyroxene) from a basaltic parental magma. From the description of the lithologies in well OW-922, it is noticeable that olivine and clinopyroxene are frequently observed as the dominant phenocryst phases in majority of the mafic rocks. Nickel partitions easily into olivine while V is mainly incorporated into clinopyroxene in mafic rocks (Wilson, 1989). The depletion of Sc towards more evolved rocks is consistent with the fractionation of olivine and plagioclase mineral phases. Cobalt follows similar pattern as Sc and is known to partition strongly into olivine (Weaver et al., 1972). Extraction of Cu is usually not related to any precipitating major mineral phases but can be linked to the separation of a sulphide minerals (Weaver et al., 1972).

The main phase affecting Sr partitioning in the mafic rocks is plagioclase and to a lesser extent alkali feldspar. Therefore, the systematic enrichment in Sr contents in the mafic and intermediate rocks can be accounted for by the accumulation of plagioclase (and possibly alkali feldspar). Additionally, incorporation of Sr into apatite or titanite may as well contribute to its reduction in the more evolved lavas (Weaver et al., 1972). However, most of the trend observed in Sr. vs. SiO_2 plot can be attributed to variable degrees of plagioclase fractionation. ITEs, e.g. Y, Zr, Rb and La, show a relatively good

positive correlation with increasing SiO_2 contents despite some scattering (Figure 24). The correlation in Rb vs. SiO_2 can be termed strong correlation, whereas for Y, Zr and La vs. SiO_2 is a moderately strong correlation. Increase in ITEs concentrations with increasing SiO_2 content can satisfactorily be interpreted to mark their incompatible behavior, where the melt become steadily enriched in these elements as fractionation proceeds.

The strong depletion of Ba (< 20 ppm) in rhyolites can be attributed to fractionation of sanidine. The element becomes compatible when alkali feldspar appears in the phase assemblage of intermediate and silicic melts. Here, it easily substitutes for potassium in K-feldspar, specifically the sanidine. The latter is one of the prominent phenocryst phases in the rhyolites. It is important to mention that fractionation of sanidines also ultimately affects the concentration of potassium in the residual liquid. On the other hand, accumulation of sanidines could possibly account for Ba enrichment in the trachytes. The differentiation trends seen in the major and trace element systematics (Figures 23 and 24) are consistent with a fractional crystallisation process for the evolution of the rocks in well OW-922.

5.6.3 Assessing other differentiation mechanisms

To assess other petrogenetic processes responsible for the generation of these rocks besides fractional crystallisation, plots of incompatible vs. incompatible elements are shown below. Zr is used as an independent variable owing to its large range of variation, high incompatibility and relatively immobile nature during hydrothermal alteration (Franzson et al., 2008).

A basic requirement for fractional crystallisation processes for any two ITEs is that the two elements must plot on linear trends which can be extrapolated to the origin (Omenda, 1997). In his pronouncement, fractional crystallisation does not significantly change ratios of trace elements with analogues degrees of incompatibility. This requirement has been successfully fulfilled by La and Y vs. Zr plots. However, fractional crystallisation cannot be single-handedly put forth to explain all the geochemical features depicted by La and Y vs. Zr plots.

Deviations from the continuous trends in the incompatible element plots (La/Zr, Y/Zr) observed in the rhyolites suggest that other processes (e.g. through partial melting of crustal rocks or magma mixing) at least contribute to their petrogenesis. These deviations are exhibited predominantly by the rhyolites between 1106-1142 m and 2420-2570 m depth. Previous studies of the magmatic differentiation mechanisms for the surface rhyolites in Olkaria (e.g. Macdonald et al., 2008) agree with the observation made in the present study. In their study, the authors established that rhyolites were formed primarily by fractional crystallisation of metaluminous trachytic magmas and to a lesser extent by partial melting of syenites. The trachytes themselves, were formed by the fractional crystallisation of basaltic magmas through mugearites and benmoreites (Marshall et al., 2009).

It is therefore possible that rhyolites plotting off the main trend were generated by partial melting of the syenites. However, no clear theory based on geochemical grounds has been put forward by the authors to exhaustively explain the origin of rhyolites by partial melting, even though there is a high probability that the process was promoted by fluxing of volatiles emanating from underlying magmas. Evaluating the degree of partial melting is, however, not feasible, because doing so requires knowledge of partition coefficients for the relevant mineral phases, source compositions and the depth at which melting occurs. These are rather poorly constrained.

5.7 Comparison of surface and sub-surface samples

A comparison of surface samples from Olkaria and neighbouring minor eruption centres and sub-surface samples from the study well, and wells OW-905A, 910 and 917 (Figure 27) clearly points towards a common petrogenetic mechanism for these rocks. This is exhibited by both samples plotting within similar fields on the TAS diagram (Figure 27). On this account, it is reasonable to suggest that magma from these volcanic centres was generated by a common differentiation process, possibly from a similar parental magma. Only detailed radiogenic isotope studies can convincingly prove the case.

Correspondingly, comparison of the geochemical data for selected major and trace elements for the four wells (Figures 28 and 29) demonstrate a perfect overlap across the whole range of compositions. A more realistic interpretation would be that the trends displayed by the two groups of elements are related by a common evolution mechanism.

These results are in agreement with the interpretations of Musonye (2015), who presented convincing results in his study of the petrochemistry of wells OW-905A, 910 and 917. The author construed high degree of correlation between certain major and trace elements vs. an evolution index as being consistent with predominantly extended fractional crystallisation, or even requiring fractional crystallisation as a necessary condition. Since the rocks from well OW-922 are geochemically comparable with rocks from wells OW-910, 917 and 905A, a petrogenetic connection seems likely between the rocks in the four wells.

Whilst these relationships are consistent with a fractional crystallisation process, it is not necessarily the only mechanism that accounts for all the geochemical characteristics observed. Other differentiation processes cannot be completely ruled out, however, limited role they play in the evolution of these rocks. To illustrate this point, plots of two ITEs plotted against each other have been made, as in Figure 38. Results of these plots (Figure 39) coincide with interpretations made for Figure 38. Once again, the unanswered question remains whether these rocks are derived from similar or different parental magma. Once again, only detailed radiogenic isotope studies can resolve the impasse.

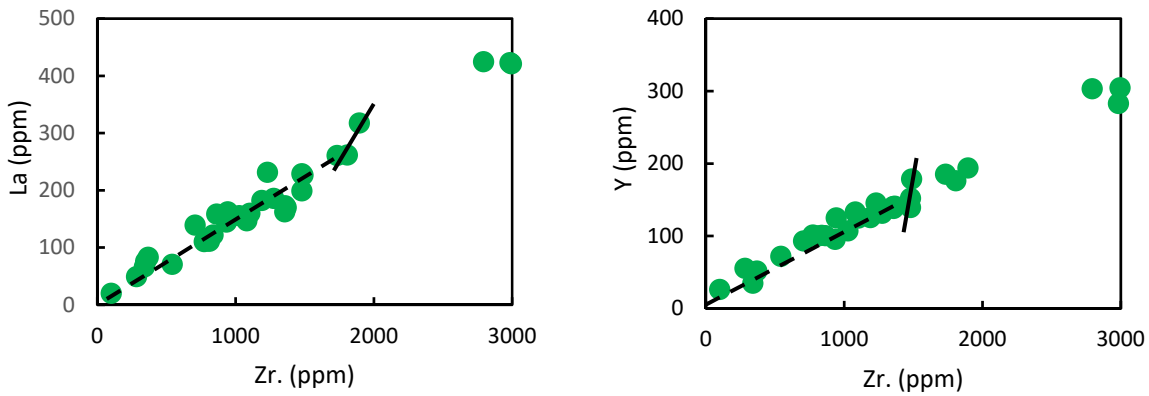

FIGURE 38: A plot of La vs. Zr. and Y vs. Zr. showing different magmatic differentiation processes. The dotted and continuous lines indicates fractional crystallisation and other petrogenetic processes, respectively

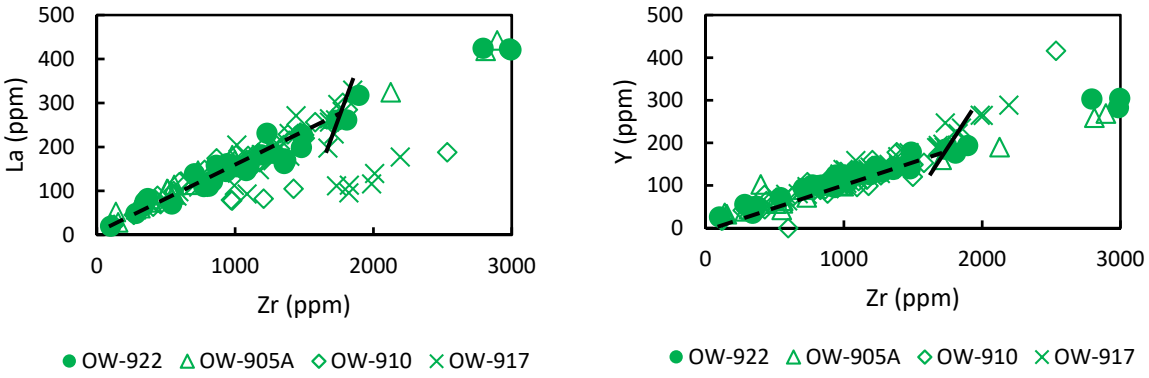

FIGURE 39: Harker's variation diagrams between various pairs of incompatible trace elements displaying fractional crystallisation (dotted line). The flexure from the main trend (continuous line) represent other magma differentiation processes

5.8 Compositional variation of alteration minerals

5.8.1 Epidote

Measured chemical compositions of different epidote crystals, derived from two different depth intervals in well OW-910, show wide and concomitant variations in Al and Fe contents. Variations in the Fe^{3+}-Al^{3+} contents of epidote observed presumably reflect changes in fluid composition during the formation of the mineral. Epidote composition depends directly on the ratio of the activities of $Fe^{3+}$and Al^{3+} in the fluid. However, aqueous complexation of Fe^{3+} and Al^{3+} with other anions (e.g. $SO_4^{2-}, CO_3^{2-}, Cl^-, OH^-$, etc) may cause the composition of epidote to depend on fCO_2, pH and chloride concentration in the fluid phase (Arnason et al., 1993). Thus, changes in fluid composition during the evolution of epidote may result in variations in $Fe^{3+}$and Al^{3+} exchange without necessarily reflecting changes in temperature or pressure.

Other plausible thermodynamic mechanisms to account for the variation in epidote composition in well OW-910 are changes in fO_2 and the oxidation state. Diverse experimental results (e.g. Arnason et al., 1993) have demonstrated that fO_2 strongly controls the Fe-content of epidote. Values for fO_2 for the Olkaria geothermal system have not been determined, but such studies would be of great interest. According to the authors, epidote is the most Fe-rich in the presence of haematite-magnetite oxygen buffer and becomes more aluminous with decreasing fO_2, as the proportion of ferric iron in the system decreases. In addition, the authors noted that epidote stability increases with increasing fO_2. The latter expands the P-T boundaries of the epidote stability field. Like in the Salton Sea geothermal system, epidote in well OW-910 is known from binocular observation and optical petrography of cuttings to occur alongside haematite. This observation is closely compatible with the relatively high fO_2 calculated for the Salton Sea geothermal system (Bird and Spieler, 2004). Epidote in haematite-bearing assemblages is traditionally known to be more Fe-rich (Bird et al., 1988).

Additionally, results of epidote analysis at 1236 m depth display a positive relationship between the relatively high Fe-content of epidote and inferred level of oxidation. This is marked by concomitant increase in the oxidation state of host rocks from 864 m to 1236 m depth. The enrichment of Sr and Ti in the rim and core of epidote, respectively suggest that epidote could be an important repository for these elements, mobilized through hydrothermal alteration. Results of previous analyses of Icelandic epidotes, for example in the Hengill geothermal system (e.g. Bragason, 2012), points to a more or less similar picture where, Sr contents are noted to increase progressively towards the rims. Based on the authors' interpretation, increase in Sr contents very likely reflects extensive breakdown of plagioclase.

Variations of the average mole fraction of pistachite (Xps) contents of epidote in this well is satisfactorily correlated with depth, and is in agreement with the range in some well known geothermal systems of the world (e.g. Bird and Spieler, 2004, Bird et al., 1988). Marks et al. (2010), while studying epidote in the Reykjanes and Nesjavellir high-temperature geothermal systems in Iceland observed an increase in the average molar ratio of pistachite with depth. The authors interpreted this observation to indicate an increase in temperature. In the Olkaria geothermal system, well OW-910 is a high-temperature well with regard to measured down-hole formation temperatures, reaching a maximum of about 300°C (Musonye, 2015). The distribution of formation temperature in this well, therefore, is consistent with the relationship between the molar ratio of pistachite and temperature advocated by Marks et al. (2010). Temperature exerts a major influence on the transition of silicate phases, and consequently controls the phase equilibrium (Arnason et al., 1993). By contrast, this correlation is contradictory with the results of epidote analyses from the Salton Sea geothermal system by Bird et al. (1988). Based on their observations, the authors established that epidote becomes more aluminous with increasing depth and temperature. Both changes in fluid composition and temperature were attributed as the most influential variables causing changes in epidote composition in that case.

Zoning of epidote mineral grains observed, for example by Marks et al. (2010) in the Reykjanes and Nesjavellir geothermal systems in Iceland is also confirmed in the present study (e.g. Figure 32). The explanation for compositional zoning patterns in epidote is an intriguing problem. This is not surprising considering the sensitivity of Fe and Al contents of epidote to slight changes in a variety of intensive

and extensive thermodynamic variables during hydrothermal activity. Zoning also depends directly on the initial ratio of the activities of Fe^{3+} and Al^{3+} in the aqueous solution. In well OW-910, intragrain compositional zoning seems to be dependent directly on local changes in fluid transport properties and intensive thermodynamic variables (e.g. CO_2 concentrations in fluid phase, pH, bulk rock composition and fO_2) during the thermal evolution of the geothermal system. Such changes result in the formation of several spatially related phases which are not in chemical equilibrium. In this respect, it is reasonable to assume that intrusion activity (e.g. basaltic and micro-granite) observed in this well caused a surge in CO_2 concentrations in the thermal fluids. This in turn caused a change in the fluid composition by lowering the pH of the fluids, consequently affecting aqueous speciation of Al^{3+} and Fe^{3+} complexes. While this is important in many cases, compositional zoning patterns in some epidote mineral grains are caused by non-equilibrium, irreversible processes (Arnason and Bird, 1992). In this case, the relative rates of Al^{3+} and Fe^{3+} mass transfer accompanying the irreversible dissolution of common rock forming minerals control epidote compositional zoning.

5.8.2 Chlorite

Measured chemical compositions of different epidote crystals, derived from two different depth intervals in well OW-910, show wide and concomitant variations in Al and Fe contents. Variations in the Fe^{3+}-Al^{3+} contents of epidote observed presumably reflect changes in fluid composition during the formation of the mineral. Epidote composition depends directly on the ratio of the activities of $Fe^{3+}$and Al^{3+} in the fluid. However, aqueous complexation of Fe^{3+} and Al^{3+} with other anions (e.g. $SO_4^{2-}, CO_3^{2-}, Cl^-, OH^-$, etc) may cause the composition of epidote to depend on fCO_2, pH and chloride concentration in the fluid phase (Arnason et al., 1993). Thus, changes in fluid composition during the evolution of epidote may result in variations in $Fe^{3+}$and Al^{3+} exchange without necessarily reflecting changes in temperature or pressure.

Other plausible thermodynamic mechanisms to account for the variation in epidote composition in well OW-910 are changes in fO_2 and the oxidation state. Diverse experimental results (e.g. Arnason et al., 1993) have demonstrated that fO_2 strongly controls the Fe-content of epidote. Values for fO_2 for the Olkaria geothermal system have not been determined, but such studies would be of great interest. According to the authors, epidote is the most Fe-rich in the presence of haematite-magnetite oxygen buffer and becomes more aluminous with decreasing fO_2, as the proportion of ferric iron in the system decreases. In addition, the authors noted that epidote stability increases with increasing fO_2. The latter expands the P-T boundaries of the epidote stability field. Like in the Salton Sea geothermal system, epidote in well OW-910 is known from binocular observation and optical petrography of cuttings to occur alongside haematite. This observation is closely compatible with the relatively high fO_2 calculated for the Salton Sea geothermal system (Bird and Spieler, 2004). Epidote in haematite-bearing assemblages is traditionally known to be more Fe-rich (Bird et al., 1988).

Additionally, results of epidote analysis at 1236 m depth display a positive relationship between the relatively high Fe-content of epidote and inferred level of oxidation. This is marked by concomitant increase in the oxidation state of host rocks from 864 m to 1236 m depth. The enrichment of Sr and Ti in the rim and core of epidote, respectively suggest that epidote could be an important repository for these elements, mobilized through hydrothermal alteration. Results of previous analyses of Icelandic epidotes, for example in the Hengill geothermal system (e.g. Bragason, 2012), points to a more or less similar picture where, Sr contents are noted to increase progressively towards the rims. Based on the authors' interpretation, increase in Sr contents very likely reflects extensive breakdown of plagioclase.

Variations of the average mole fraction of pistachite (Xps) contents of epidote in this well is satisfactorily correlated with depth, and is in agreement with the range in some well known geothermal systems of the world (e.g. Bird and Spieler, 2004, Bird et al., 1988). Marks et al. (2010), while studying epidote in the Reykjanes and Nesjavellir high-temperature geothermal systems in Iceland observed an increase in the average molar ratio of pistachite with depth. The authors interpreted this observation to indicate an increase in temperature. In the Olkaria geothermal system, well OW-910 is a high-temperature well with regard to measured down-hole formation temperatures, reaching a maximum of about 300°C (Musonye, 2015). The distribution of formation temperature in this well, therefore, is

consistent with the relationship between the molar ratio of pistachite and temperature advocated by Marks et al. (2010). Temperature exerts a major influence on the transition of silicate phases, and consequently controls the phase equilibrium (Arnason et al., 1993). By contrast, this correlation is contradictory with the results of epidote analyses from the Salton Sea geothermal system by Bird et al. (1988). Based on their observations, the authors established that epidote becomes more aluminous with increasing depth and temperature. Both changes in fluid composition and temperature were attributed as the most influential variables causing changes in epidote composition in that case.

Zoning of epidote mineral grains observed, for example by Marks et al. (2010) in the Reykjanes and Nesjavellir geothermal systems in Iceland is also confirmed in the present study (e.g. Figure 32). The explanation for compositional zoning patterns in epidote is an intriguing problem. This is not surprising considering the sensitivity of Fe and Al contents of epidote to slight changes in a variety of intensive and extensive thermodynamic variables during hydrothermal activity. Zoning also depends directly on the initial ratio of the activities of Fe^{3+} and Al^{3+} in the aqueous solution. In well OW-910, intragrain compositional zoning seems to be dependent directly on local changes in fluid transport properties and intensive thermodynamic variables (e.g. CO_2 concentrations in fluid phase, pH, bulk rock composition and fO_2) during the thermal evolution of the geothermal system. Such changes result in the formation of several spatially related phases which are not in chemical equilibrium. In this respect, it is reasonable to assume that intrusion activity (e.g. basaltic and micro-granite) observed in this well caused a surge in CO_2 concentrations in the thermal fluids. This in turn caused a change in the fluid composition by lowering the pH of the fluids, consequently affecting aqueous speciation of Al^{3+} and Fe^{3+} complexes. While this is important in many cases, compositional zoning patterns in some epidote mineral grains are caused by non-equilibrium, irreversible processes (Arnason and Bird, 1992). In this case, the relative rates of Al^{3+} and Fe^{3+} mass transfer accompanying the irreversible dissolution of common rock forming minerals control epidote compositional zoning.

6. CONCLUSION AND RECOMMENDATIONS

6.1 Conclusion

The lithological units encountered in well OW-922 are consistent with the general sub-surface stratigraphy of the Olkaria Volcanic Complex. Total absence of intrusive rocks and a marked reduction in rhyolitic volcanism is, however, observed in this well. The two aspects point towards the location of the well, being outside the main Olkaria volcanic zone.

Generally, the well is dominated by low-temperature alteration minerals, which are observed extending to greater depths. Abundant calcite deposition is apparent, especially towards the bottom of the well, and the mineral is observed overprinting epidote.

Five small feed zones have been recognized in the well. They are connected to lithological contacts, variations in alteration patterns, circulation losses, prevalence of calcite deposition, intense pyritization, changes in ROP and kinks in temperature recovery logs.

Intense calcite deposition, failure of the well to accept water during injection test and the absence of clear pivot point are indications that permeability in the well is very limited.

Hydrothermal alteration mineralogy shows that the area has had temperatures $\geq 240^{o}$C in the past, as indicated by the presence of epidote. However, measured formation temperature reached a maximum of 127^{o}C after 49-days recovery period. Consequently, the difference in measured formation and inferred alteration temperatures distinctly demonstrates that the geothermal system around the well has significantly cooled over time. Calcite overprinting epidote further argues in favour of this conclusion.

From petrochemical analysis, the rocks show a complete range of compositions from basalt to trachyte or rhyolite. Highly evolved rocks are predominant.

Based on major oxides and trace elements systematics, fractional crystallisation is the dominant magma differentiation mechanism for evolution of the rocks of the study well. Other magma modification mechanisms likely played some role, but only to a limited extent.

Significant changes in the abundance of major oxides and trace elements have not taken place during hydrothermal alteration processes. Equally, a comparison of surface and sub-surface samples indicates the possibility of a petrogenetic connection caused by a common differentiation process. The samples are, therefore, geochemically comparable.

The compositional variations of epidote from two different depth intervals in well OW-910 appear to be strongly influenced by the combined effects of temperature, fO_2 and fluid composition. Results of similar studies from other geothermal systems corroborates this fact.

The presence of zonation in epidote mineral grains indicates that fluid composition and pressure or temperature conditions in the geothermal system have changed with time.

Due to limited number of epidote and chlorite samples, it was not possible to carry out a stratigraphic correlation in the four wells based on major and minor element contents.

6.2 Recommendations

Additional temperature and pressure profiles need to be measured. As the well has been shut-in for a period of over one and a half years, current temperature and pressure measurements will provide a true reflection of the state of the system, as opposed to the 49-days recovery profile used in this study.

Fluid inclusion studies need to be carried out and integrated with the inferred alteration and measured (or calculated) formation temperatures. Several attempts were made to conduct fluid inclusion analysis for the well but were unsuccessful due to problems with sample preparation. The findings would serve as a better means of reconstructing the past history of the geothermal system around well OW-922.

In-depth geological and geophysical studies of the area east of Domes field is still strongly recommended if expansion of production drilling has to continue in the area. Some geophysical studies have already been carried in the area but the findings are limited in my view. The combination and comparison of the findings with other disciplines (i.e. geochemistry) will be crucial in better understanding the system east of the Domes.

Well OW-922 should be listed amongst the reservoir monitoring wells in Olkaria. In particular, monitoring of the drawdown changes in this well will be vital in establishing whether or not there exists a connection between system around the well and the Olkaria reservoir.

There is need to carry out radiogenic isotope studies (Pb-Sr-Nd-Hf) to gain valuable information about the source of the rocks from the four wells, that is whether the rocks are derived from similar or different parental magmas. In addition, radiogenic isotopes will provide useful insights about crustal contamination during ascent of the magma.

REFERENCES

Achauer, U., and Masson, F., 2002: Seismic tomography of continental rifts revisited: from relative to absolute heterogeneities. *Tectonophysics, 358*, 17-37.

Allen, D.J., Darling, W.G., and Burgess, W.G., 1989: *Geothermics and hydrogeology of the southern part of the Kenya Rift Valley with emphasis on the Magadi-Nakuru area.* British Geological Survey, report SD/89/1, 68 pp.

Ambusso, W.J., and Ouma, P.A., 1991: Thermodynamic and permeability structure of Olkaria Northeast field: Olkaria fault. *Geothermal Resource Council, Transactions, 15*, 237-242.

Arnason, J.G., and Bird, D.K., 1992: Formation of zoned epidote in hydrothermal systems. *Water-Rock Interaction, Stanford University, USA*, 1473-1476.

Arnason, J.G., Liou, J. G., and Bird, D.K., 1993: Variables controlling epidote composition in hydrothermal and low-pressure regional metamorphic rocks. *Proceedings of the Abhand Geol. Bund., Salzburg, Austria, 49*, 17–25.

Baker, B.H., Mohr, P.A., and Williams, L. A. J., 1972: Geology of the Eastern Rift System of Africa. *Contrib. GSA Special Papers, 136*, 1-68.

Baker, B.H. and Wohlenberg, J., 1971: Structural evolution of the Kenya Rift Valley. *Nature, 229,* 538-542.

Bird, D.K., Cho, M., Janik, C.J., Liou, J.G., and Caruso, L.J., 1988: Compositional, order/disorder, and stable isotope characteristics of Al-Fe epidote, State 2-14 Drill hole, Salton Sea geothermal system. *J. of Geophysics. Res., 93,* 13135-13144.

Bird, D.K., and Spieler, A.R., 2004: Epidote in geothermal systems. *Reviews in Mineralogy and Geochemistry, 56*, 235-300.

Bosworth, W., 1987: Axis volcanism in the Gregory Rift, East Africa: implications for models of continental rifting. *Geology, 15,* 397-400.

Bliss, C.M., 1979: *Geology and petrochemistry of the Naivasha area, Kenya RiftValley*. Lancaster University, Ph.D. thesis (unpublished), 270 pp.

Bragason, G,O., 2012: *Strontium isotope shift in clay minerals, epidote and geothermal fluid in the Hellisheidi geothermal field, SW-Iceland*. University of Iceland, MSc. thesis, 45 pp.

Browne, P.R.L., 1978: Hydrothermal alteration in active geothermal fields. *Annual Review Earth and Planetary Sciences, 6,* 229–250.

Browne, P.R.L., 1984: *Lectures on geothermal geology and petrology*. UNU-GTP, Iceland, report 2, 92 pp.

Bryndzia, L.T., and Scott, S.D., 1987: The composition of chlorite as a function of sulfur and oxygen fugacity. An experimental study. *Am. J. Sci., 287*, 50-76.

Chorowicz, J., 2005: The East African Rift System. *J. African Earth Sciences, 43*, 379-410.

Clarke, M.C.G., Woodhall, D.G., Allen, D., Darling, G., 1990: *Geological, volcanological and hydrogeological controls of the occurrence of geothermal activity in the area surrounding Lake Naivasha, Kenya.* Min. of Energy, Nairobi, report 150, 138 pp.

Davies, G.R., and Macdonald, R., 1987: Crustal influences in the petrogenesis of the Naivasha basalt-comendite complex, combined trace elements and Sr-Pb isotope constraints. *J.Petrology, 28,*1009-1031.

Dubois, M., and Martinez-Serrano, R.G., 1998: Chemical variations in chlorite at the Los Humeros geothermal system, Mexico. *Clay and Clay Minerals, 46-6,* 615-628.

Ebinger, C., 2005: Continental breakup: The East African perspective. *Astronomy and Geophysics, 46*, 216–221.

Ebinger, C., and Sleep, N.H., 1998: Cenozoic magmatism in central and east Africa resulting from impact of one large plume. *Nature, 395*, 788–791.

Franzson, H., Zierenberg, R. and Schiffman, P., 2008: Chemical transport in geothermal systems in Iceland, evidence from hydrothermal alteration. *J. Volcanology & Geothermal Research, 173*, 217-229.

Hardarson, B.S., 1993: *Alkalic rocks in Iceland with special reference to the Snaefellsjökull volcanic system*. University of Edinburgh, Ph.D. thesis (unpublished), 330 pp.

Heumann, A., Davies, G.R., 2002: U-Th disequilibrium and Rb-Sr age constraints on the magmatic evolution of peralkaline rhyolites from Kenya. *J. Petrology, 43,* 557-577.

KenGen 2012: *Stratigraphy and hydrothermal alteration mineralogy of well OW-915B*. KenGen internal report (unpublished), 40 pp.

KenGen 2014: *Well completion report for well OW-922*. KenGen in-house report (unpublished), 32 pp.

Kristmannsdóttir, H., 1979: Alteration of basaltic rocks by hydrothermal activity at 100-300°C. In: Mortland, M.M., and Farmer, V.C. (editors), *International Clay Conference 1978*. Elsevier Scientific Publishing Co., Amsterdam, 359-367.

Lagat, J.K., 2004: *Geology, hydrothermal alteration and fluid inclusion studies of the Olkaria Domes geothermal field, Kenya*. University of Iceland, MSc. thesis, UNU-GTP, Iceland, report 2, 71 pp.

Laird, D.A., 2006: Influence of layer charge on swelling of smectites. *Applied Clay Science, 34*, 74-87.

Le Bas, M.J., Le Maitre, R.W., Streckeisen, A., and Zanettin, B., 1986: A chemical classification of volcanic rocks based on the total alkali-silica diagram. *J. Petrology, 27-3*, 745-750.

Lonker, S.W., Franzson, H., & Kristmannsdóttir, H., 1993: Mineral-fluid interactions in the Reykjanes and Svartsengi geothermal systems, Iceland. *Am. J. of Science, 293-7*, 605-670.

Macdonald, R., 1974: Nomenclature and petrochemistry of the peralkaline oversaturated extrusive rocks. *Bull. Volcanology*, *38*, 498–516.

Macdonald, R., Black, H.E., Fitton, J.G., Marshall, A.S., Nejbert, K., Rodgers, N.W., and Tindle, A.G., 2008: The roles of fractional crystallisation, magma mixing, crystal mush remobilization and volatile-melt interactions in the genesis of a young basalt-peralkaline rhyolite suite, the Greater Olkaria volcanic complex, Kenya Rift Valley. *J. Petrology, 49-8*, 1515-1547.

Macdonald, R., Rogers, N. W., Fitton, J. G., Black, S., and Smith, M., 2001: Plume-lithosphere interactions in the generation of basalts of the Kenya Rift, East Africa. *J. Petrology, 42,* 877-900.

Macdonald, R., and Scaillet, B., 2006: The central Kenya peralkaline province: Insights into the evolution of peralkaline salic magmas. *J. Petrology, 47*, 59-73.

Mannvit/ÍSOR/Vatnaskil/Verkís Consortium, 2011: *Consultancy services for geothermal optimization study of the Greater Olkaria geothermal fields. Report 3: Revision of the conceptual model of the Greater Olkaria Geothermal System – Phase I.* Mannvit/ÍSOR/ Vatnaskil/Verkís, Reykjavík, 100 pp.

Marks, N., Schiffman, P., Zierenberg, R.A., Franzson, H., and Fridleifsson, G.Ó., 2010: Hydrothermal alteration in the Reykjanes geothermal system: Insights from Iceland deep drilling program well RN-17. *J. Volcanology & Geothermal Research, 189*, 172–190.

Marshall, A.S., Macdonald, R., Rogers, N.W., Fitton, J.G., Tindle, A.G., Nejbert, K., and Hinton, R.W., 2009: Fractionation of peralkaline silicic magmas: The Greater Olkaria volcanic complex, Kenya Rift Valley. *J. Petrology, 50,* 323-359.

Mielke, P., Nehler, M., Bignall, G., and Sass I., 2015: Thermo-physical rock properties and the impact of advancing hydrothermal alteration – A case study from the Tauhura geothermal field, New Zealand. *J. Volcanology and Geothermal Research, 301,* 14-28.

Moore, M.D. and Reynolds, R.C. Jr., 1997: X-ray diffraction and the identification and analysis of clay minerals (18th ed.). Oxford University Press, NY, 378 pp.

Mortensen, A.K., Egilson, Th., Gautason, B., Árnadóttir S., and Gudmundsson A., 2014: Stratigraphy, alteration mineralogy, permeability and temperature conditions of well IDDP-1, Krafla, NE-Iceland. *Geothermics, 49*, 31-41.

Mungania, J., 1999: *Geological report of well OW-714*. Kenya Power Company internal report.

Musonye, X.S., 2015: *Sub-surface petrochemistry, stratigraphy and hydrothermal alteration of the Domes area, Olkaria geothermal field, Kenya*. University of Iceland, MSc. thesis, UNU-GTP, Iceland, report 3, 108 pp.

Mwangi, D.W., 2012: Borehole geology and hydrothermal mineralisation of well OW-916, Olkaria Domes geothermal field, Naivasha, Kenya. Report 24 in: *Geothermal training in Iceland 2012*. UNU-GTP, Iceland, 541-571.

Mwania, M.M., Munyiri, S., and Okech, E., 2013: *Borehole geology and hydrothermal mineralisation of well OW-35, Olkaria East geothermal field, Kenya*. UNU-GTP, Iceland, report 1, 56 pp.

Nkapiani, M.N., 2014: Application of stable isotope geochemistry to tracing recharge and flow systems of fluids in the Olkaria geothermal field, Kenya. Report 24 in: *Geothermal training in Iceland 2014*. UNU-GTP, Iceland, 483-504.

Nyblade, A.A., and Robinson, S.W., 1994: The African superswell. *Geophys. Res. Letters, 21,* 765–768.

Ofwona, C., Omenda, P., Mariita, N., Wambugu, J., Mwawongo, G., and Kubo, B., 2006: *Surface geothermal exploration of Korosi and Chepchuk prospects.* KenGen, Kenya, internal report, 44 pp.

Ojiambo, B.S., and Lyons, W.B., 1993: Stable isotope composition of Olkaria geothermal field fluids, Kenya. *Geothermal Resource Council, Transactions 17,* 149-145.

Okoo, J.A., 2013: Borehole geology and hydrothermal mineralisation of well OW–39A, Olkaria East geothermal field, Naivasha, Kenya. Report 24 in: *Geothermal training in Iceland 2013*. UNU-GTP, Iceland, 547-574.

Omenda, P.A., 1997: The geochemical evolution of Quaternary volcanism in the south-central portion of the Kenya Rift. University of Texas, El Paso, Ph.D. thesis, 219 pp.

Omenda, P.A., 1998: The geology and structural controls of the Olkaria geothermal system, Kenya. *Geothermics, 27-1,* 55-74.

Otieno, V., and Kubai, R., 2013: Borehole geology and hydrothermal mineralisation of well OW-37A, Olkaria east geothermal field, Kenya. UNU-GTP, Iceland, report 2, 105 pp.

Otieno, V., Okoo, J., Munyiri., S., Wanjohi, D., and Wanjohi A., 2014: *Structural mapping of Olkaria South West field, Olkaria geothermal project*. KenGen, Kenya, internal report, 41 pp.

Pirajno, F., 1992: *Hydrothermal mineral deposits*. John Wiley and Sons, Sydney, 709 pp.

Peccerillo, A., Donati, C., Santo, A.P., Orlando, A., Yirgu, G., and Ayalew, D., 2007: Petrogenesis of silicic peralkaline rocks in the Ethiopian rift: Geochemical evidence and volcanological implications. *J. African Earth Sciences, 48*, 161-173.

Reyes, A.G., 2000: *Lectures on petrology and mineral alteration in hydrothermal systems: From diagenesis to volcanic catastrophes.* UNU-GTP, Iceland, report 18-1998, 77 pp.

Ring, U., 2014: The East African Rift System: *Austrian J. Earth Sciences, 107-1,* 132-146.

Rollinson, H.R., 1995: *Using geochemical data: Evaluation, presentation, interpretation*. Longman Group Ltd., England.

Ronga, F., Lustrini, M., Marzoli, A., and Melluso, L., 2009: Petrogenesis of a basalt-comendite-pantellerite rock suite: The Boseti volcanic complex (Main Ethiopian Rift). *Miner Petrol, 98,* 227-243.

Ronoh, I.J., 2012: *Borehole geology and hydrothermal mineralisation of well OW-912B, Olkaria geothermal field, Kenya.* Report 29 in: *Geothermal training in Iceland 2012*. UNU-GTP, Iceland, 695-732.

Schiffman, P., and Roeske, S., 2014: Electron microprobe analysis of minerals, University of California, 293-306.

Shackleton, R.M., 1996: The final collision between East and West Gondwana: where is it? *J. African Earth Sciences, 23*, 271-287.

Simiyu, S.M., 2010: Status of geothermal exploration in Kenya and future plans for its development. *Proceedings of the World Geothermal Congress, Bali Indonesia,* 11 pp.

Simiyu, S.M., and Keller, G.R., 2000: Seismic monitoring of the Olkaria Geothermal area, Kenya Rift valley. *J. Volcanology and Geothermal Research, 95,* 197-208.

Simmons, S.F., and Christenson, B. W., 1994: Origins of calcite in boiling geothermal systems. *Am. J. of Science, 294,* 361-400.

Smith, M., Mosley, P., 1993: Crustal heterogeneity and basement influence on the development of the Kenya Rift, East Africa. *Tectonics 12-2,* 591–606.

Steiner, A., 1968: Clay minerals in hydrothermally altered rocks at Wairakei, New Zealand. *Clay and clay minerals, 16*, 193-213.

Steiner, A., 1977: The Wairakei geothermal area, North Island, New Zealand: its sub-surface geology and hydrothermal rock alteration. *NZ Geol. Surv., Bull., 90*, 127 pp.

Verma, S.P., Torres-Alvarado, I.S., Pandarinath, K., and Dulski, P., 2008: Element mobility during the hydrothermal alteration of rhyolitic rocks of the Los Azufres geothermal field (Mexico). *Geothermics, 37*, 53-72.

Verma, S.P., Torres-Alvarado, I.S., Satir, M., and Dobson, P. F., 2005: Hydrothermal alteration effects in geochemistry and Sr, Nd, Pb and O isotopes of magmas from the Los Azufres geothermal field (Mexico): A statistical approach. *Geochemical J., 39,* 141-163.

Weaver, B. D., Sceal, J.S.C and Gibson, I. L., 1972: Trace element data relevant to the origin of trachytic and pantelleritic lavas in the East African Rift System. *Contrib. Mineral. Petrol. 36,* 181-194.

Williams, L.A.J., 1970: The volcanics of the Gregory Rift Valley, East Africa. *Bull. Volcanology, 34*, 439-465.

Wilson, M., 1989: *Igneous petrogenesis, A global tectonic approach*. University of Leeds, Department of Earth Sciences, 466 pp.

Wise, W.S., 2005: Zeolites. *University of California, Santa Barbara, CA. Elsevier Ltd.,* 591-600.

Yoshio, W., Eiichiro, M., and Kozo, S., 2011: *X-ray diffraction crystallography*. Springer, NY, Heidelberg Dordrecht, 67-80.

APPENDIX A: Lithological description of well OW-922 based on binocular and optical petrographic analyses

0-46 m Pyroclastics: Light grey, unconsolidated heterogeneous drill chips composed predominantly of tuffaceous, pumiceous, obsidian, volcanic glass as well as obsidian. It is moderately oxidized and no hydrothermal alteration is observed in this section. Alteration minerals: oxides.

46-58 m: No samples (Loss of circulation returns).

58-96 m Pyroclastics: Light grey, considerably unconsolidated heterogeneous drill cuttings composed of tuffaceous, pumiceous, volcanic glass as well as obsidian. It is moderately oxidized and no hydrothermal alteration is observed in this section. Alteration minerals: oxides.

96-190 m: *No samples (Loss of circulation returns).*

190-302 m Pyroclastics: Light grey to yellowish-brown, unconsolidated heterogeneous drill chips composed predominantly of tuffaceous, pumiceous, volcanic glass as well as obsidian. It is mildly oxidized. Alteration minerals: oxides, calcite.

302-350 m Tuffs (lithic): Brown to light grey, cryptocrystalline tuffaceous rock. It is highly vesicular, vesicles are primarily infilled with zeolites (scolecite and mesolite) and rarely calcite. Patches of fine grained green clays are also noted infilling vesicles. The rock is weakly altered with minor pyrite disseminations in the matrix. Alteration minerals: clays, calcite, zeolites.

350-362 m: *No samples (Loss of circulation returns).*

362-364 m Tuffs: Brown to light grey, cryptocrystalline tuffaceous rock. It is highly vesicular, vesicles are primarily infilled with zeolites (scolecite and mesolite) and rarely calcite. The rock is weakly altered with minor pyrite disseminations in the matrix. Alteration minerals: clays, calcite, zeolites, pyrite.

364-408 m Trachyte: Grey, fine grained crystalline rock. It is phyric with sanidine and quartz porphyries. Numerous specs of opaque minerals (olivine and pyroxenes) are noted as well in the rock matrix. It depicts flow banding texture and slight intensity of alteration. Minor pyrite is disseminated in the rock matrix. Alteration minerals: clays, zeolites, pyrite.

408-422 m Tuffs (lithic): Brown, highly vesicular tuffaceous rock. Vesicles are infilled with chalcedony (412-414 m) and zeolites (scolecite and mesolite). The rock is weakly altered with minor pyrite disseminations in the matrix. Alteration minerals: clays, calcite, chalcedony, zeolites, pyrite.

422-476 m Trachyte: Grey, fine grained phyric rock with sanidine and quartz porphyries. Specs of mafic minerals (olivine and pyroxenes) are noted in the rock matrix. It is slightly vesicular, vesicles are infilled with calcite and chalcedony. Veinlet infilled with chalcedony noted between 446 and 448 m. Minor pyrite is disseminated in the rock matrix. Alteration minerals: clays, calcite, titanite, chalcedony, pyrite.

476-498 m Tuff (lithic): Light grey to light brown, highly vesicular tuffaceous rock intermixed with minor trachytic fragments. The latter are suspected to have fallen from the unit above. Distinct vesicles infilled with secondary quartz (e.g. 476-478 m), zeolites (e.g. 480-482 m) and calcite are observed. Furthermore, wairakite is noted in a vesicle between 494 and 496 m. The rock is weakly altered with minor pyrite disseminations in the matrix. Alteration minerals: clays, calcite, secondary quartz, wairakite, pyrite.

498-504 m Basalt: Dark grey, fine grained, slightly vesicular rock. Tuffaceous fragments (suspected to have fallen from above) are notable in minor quantities. Quartz veins are present between 500 and 502 m. It is slightly altered. Alteration minerals: clays, calcite, secondary quartz.

504-564 m Trachyte: Grey, mixed cuttings of trachyte (most abundant), tuffaceous and basaltic fragments. It is veined and vesicular. Quartz vein noted between 516 and 518 m while vesicles infilled with calcite are observed between 520 and 522 m. Alteration minerals: clays, secondary quartz, calcite.

564-582 m Tuff (lithic): Mostly brown, whitish to brownish cryptocrystalline tuffaceous fragments. It is mixed with pumiceous, trachytic and rhyolitic fragments and moderately vesicular rock. Majority of the vesicles are empty, whereas, a few are infilled with zeolites and secondary quartz. Pyrite is embedded as well as disseminated in the rock matrix. Minor patches of green clays are noted replacing the matrix of individual fragments. Alteration minerals: clays, calcite, pyrite, quartz, wairakite (574-578 m).

582-726 m Trachyte: Light grey, fine grained moderately porphyritic rock with feldspar and quartz porphyries. Veinlets infilled with mafic minerals are discernible. Green clays are observed replacing the mafic silicates. It is mildly oxidized and appears relatively fresh. Partial loss between 596 and 604 m, and 636-638 m. Alteration minerals: clays, titanite.

726-744 m Tuff (lithic): Pale brown fine grained tuffaceous rock (dominant) mixed with trachytic fragments. Occasional quartz phenocrysts are observed on both fragments. It is moderately to highly oxidized but displays minimal intensity of alteration. Calcite is observed infilling the vesicles. Alteration minerals: clays, calcite.

744-822 m Trachyte: Brown to dark grey, fine grained to cryptocrystalline rock. It is slightly porphyritic with euhedral sanidine phenocrysts, some elongated in form. Mafic minerals are outstanding in the matrix and show alteration to green clays. Albite noted replacing the sanidine phenocrysts at 802-814 m and 816-818 m. It is mixed with minor tuffaceous fragments. The formation shows minimal intensity of alteration. Alteration minerals: clays, calcite, chalcedony, albite.

822-890 m Trachyte: Holocrystalline, grey to dark grey, fine grained rock depicting flow banding texture (between 862 and 864 m). It is slightly porphyritic with subhedral to euhedral phenocrysts of sanidine. Generally, the formation is massive, though vesicular between 870 and 872 m, with green clays infilling the vesicles. Green clays are also observed extensively replacing the mafic silicates. Albite is observed replacing sanidine phenocryst between 842 and 844 m. The formation is slightly oxidized and exhibit slight degree of alteration. Alteration minerals: clays, calcite, chalcedony, albite.

890-918 m Trachyte: Light grey to grey, fine grained poorly phyric rock with elongated subhedral sanidine phenocrysts. It is relatively massive and holocrystalline. The rock is slightly altered but shows high intensity of alteration between 904 and 910 m. Tuffaceous fragments observed between 910 and 912 m (inferred to have fallen from above). Alteration minerals: clays, calcite.

918-952 m Trachyte: Light grey, aphanitic rock. It is moderately feldspar phyric with the dominant phenocryst phase being sanidine. Some phenocrysts are elongated and euhedral. It is slightly altered. It is both slightly oxidized and altered. Alteration minerals: clays, calcite, pyrite, albite.

952-966 m Tuff (lithic): Brown (952-962 m) to grey (962-966 m), fine grained tuffaceous rock. It is highly vesicular between 962 and 966 m, vesicles are empty. It is moderately altered to clays between 952 and 962 m and shows slight alteration for the remaining part. Alteration minerals: clays, calcite, pyrite.

966-1046 m Trachyte: Grey, fine grained highly vesicular rock. It is moderately porphyritic with subhedral sanidine phenocrysts. Most vesicles are empty and others partially infilled with calcite. In addition, specs of mafic minerals are present, some being replaced by brown and green clays. The formation is slightly altered but alteration intensity increases towards the bottom (1024-1042 m). Partial loss between 1042 and 1046 m. Pyrite disseminated in the rock matrix. Alteration minerals clays, pyrite, calcite, chalcedony (990-992 m).

1046-1150 m Rhyolite: Light grey to pink, fine grained massive and crystalline rock. It is moderately porphyritic with quartz phenocrysts. Several specs of mafic minerals are noted disseminated in the rock

matrix. Some mafics are partially replaced by clays. The formation is highly oxidized between 1054 and 1056 m and relatively fresh. Alteration minerals: clays, pyrite.

1150-1198 m Basalt: Mostly brown, fine grained, mixed cuttings composed primarily of basaltic fragments. It is slightly porphyritic with plagioclase phenocrysts. Majority of the phenocrysts have been replaced by clays whereas others are noted being replaced by calcite. Mineral sequence noted between 1188 and 1190 m with chalcedony on the rim and calcite precipitated on the core. Vesicles infilled with calcite are plentiful. Pyrite is disseminated in the rock matrix. The formation is highly altered. Partial loss between 1152 and 1154 m, and 1190 and 1192 m. Alteration minerals: clays, pyrite, calcite, haematite (1192-1198 m).

1198-1214 m Basalt: Dark grey, fine grained to cryptocrystalline rock. It is poorly porphyritic with indistinct plagioclase phenocrysts. Depicts slight intensity of alteration with minor pyrite disseminations in the rock matrix. Alteration minerals: clays, pyrite, calcite, haematite (1198-1200 m).

1214-1224 m Rhyolite: Light grey, fine grained highly felsic massive rock mixed with cryptocrystalline basaltic fragments. It is phyric with quartz phenocrysts. Fresh specs of mafic minerals are observed in the matrix. The formation is mostly fresh though slight alteration to green and brown clays is evident. It is mildly oxidized as well. Alteration minerals: clays.

1224-1260 m Trachyte: Light grey to pale green, fine grained holocrystalline rock but mostly grey between 1234 and 1244 m. It is slightly porphyritic with sanidine phenocrysts. Minor tuffaceous fragments noted between 1248 and 1260 m. The rock is slightly altered and moderately oxidized between 1258 and 1260 m. Alteration minerals: titanite, clays, pyrite.

1260-1312 m Tuff (vitric): Mostly whitish, fine grained tuffaceous rock. It is highly vesicular especially between 1294 and 1298 m, vesicles are infilled with calcite and green clays. Pyrite dissemination (including euhedral cubes) is rather intense. This is a probable feed zone. Alteration minerals: clays, calcite, pyrite.

1312-1440 m Trachyte: Light grey, to grey to pale green, fine grained rock. It is slightly porphyritic with occasional subhedral sanidine phenocrysts. Calcite is noted replacing some phenocrysts. Mafic silicates are being replaced by brown clays. Pyrite is noted infilling veinlets as well as disseminated in the rock matrix. The formation is moderately altered. Alteration minerals: pyrite, clays, titanite, calcite.

1440-1600 m Tuff (lithic): Grey to pale green, fine grained tuffaceous rock mixed with minor trachytic fragments embedded within the lithic fragments. Vesicles infilled with calcite are noted. It is slightly altered and pyrite disseminations are evident on the rock matrix. Partial losses between 1454 and 1458,1462 and 1466, and 1512 and 1518 m. Alteration minerals: pyrite, clays, titanite, calcite.

1600-1642 m Tuff (lithic): Grey, fine grained tuffaceous rock. It is highly vesicular, vesicles are infilled with clays and calcite. Also, veinlets are noted infilled with calcite. It shows incipient alteration with minor pyrite disseminations in the rock matrix. Alteration minerals: pyrite, clays, titanite, calcite.

1642-1654 m Basalt: Dark grey, fine grained crystalline rock. It is slightly porphyritic with plagioclase phenocrysts. Occasionally, vesicles infilled with calcite are present. Also, calcite is observed replacing some plagioclase phenocrysts. It is moderately altered and pyrite is disseminated in the rock matrix. Alteration minerals: pyrite, clays, titanite, calcite.

1654-1700 m Basaltic trachyandesite: Brown, slightly porphyritic crystalline rock with plagioclase phenocrysts. The latter are noted being replaced by clays and calcite. Mafic silicates display total alteration to clays. Platy calcite observed between 1646 and 1648, and 1680 and 1682 m. Pyrite cubes are disseminated in the rock matrix. The formation is highly altered. Alteration minerals: clays, calcite, pyrite, titanite.

1700-1730 m Trachydacite: Grey, fine grained to cryptocrystalline poorly porphyritic rock with minor sanidine phenocrysts. Occasionally vesicles are present infilled with clays and calcite. Epidote colouration is evident on a sanidine phenocryst between 1728 and 1730 m. Pyrite is disseminated in the rock matrix. Partial circulation loss between 1722 and 1730 m. The formation is moderately altered. Alteration minerals: clays, calcite, pyrite, titanite, epidote, quartz.

1730-2052 m Trachyte: Grey to pale brown, fine grained slightly phyric rock with indistinct sanidine phenocrysts. Vesicles infilled with calcite, green clays and secondary quartz are noted. Veinlets infilled with calcite, mafic minerals and brown clays are noted as well. Calcite replacing sanidine phenocryst between 1768 and 1770 m. Platy calcite noted between 1944 and 1946 m. Epidote coloration noted between 1704 and 1706, 1770 and 1774, and 1930 and 1932 m. It is mildly oxidized and depicts moderate intensity of alteration. However, the formation is highly altered (rated at a scale of 2.5) between 1788-1852 m. Minor pyrite disseminated in the matrix. Partial losses at 1794-1796, 1798-1806, 1810-1816, 1820-1824, 1836-1838, 1842-1844, 1926-1930, 1954-1958, 1964-1972, and 2014-2018 m. A possible feed zone is suspected within this zone. Alteration minerals: pyrite, clays, secondary quartz, titanite, calcite, chalcedony (2008-2010 m), epidote.

2052-2070 m Trachyte: Grey, fine grained to cryptocrystalline rock with minor sanidine phenocrysts. It is relatively dense with specs of mafic minerals conspicuous in the matrix, some showing alteration to brown clays. Trace amounts of pyrite are disseminated in the matrix. It is slightly altered. Alteration minerals: clays, calcite, pyrite.

2070-2186 m Trachyte: Grey to pale brown, fine grained slightly phyric rock with indistinct sanidine phenocrysts. It is highly vesicular. Vesicles infilled with calcite and green clays are noted. Veinlets are noted as well, infilled with calcite, mafic minerals and brown clays. Chalcedony observed recrystallizing to secondary quartz between 2114 and 2116 m. It is mildly oxidized and depicts moderate intensity of alteration. Partial loss at 2070-2076, 2104-2114, 2128-2130, 2142-2150, 2158-2162, 2170-2172, and 2184-2186 m. A possible feed zone within this zone. Alteration minerals: pyrite, clays, titanite, calcite.

2186-2210 m Trachydacite: Pale grey to pink, fine grained aphyric rock mixed with grey trachytic fragments. The rock is rather massive and depicts slight intensity of alteration. Minor pyrite is embedded in the rock matrix. Partial loss between 2186 and 2192, and 2206 and 2210 m. Alteration minerals: clays, calcite, pyrite.

2210-2326 m Trachyte: Mostly grey though showing distinctive gradation to brown between 2256 and 2260, and 2302 and 2306 m. It is sparsely porphyritic with occasional sanidine phenocrysts. Minor basaltic and tuffaceous fragments are noted. Vesicles and veinlets infilled with brown clays are noted. Minor pyrite is disseminated in the rock matrix. Calcite deposition is quite intense in this zone (scale 2.5), possibly reflecting a minor feed zone. It is moderately to highly altered. Partial circulation returns experienced at 2214-2216, 2246-2248, 2266-2268, and 2276-2278 m Alteration minerals: clays, haematite, pyrite, calcite, titanite, epidote coloration (2234-2236 m).

2326-2370 m Trachydacite: Pink, highly felsic fine grained slightly porphyritic rock with primarily quartz phenocrysts. Minor basaltic fragments are observed between 2334 and 2342 m. Vesicles are noted infilled with secondary quartz and dark green clays. Veinlets are largely infilled by brown clays and white minerals. The latter also replace the mafic silicates. Euhedral pyrite cubes are disseminated in the matrix. It is moderately altered. Alteration minerals: clays, pyrite, titanite, calcite, quartz.

2370-2592 m Rhyolite: Pale brown, fine grained, poorly porphyritic rock. It shows flow texture and veinlets infilled with pyrite and brown minerals. Minor pyrite is disseminated in the rock matrix. Generally, the formation is moderately to highly altered but shows slight to moderate intensity of alteration from 2448 m to 2474 m. Partial loss of returns between 2374-2380 m, 2388-2390 m, and 2398-2412 m. Alteration minerals: clays, pyrite, calcite, haematite, chalcedony, epidote coloration (2570-2580 m).

2592-2780 m Trachydacite: Light grey to grey, fine grained slightly porphyritic rock with subhedral to euhedral elongated sanidine phenocryst. It is moderately to strongly porphyritic with striated sanidine phenocrysts between 2598 and 2610, and 2618 and 2632 m. It is slightly vesicular. Vesicles are infilled with brown clays and calcite. Pyrite is disseminated in the rock matrix. The formation is moderately altered. Alteration minerals: clays, calcite, pyrite, haematite,

2780-2784 m Trachyandesite: Grey to dark grey, fine grained poorly porphyritic rock with minor feldspar phenocrysts. It is relatively dense with numerous specs of mafic minerals noted in the rock matrix. Epidote noted replacing feldspar phenocrysts (plagioclase) between 2782 and 2784 m. Paragenetic sequence, with epidote occurring in the core and calcite occurring in the rim is also noted between the same depth interval. Minor pyrite disseminated in the matrix. It shows slight degree of alteration. Alteration minerals: clays, calcite, pyrite, quartz, epidote.

2784-2990 m Trachyte: Mostly grey, poorly porphyritic rock (though slightly porphyritic between 2786 and 2794 m) with indistinct sanidine phenocrysts. It is slightly oxidized and both vesicles and veinlets infilled with calcite and quartz are observed. Pyrite disseminations are discernible in the matrix. Partial losses between 2816 and 2820 m. It is slightly altered. Alteration minerals: clays, pyrite, haematite, titanite, calcite.

APPENDIX B: XRD analysis of clay minerals in well OW-922

Depth (m)	d(001) A	d(001) G	d(001) H	d(002)	Mineral	Type	Other minerals
318-320	No clear peaks	No clear peaks	No clear peaks		No clear peaks	No clear peaks	
338-340	14.11	19.13	9.89		Smectite	Sm.	Feldspars, Amphiboles
358-360	12.48	16.77	9.97		Smectite	Sm.	Feldspars, Amphiboles
380-382	15.36	17.89	10.01		Smectite	Sm.	Feldspars
398-400	13.85	17.27	9.91		Smectite	Sm.	Feldspars, Amphiboles
418-420	No clear peaks	No clear peaks	No clear peaks	No clear peaks	No clear peaks	No clear peaks	
438-440	15.66	18.05	10.11		Smectite	Sm.	Feldspars, Amphiboles
474-476	10.03	10.03	10.03	7.23, HIT=0	Illite + Chlorite (traces)	Chl: ill	Feldspars, Amphiboles
538-540	10.04	10.04	10.04	7.23, HIT=0	Illite + Chlorite (traces)	Chl: ill	Feldspars, Amphiboles
558-560	No clear peaks	No clear peaks	No clear peaks	No clear peaks	No clear peaks	No clear peaks	
738-740	9.96	9.96	9.96		Illite (traces)	ill	Feldspars, Amphiboles
758-760	10.03	10.03	10.03		Illite (traces)	ill	Feldspars, Amphiboles
778-780	10.14	10.14	10.14		Illite (traces)	ill	Feldspars, Amphiboles
952-960	No clear peaks	No clear peaks	No clear peaks	No clear peaks	No clear peaks	No clear peaks	
978-980	No clear peaks	No clear peaks	No clear peaks	No clear peaks	No clear peaks	No clear peaks	
998-1000	No clear peaks	No clear peaks	No clear peaks	No clear peaks	No clear peaks	No clear peaks	
1038-1040	15.41, 10.07	17.42, 10.07	10.07	7.18, HIT=0	Smectite+ Illite + Chlorite	Sm:ill: Chl	Feldspars, Amphiboles
1058-1060	13.69, 10.13	17.30, 10.13	10.13	7.31, HIT=0	Smectite + Illite	Sm: ill	Feldspars, Amphiboles
1198-1200	15.13	17.15	10.29	7.26, HIT=0	Smectite + Unst. Chlorite	Sm: Chl	Feldspars
1218-1220	12.92	17.24	9.86	7.07, HIT=0	Smectite + Unst. Chlorite	Sm: Chl	Feldspars
1340-1342	12.07	12.07	12.07	7.12, HIT=1	Unst. Chlorite + illite	Chl: ill	Feldspars
1358-1360	12.69, 10.06	17.09, 10.06	10.06	7.09, HIT=0	Smectite+ Illite+Chlorite	Sm:ill:Chl	Feldspars, Amphiboles
1418-1420	12.86, 9.96	17.09, 9.96	9.96	7.13, HIT=0	Smectite+ Illite+Chlorite	Sm:ill:Chl	Feldspars, Amphiboles
1438-1440	15.29, 9.99	17.17, 9.99	9.99	7.09, HIT=1	Smectite+ Illite+Chlorite	Sm:ill:Chl	Feldspars, Amphiboles
1458-1460	15.34, 9.79	17.08, 9.79	9.79	7.08, HIT=2	Smectite+ Illite+Chlorite	Sm:ill:Chl	Feldspars, Amphiboles
1554-1556	9.96	9.96	9.96	7.14, HIT=0	Chlorite + Illite	Chl:ill	Feldspars, Amphiboles

Depth (m)	d(001) A	d(001) G	d(001) H	d(002)	Mineral	Type	Other minerals
1558-1560	15.18, 10.11	17.26, 10.11	10.14	7.11, HIT=0	Smectite+ Illite+Chlorite	Sm:ill:Chl	Feldspars, Amphiboles
1576-1578	12.89, 9.91	17.14, 9.91	9.91	7.06, HIT=1	Smectite+ Illite+Chlorite	Sm:ill:Chl	Feldspars, Amphiboles
1578-1582	13.94, 9.93	16.99, 9.93	9.93	7.05, HIT=0	Smectite+ Illite+Chlorite	Sm:ill:Chl	Feldspars, Amphiboles
1598-1600	12.69, 10.03	17.08, 10.03	10.03	7.04, HIT=0	Smectite+ Illite+Chlorite	Sm:ill:Chl	Feldspars, Amphiboles
1618-1620	13.14, 9.84	16.99, 9.84	9.84	7.07, HIT=0	Smectite+ Illite+Chlorite	Sm:ill:Chl	Feldspars, Amphiboles
1640-1642	15.36	17.17	9.91	7.17, HIT=0	Smectite+ Unst. Chlorite	Sm:Chl.	Feldspars, Amphiboles
1658-1660	14.02, 10.01	17.11, 10.01	10.01	7.09, HIT=0	Smectite+ Illite+Chlorite	Sm:ill:Chl	Feldspars, Amphiboles
1696-1698	14.99, 9.98	16.9, 9.98	9.98	HIT=0	Smectite+Illite	Sm:ill	Feldspars
1698-1700	12.51, 10.19	17.17, 10.19	10.19	7.11, HIT=0	Smectite+ Illite+ Chlorite	Sm:ill:Chl	Feldspars
1716-1718	13.48, 10.07	17.57, 10.07	10.07	7.21, HIT=0	Smectite+ Illite+Chlorite	Sm:ill:Chl	Feldspars
1718-1720	13.01, 9.89	16.99, 9.89	9.89	7.16, HIT=0	Smectite+ Illite+Chlorite	Sm:ill:Chl	Feldspars
1738-1740	14.4, 9.98	16.99, 9.98	9.98	7.22, HIT=0	Smectite+ Illite+Chlorite	Sm:ill:Chl	Feldspars
1740-1742	13.5, 9.96	17.26, 9.96	9.96	7.13, HIT=0	Smectite+ Illite+Chlorite	Sm:ill:Chl	Feldspars
1760-1762	14.47, 10.11	17.26, 10.11	10.11	7.19, HIT=0	Smectite+ Illite+Chlorite	Sm:ill:Chl	Feldspars
1778-1780	12.96, 9.99	17.38, 9.99	9.99	7.1, HIT=1	Smectite+ Illite+Chlorite	Sm:ill:Chl	
1780-1782	13.32, 9.96	17.17, 9.96	9.96	7.07, HIT=0	Smectite+ Illite+Chlorite	Sm:ill:Chl	Feldspars
1800-1802	12.84, 9.91	16.54, 9.91	9.91	7.07, HIT=0	Smectite+ Illite+Chlorite	Sm:ill:Chl	Feldspars
1818-1820	12.64, 9.98	17.20, 9.98	9.98	7.09, HIT=0	Smectite+ Illite+Chlorite	Sm:ill:Chl	Feldspars
1838-1840	14.64, 9.89	16.63, 9.89	9.89	7.16, HIT=0	Smectite+ Illite+Chlorite	Sm:ill:Chl	
1860-1862	15.23, 9.98	17.79, 9.98	9.98	7.15, HIT=0	Smectite+ Illite+Chlorite	Sm:ill:Chl	Feldspars
1876-1880	14.68, 10.05	17.17, 10.05	10.05	7.08, HIT=0	Smectite+ Illite+Chlorite	Sm:ill:Chl	Feldspars
1900-1902	14.19, 10.08	16.91, 10.08	10.08	7.08, HIT=0	Smectite+ Illite+Chlorite	Sm:ill:Chl	
1918-1920	14.04, 9.92	14.04, 9.92	14.04, 9.92	7.06, HIT=0	Chlorite + Illite	Chl: ill	
1940-1942	14.53, 10.01	16.99, 10.01	10.01	7.13, HIT=0	Smectite+ Illite+Chlorite	Sm:ill:Chl	Feldspars
1956-1958	14.26, 9.98	17.63, 9.98	9.98	7.15, HIT=0	Smectite+ Illite+Chlorite	Sm:ill:Chl	Feldspars
1958-1960	9.98	9.98	9.98	7.15, HIT=0	Unst. Chlorite + Illite	Chl: ill	Feldspars
1978-1980	9.84	9.84	9.84	7.12, HIT=0	Unst. Chlorite + Illite	Chl: ill	Feldspars

Depth (m)	d(001) A	d(001) G	d(001) H	d(002)	Mineral	Type	Other minerals
1996-1998	10.03	10.03	10.03	7.09, HIT=0	Unst. Chlorite + Illite	Chl: ill	Feldspars
2018-2020	9.96	9.96	9.96	7.14, HIT=0	Unst. Chlorite + Illite	Chl: ill	Feldspars
2038-2040	13.11, 10.17	17.41, 10.17	10.17	7.19, HIT=0	Smectite+ Illite+Chlorite	Sm:ill:Chl	Feldspars
2056-2058	10.12	10.12	10.12	7.15, HIT=0	Unst. Chlorite + Illite	Chl: ill	Feldspars
2058-2060	13.16, 9.95	16.94, 9.95	9.95	7.05, HIT=0	Smectite+ Illite+Chlorite	Sm:ill:Chl	Feldspars
2078-2080	14.06, 9.97	17.14, 9.97	9.97	7.04, HIT=0	Smectite+ Illite+Chlorite	Sm:ill:Chl	Feldspars
2096-2098	10.34	10.34	10.34	7.13, HIT=0	Unst. Chlorite + Illite	Chl: ill	Feldspars
2118-2120	14.28, 9.82	14.28, 9.82	14.28, 9.82	7.06, HIT=0	Chlorite + Illite	Chl: ill	Feldspars
2156-2158	9.94	9.94	9.94	7.13, HIT=0	Unst. Chlorite + Illite	Chl: ill	Feldspars
2196-2200	14.12, 9.96	17.12, 9.96	9.96	7.08, HIT=0	Smectite+ Illite+Chlorite	Sm:ill:Chl	
2198-2200	14.59, 10.09	14.59, 10.09	14.59, 10.09	7.13, HIT=0	Chlorite + Illite	Chl: ill	Feldspars
2240-2242	12.56	17.12	9.73	7.03, HIT=0	Smectite+ Chlorite	Sm:Chl	
2258-2262	14.73, 10.2	14.73, 10.2	14.73, 10.2	7.26, HIT=0	Chlorite + Illite	Chl: ill	Feldspars
2278-2282	15.2, 10.31	15.2, 10.31	15.2, 10.31	7.18, HIT=0	Chlorite + Illite	Chl: ill	Feldspars
2296-2300	14.02, 9.94	16.97, 9.94	9.94	7.07, HIT=0	Smectite+ + Illite+Chlorite	Sm:ill:Chl	
2316-2320	14.06, 10.16	16.94, 10.16	10.16	7.04, HIT=0	Smectite+ + Illite+ Chlorite	Sm:ill:Chl	
2338-2340	10.06	10.06	10.06	7.04, HIT=0	Unst. Chlorite + Illite	Chl: ill	
2338-2342	12.76, 9.89	16.94, 9.89	9.89	7.03, HIT=0	Smectite+ + Illite+Chlorite	Sm:ill:Chl	Feldspars
2354-2358	14.02, 10.11	17.26, 10.11	10.11	7.09, HIT=0	Smectite+ + Illite+ Chlorite	Sm:ill:Chl	
2458-2460	14.14, 10.14	17.39, 10.14	10.14	7.09, HIT=0	Smectite+ + Illite+ Chlorite	Sm:ill:Chl	
2482-2484	-	-	-	7.14, HIT=0	Unst. Chlorite	Chl.	Feldspars
2496-2500	10.01	10.01	10.01	7.07, HIT=0	Unst. Chlorite + Illite	Chl: ill	Feldspars
2516-2518	9.99	9.99	9.99	7.09, HIT=0	Unst. Chlorite + Illite	Chl: ill	Feldspars
2522-2524	10.86	10.86	10.86	7.12, HIT=0	Unst. Chlorite + Illite	Chl: ill	Feldspars
2536-2540	12.55, 9.99	17.03, 9.99	9.99	7.08, HIT=0	Smectite+ + Illite+ Chlorite	Sm:ill:Chl	Feldspars
2558-2562	14.45, 9.89	17.03, 9.89	9.89	7.09, HIT=0	Smectite+ + Illite+ Chlorite	Sm:ill:Chl	
2576-2580	13.01, 9.92	17.2, 9.92	9.92	7.11, HIT=0	Smectite+ + Illite+ Chlorite	Sm:ill:Chl	

Depth (m)	d(001) A	d(001) G	d(001) H	d(002)	Mineral	Type	Other minerals
2616-2618	12.48, 10.15	17.54, 10.15	10.15	7.08, HIT=0	Smectite+ + Illite+ Chlorite	Sm:ill:Chl	
2676-2678	14.77, 10.03	17.23, 10.03	10.03	7.08, HIT=0	Smectite+ + Illite+ Chlorite	Sm:ill:Chl	Feldspars
2696-2700	12.21, 9.91	17.14, 9.91	9.91	7.05, HIT=0	Smectite+ + Illite+ Chlorite	Sm:ill:Chl	
2716-2718	12.03, 9.91	12.02, 9.91	12.02, 9.91	7.09, HIT=0	Chlorite + Illite	Chl: ill	Feldspars
2758-2760	10.65	10.65	10.65	7.07, HIT=0	Unst. Chlorite + Illite	Chl: ill	Feldspars
2760-2762	10.72	10.72	10.72	7.09, HIT=0	Unst. Chlorite + Illite	Chl: ill	Feldspars
2798-2800	9.98	9.98	9.98	7.12, HIT=0	Unst. Chlorite + Illite	Chl: ill	Feldspars
2834-2836	14.36, 9.89	17.51, 9.89	9.89	7.13, HIT=0	Smectite+ + Illite+ Chlorite	Sm:ill:Chl	Feldspars
2840-2842	12.42, 10.06	17.15, 10.06	10.06	7.09, HIT=0	Smectite+ + Illite+ Chlorite	Sm:ill:Chl	Feldspars
2898-2900	13.16, 9.98	16.99, 9.98	9.98	7.04, HIT=0	Smectite+ + Illite+ Chlorite	Sm:ill:Chl	Feldspars
2918-2920	12.89, 10.14	17.54, 10.14	10.14	7.12, HIT=0	Smectite+ + Illite+ Chlorite	Sm:ill:Chl	Feldspars
2958-2960	10.05	10.05	10.05	7.07, HIT=0	Unst. Chlorite + Illite	Chl: ill	Feldspars
2978-2980	13.06, 9.95	17.26, 9.95	9.95	7.11, HIT=0	Smectite+ + Illite+ Chlorite	Sm:ill:Chl	Feldspars

APPENDIX C: ICP-OES analysis procedure

- The first step is to grind the drill chips in agate mortar to a fineness of approximately 100 mesh powder. Always remember to clean the mortar and pestle using acetone after grinding each sample to eliminate contamination between the samples.
- Weigh 100 mg ± 1mg of the sample in an epicure graphite crucible. Reset the scale to 0 g and add 200 mg ± 1 mg of flux (Lithium metaborate, $LiBO_2$) to the sample. Mix the two properly making sure that the mixture does not spill on the crucible walls. The purpose of the flux is to increase the melting temperature of the sample.
- Prepare the working standard samples. In this case, a total of six standard samples were prepared. These include three external reproducibility standards (K-1919, BIR-1 and BGM-1) and three internal calibration standards (A-THO, B-THO and B-ALK). 250 mg ± 1 mg of the sample and 500 mg ± 1 mg of the flux were used.
- The samples were melted in an electric furnace heated at 1000^{o}C for at least 30 mins and thereafter left to cool for another 15-20 mins. before the fused bead (or glass pellet) is transferred into a bottle containing 30 ml of Rockan complexing acid. The latter, basically is a mixture of de-ionized water, 5% HNO_3, 1.33% HCL and 1.33% semi-saturated Oxalic acid, $H_2C_2O_4$. The three calibration standards were however, transferred into three different bottles, each containing 75 ml of Rockan complexing acid. Highly acidic/highly alkaline solutions are not recommended for this analysis because they will extinguish the argon plasma.
- The glass pellet and Rockan complexing acid are immediately run in a carousel to complete solution to avoid silica precipitation. Complete solution is achieved between 2-3 hours. The samples are now ready for analysis at the ICP-OES machine.
- Analytical session began by running the three calibration standards. Spectra vision software was applied in the calculation of 2-3 points calibration for every single element. Instrumental reference sample (REF), used for monitoring drift during analysis was made of equal parts (a third) of the internal calibration standards. The REF was analysed at the beginning of the session and at 10 samples interval across the whole analytical period. One calibration standard (B-THO) was analysed in between a batch of 10 samples to observe instrument reproducibility in multiple analyses.
- During data processing, the raw data was copied and pasted into a correction spreadsheet. Thereafter, all the batch analyses were normalized to 100%. The spreadsheet calculates time dependent variation along each column of the analysis.
- Application of the time-dependent variation-correction to the batch results to equal absolute values of the reference samples, both at the beginning and the end

APPENDIX D: EMP analysis for chlorite and epidote

1. Quantitative analysis results for chlorite

Representative EMP analyses of Chlorite - Well OW-917 - 1870 m depth										
Point	**1**	**2**	**3**	**4**	**5**	**6**	**7**	**8**	**9**	**10**
SiO_2	22.78	22.62	22.26	19.58	24.59	22.93	22.67	22.62	22.67	20.09
TiO_2	0.09	0.08	0.06	0.04	0.04	0.08	0.06	0.02	0.08	0.00
Al_2O_3	18.46	18.72	18.3	16.33	17.81	18.67	18.39	18.05	18.73	15.93
FeO	34.38	34.55	33.32	34.55	30.82	33.88	34.62	33.60	33.76	33.64
MnO	0.70	0.85	0.80	0.70	1.07	0.65	0.78	0.66	0.63	0.66
MgO	5.42	4.84	4.81	5.3	6.1	4.96	5.83	4.91	5.01	5.93
CaO	0.05	0.04	0.10	0.07	0.07	0.05	0.03	0.06	0.06	0.05
Na_2O	0.42	0.33	0.44	0.47	1.07	0.42	0.39	0.39	0.29	0.33
K_2O	0.58	0.39	0.56	0.58	0.65	0.61	0.47	0.53	0.50	0.62
SrO	0.00	0.00	0.02	0.00	0.00	0.04	0.00	0.00	0.12	0.06
Total	82.88	82.40	80.68	77.62	82.22	82.29	83.25	80.84	81.86	77.32
Number of cations on the basis of 24 Oxygens										
Si	4.688	4.684	4.703	4.417	5.000	4.739	4.651	4.765	4.708	4.519
Ti	0.015	0.012	0.009	0.007	0.006	0.012	0.009	0.003	0.013	0.000
Al	4.480	4.569	4.558	4.342	4.267	4.548	4.447	4.481	4.586	4.225
Fe^{2+}	5.919	5.985	5.889	6.518	5.241	5.855	5.941	5.919	5.864	6.330
Mn	0.122	0.148	0.143	0.133	0.184	0.114	0.136	0.118	0.111	0.126
Mg	1.663	1.495	1.515	1.783	1.850	1.528	1.785	1.541	1.551	1.988
Ca	0.012	0.009	0.023	0.017	0.015	0.011	0.007	0.014	0.014	0.013
Na	0.166	0.131	0.182	0.207	0.424	0.168	0.156	0.161	0.119	0.146
K	0.152	0.103	0.150	0.167	0.170	0.160	0.122	0.142	0.133	0.178
Sr	0.000	0.000	0.003	0.000	0.000	0.005	0.000	0.000	0.015	0.008
Total	17.216	17.135	17.176	17.591	17.156	17.140	17.255	17.144	17.113	17.532

Representative EMP analyses of Chlorite -Well OW-922 - 2236 m depth										
Point	**1**	**2**	**3**	**4**	**5**	**6**	**7**	**8**	**9**	**10**
SiO_2	22.20	20.04	20.23	21.01	18.88	19.86	21.38	21.52	22.54	19.71
TiO_2	0.10	0.10	0.08	0.05	0.02	0.01	0.02	0.07	0.02	0.01
Al_2O_3	14.86	14.57	13.63	14.49	13.11	13.51	13.29	14.84	13.36	13.27
FeO	30.50	31.78	29.63	29.54	28.47	28.19	28.85	29.93	29.76	29.72
MnO	0.12	0.13	0.11	0.11	0.08	0.11	0.14	0.13	0.11	0.12
MgO	5.38	5.88	4.73	4.58	4.47	4.41	4.32	4.87	4.42	4.92
CaO	0.10	0.12	0.05	0.07	0.08	0.08	0.05	0.08	0.05	0.05
Na_2O	0.75	0.51	0.32	0.32	0.30	0.32	0.27	0.33	0.33	0.29
K_2O	0.32	0.31	0.31	0.32	0.38	0.45	0.29	0.48	0.27	0.34
SrO	0.03	0.00	0.00	0.00	0.00	0.05	0.00	0.00	0.00	0.00
Total	74.35	73.45	69.09	70.50	65.78	66.99	68.62	72.25	70.85	68.44
Number of cations on the basis of 24 Oxygens										
Si	5.050	4.702	4.997	5.045	4.919	5.039	5.265	5.039	5.365	4.941
Ti	0.017	0.018	0.014	0.008	0.003	0.002	0.004	0.012	0.003	0.002
Al	3.985	4.031	3.968	4.102	4.026	4.041	3.857	4.096	3.748	3.920
Fe^{2+}	5.803	6.236	6.122	5.934	6.204	5.982	5.940	5.861	5.924	6.231
Mn	0.023	0.026	0.024	0.023	0.018	0.024	0.030	0.025	0.021	0.025
Mg	1.824	2.057	1.742	1.638	1.736	1.668	1.584	1.699	1.567	1.837
Ca	0.024	0.030	0.014	0.018	0.021	0.021	0.013	0.020	0.012	0.014
Na	0.329	0.233	0.151	0.151	0.151	0.159	0.127	0.152	0.153	0.143
K	0.092	0.094	0.098	0.099	0.125	0.146	0.093	0.144	0.082	0.109
Sr	0.004	0.000	0.000	0.000	0.000	0.007	0.000	0.000	0.000	0.000
Total	17.151	17.426	17.130	17.018	17.203	17.090	16.913	17.048	16.876	17.222

Representative EMP analyses of Chlorite - Well OW-922 - 2782 m depth									
Point	**1**	**2**	**3**	**4**	**5**	**6**	**7**	**8**	**9**
SiO_2	23.42	32.83	23.41	22.12	20.96	24.07	30.84	27.84	20.75
TiO_2	0.02	0.04	0.04	0.06	0.00	0.01	0.01	0.00	0.00
Al_2O_3	15.51	12.45	15.38	13.85	14.26	14.65	15.47	10.01	13.46
FeO	35.23	29.59	33.21	32.97	30.77	33.49	28.02	26.06	32.73
MnO	0.24	0.20	0.26	0.33	0.28	0.26	0.32	0.22	0.29
MgO	4.07	4.08	4.33	5.38	4.66	5.08	4.01	2.83	3.81
CaO	0.14	0.09	0.08	0.16	0.14	0.16	0.13	0.12	0.18
Na_2O	0.09	0.14	0.33	0.18	0.17	0.08	1.69	0.17	0.12
K_2O	0.13	0.11	0.12	0.13	0.18	0.14	0.12	0.19	0.12
SrO	0.07	0.00	0.00	0.00	0.00	0.03	0.00	0.00	0.08
Total	78.92	79.54	77.17	75.18	71.41	77.97	80.61	67.44	71.55
Number of cations on the basis of 24 Oxygens									
Si	5.092	6.618	5.154	5.050	5.007	5.241	6.139	6.681	5.029
Ti	0.003	0.007	0.007	0.011	0.000	0.002	0.002	0.001	0.000
Al	3.975	2.960	3.991	3.727	4.015	3.760	3.629	2.832	3.844
Fe^{2+}	6.405	4.989	6.116	6.296	6.148	6.098	4.664	5.232	6.633
Mn	0.044	0.035	0.049	0.064	0.057	0.047	0.055	0.044	0.060
Mg	1.318	1.226	1.421	1.831	1.658	1.650	1.189	1.013	1.376
Ca	0.034	0.019	0.018	0.039	0.035	0.038	0.027	0.031	0.046
Na	0.038	0.055	0.143	0.080	0.078	0.035	0.651	0.078	0.058
K	0.035	0.029	0.033	0.039	0.053	0.038	0.030	0.059	0.039
Sr	0.009	0.000	0.000	0.000	0.000	0.004	0.000	0.000	0.012
Total	16.953	15.937	16.932	17.136	17.051	16.913	16.386	15.971	17.097

Representative EMP analyses of Chlorite - Well OW-910 - 864 m depth										
Point	**1**	**2**	**3**	**4**	**5**	**6**	**7**	**8**	**9**	**10**
SiO_2	24.59	25.16	23.22	24.92	24.25	25.25	25.02	25.04	25.90	23.93
TiO_2	0.03	0.02	0.04	0.03	0.05	0.00	0.03	0.00	0.01	0.04
Al_2O_3	13.23	13.51	12.57	12.86	11.94	13.14	12.95	13.68	13.34	12.34
FeO	12.16	12.24	12.67	12.46	12.02	12.20	12.60	11.96	12.33	12.03
MnO	0.21	0.26	0.20	0.19	0.18	0.21	0.19	0.23	0.19	0.21
MgO	17.05	16.63	17.30	16.72	16.21	16.70	17.58	15.63	15.73	17.10
CaO	0.29	0.28	0.27	0.37	0.32	0.31	0.31	0.29	0.30	0.33
Na_2O	0.00	0.06	0.04	0.02	0.03	0.01	0.03	0.01	0.02	0.04
K_2O	0.02	0.00	0.02	0.01	0.02	0.01	0.02	0.01	0.02	0.01
SrO	0.06	0.08	0.00	0.02	0.00	0.03	0.00	0.00	0.00	0.01
Total	67.64	68.24	66.33	67.60	65.02	67.85	68.73	66.84	67.83	66.04
Number of cations on the basis of 24 Oxygens										
Si	5.428	5.496	5.276	5.509	5.573	5.542	5.446	5.559	5.668	5.425
Ti	0.005	0.003	0.007	0.006	0.009	0.000	0.006	0.000	0.002	0.006
Al	3.441	3.477	3.367	3.350	3.233	3.399	3.323	3.582	3.440	3.297
Fe^{2+}	2.245	2.235	2.408	2.304	2.310	2.238	2.294	2.222	2.257	2.281
Mn	0.039	0.048	0.038	0.035	0.035	0.039	0.035	0.042	0.035	0.040
Mg	5.609	5.415	5.861	5.511	5.553	5.462	5.703	5.174	5.133	5.777
Ca	0.069	0.067	0.065	0.088	0.078	0.072	0.073	0.068	0.070	0.081
Na	0.000	0.024	0.019	0.009	0.014	0.004	0.013	0.003	0.007	0.019
K	0.004	0.000	0.005	0.002	0.006	0.002	0.005	0.002	0.005	0.003
Sr	0.008	0.010	0.000	0.003	0.000	0.004	0.000	0.000	0.000	0.002
Total	16.85	16.77	17.05	16.82	16.81	16.76	16.90	16.65	16.62	16.93

Representative EMP analyses of Chlorite - Well OW-910 - 1236 m depth										
Point	**1**	**2**	**3**	**4**	**5**	**6**	**7**	**8**	**9**	**10**
SiO_2	30.45	31.82	35.11	33.18	30.43	29.62	37.91	33.01	30.81	32.81
TiO_2	0.11	0.03	0.06	0.03	0.00	0.03	0.00	0.02	0.02	0.01
Al_2O_3	16.90	19.12	14.33	17.43	16.52	16.50	12.86	16.46	18.40	17.96
FeO	17.62	17.25	16.94	17.42	17.50	18.37	17.56	16.25	17.61	18.29
MnO	0.28	0.26	0.25	0.25	0.27	0.27	0.29	0.25	0.31	0.20
MgO	15.59	18.07	16.05	14.52	18.64	17.54	15.99	16.23	19.82	16.19
CaO	0.44	0.39	0.94	0.85	0.56	0.40	3.37	1.45	0.32	0.44
Na_2O	0.09	0.25	0.06	0.20	0.16	0.05	0.04	0.39	0.03	0.16
K_2O	0.01	0.04	0.04	0.22	0.06	0.02	0.05	0.10	0.03	0.17
SrO	0.02	0.02	0.00	0.05	0.04	0.00	0.01	0.01	0.02	0.00
Total	81.50	87.25	83.78	84.15	84.18	82.80	88.08	84.16	87.35	86.23
Number of cations on the basis of 24 Oxygens										
Si	5.634	5.463	6.239	5.902	5.469	5.439	6.452	5.863	5.316	5.717
Ti	0.015	0.004	0.008	0.004	0.000	0.004	0.000	0.002	0.002	0.002
Al	3.686	3.870	3.003	3.655	3.500	3.572	2.581	3.445	3.743	3.689
Fe^{2+}	2.726	2.477	2.519	2.592	2.631	2.822	2.499	2.413	2.542	2.666
Mn	0.043	0.038	0.038	0.037	0.041	0.042	0.042	0.038	0.045	0.029
Mg	4.298	4.626	4.252	3.85	4.993	4.803	4.058	4.297	5.096	4.206
Ca	0.087	0.072	0.179	0.162	0.109	0.078	0.614	0.276	0.058	0.082
Na	0.031	0.082	0.020	0.068	0.057	0.017	0.013	0.133	0.009	0.054
K	0.004	0.009	0.009	0.050	0.014	0.005	0.012	0.023	0.007	0.037
Sr	0.002	0.002	0.000	0.005	0.004	0.000	0.001	0.001	0.002	0.000
Total	16.53	16.64	16.27	16.33	16.82	16.78	16.27	16.49	16.82	16.48

Representative EMP analyses of Chlorite - Well OW-905A - 1560 m depth										
Point	**1**	**2**	**3**	**4**	**5**	**6**	**7**	**8**	**9**	**10**
SiO_2	25.68	25.61	24.72	26.12	25.19	24.12	24.99	26.53	24.96	25.54
TiO_2	0.03	0.00	0.05	0.01	0.00	0.04	0.05	0.00	0.08	0.02
Al_2O_3	19.48	19.16	19.08	19.53	18.94	22.21	18.95	19.79	18.92	19.29
FeO	35.60	34.41	35.64	35.47	36.21	31.47	36.55	35.91	35.22	35.78
MnO	2.20	2.02	2.20	2.13	2.26	1.98	2.36	2.25	2.38	2.25
MgO	7.08	7.87	7.23	7.44	7.08	7.87	7.55	7.36	8.25	7.84
CaO	0.18	0.11	0.13	0.13	0.11	0.13	0.12	0.15	0.15	0.10
Na_2O	0.09	0.02	0.03	0.08	0.07	0.21	0.03	0.09	0.02	0.00
K_2O	0.02	0.02	0.02	0.03	0.01	0.04	0.02	0.03	0.03	0.03
SrO	0.02	0.02	0.00	0.00	0.07	0.06	0.00	0.08	0.00	0.00
Total	90.39	89.26	89.09	90.94	89.94	88.13	90.62	92.19	90.00	90.85
Number of cations on the basis of 24 Oxygens										
Si	4.802	4.821	4.714	4.837	4.766	4.533	4.703	4.851	4.701	4.757
Ti	0.004	0.000	0.007	0.001	0.000	0.006	0.007	0.000	0.011	0.002
Al	4.294	4.250	4.288	4.264	4.224	4.920	4.203	4.264	4.200	4.235
Fe^{2+}	5.568	5.418	5.684	5.495	5.729	4.946	5.752	5.490	5.546	5.574
Mn	0.348	0.322	0.355	0.335	0.362	0.315	0.376	0.349	0.379	0.355
Mg	1.973	2.209	2.054	2.054	1.998	2.206	2.117	2.006	2.315	2.177
Ca	0.037	0.023	0.027	0.026	0.022	0.026	0.025	0.030	0.029	0.021
Na	0.032	0.009	0.010	0.028	0.027	0.077	0.012	0.031	0.008	0.000
K	0.005	0.005	0.004	0.008	0.002	0.009	0.004	0.006	0.006	0.008
Sr	0.002	0.003	0.000	0.000	0.008	0.007	0.000	0.009	0.000	0.000
Total	17.07	17.06	17.14	17.05	17.14	17.05	17.20	17.04	17.20	17.13

2. Quantitative analysis results for Epidote

Representative EMP analyses of Epidote - Well OW-922 - 2782 m depth										
Point	**1**	**2**	**3**	**4**	**5**	**6**	**7**	**8**	**9**	**10**
SiO_2	37.48	37.50	37.34	37.65	37.71	37.56	37.58	37.23	37.30	37.60
TiO_2	0.00	0.03	0.00	0.07	0.01	0.00	0.03	0.04	0.09	0.04
Al_2O_3	24.62	24.71	24.60	24.40	24.71	24.43	24.48	24.43	24.59	24.29
Fe_2O_3	12.71	12.48	12.49	12.44	12.59	12.57	12.38	12.46	12.29	12.44
MnO	0.11	0.17	0.13	0.13	0.19	0.14	0.14	0.16	0.09	0.17
MgO	0.11	0.05	0.08	0.08	0.07	0.07	0.07	0.08	0.10	0.07
CaO	22.97	22.81	22.91	22.94	22.90	22.48	22.65	22.73	22.64	22.50
Na_2O	0.02	0.03	0.00	0.04	0.06	0.03	0.03	0.04	0.06	0.07
K_2O	0.04	0.04	0.05	0.04	0.05	0.05	0.04	0.03	0.05	0.06
SrO	0.36	0.32	0.51	0.44	0.41	0.46	0.50	0.46	0.27	0.55
Total	98.43	98.13	98.10	98.23	98.71	97.79	97.91	97.66	97.49	97.79
Number of cations on the basis of 24 Oxygens										
Si	5.694	5.707	5.695	5.729	5.710	5.736	5.733	5.702	5.708	5.747
Ti	0.000	0.003	0.000	0.008	0.001	0.000	0.004	0.004	0.010	0.005
Al	4.409	4.432	4.422	4.377	4.411	4.399	4.402	4.410	4.436	4.376
Fe^{3+}	1.454	1.429	1.433	1.423	1.435	1.444	1.422	1.436	1.416	1.430
Mn	0.015	0.021	0.016	0.017	0.024	0.018	0.018	0.021	0.012	0.023
Mg	0.024	0.012	0.018	0.018	0.016	0.016	0.016	0.017	0.024	0.016
Ca	3.740	3.720	3.743	3.740	3.716	3.679	3.703	3.730	3.713	3.685
Na	0.006	0.010	0.000	0.013	0.018	0.010	0.010	0.013	0.017	0.020
K	0.008	0.007	0.009	0.008	0.010	0.010	0.009	0.006	0.009	0.011
Sr	0.032	0.028	0.045	0.039	0.036	0.040	0.044	0.041	0.024	0.049
Total	15.382	15.370	15.380	15.372	15.378	15.352	15.360	15.380	15.369	15.361

Representative EMP analyses of Epidote - Well OW-910 - 864 m depth										
Point	**1**	**2**	**3**	**4**	**5**	**6**	**7**	**8**	**9**	**10**
SiO_2	38.00	37.67	37.70	37.80	37.74	37.92	37.32	38.14	37.49	37.98
TiO_2	0.05	0.09	0.01	0.01	0.06	0.11	0.24	0.02	0.11	0.11
Al_2O_3	24.18	22.99	23.45	23.92	23.93	24.54	22.21	25.57	20.46	25.29
Fe_2O_3	13.37	15.02	14.38	13.90	13.68	13.28	16.14	11.86	18.56	12.01
MnO	0.02	0.09	0.00	0.06	0.10	0.08	0.14	0.04	0.09	0.06
MgO	0.13	0.13	0.06	0.08	0.06	0.06	0.09	0.06	0.11	0.06
CaO	23.23	23.16	23.38	23.33	23.62	23.38	23.21	23.15	22.80	23.38
Na_2O	0.00	0.06	0.00	0.01	0.00	0.01	0.00	0.00	0.00	0.02
K_2O	0.01	0.00	0.00	0.00	0.00	0.00	0.00	0.01	0.00	0.01
SrO	0.19	0.00	0.16	0.09	0.21	0.27	0.10	0.22	0.00	0.22
Total	99.17	99.22	99.14	99.21	99.41	99.64	99.46	99.08	99.63	99.14
Number of cations on the basis of 24 Oxygens										
Si	5.731	5.714	5.714	5.712	5.699	5.697	5.681	5.721	5.733	5.707
Ti	0.005	0.011	0.001	0.001	0.007	0.012	0.028	0.002	0.013	0.013
Al	4.299	4.109	4.190	4.260	4.259	4.345	3.984	4.521	3.688	4.478
Fe^{3+}	1.517	1.714	1.640	1.581	1.554	1.501	1.849	1.339	2.136	1.358
Mn	0.002	0.012	0.000	0.008	0.012	0.010	0.018	0.005	0.012	0.008
Mg	0.030	0.030	0.014	0.019	0.014	0.013	0.021	0.014	0.025	0.013
Ca	3.753	3.764	3.797	3.778	3.822	3.764	3.785	3.721	3.736	3.763
Na	0.000	0.018	0.000	0.003	0.000	0.002	0.000	0.001	0.000	0.005
K	0.002	0.000	0.000	0.000	0.000	0.000	0.001	0.002	0.000	0.002
Sr	0.016	0.000	0.014	0.008	0.019	0.023	0.009	0.020	0.000	0.019
Total	15.355	15.372	15.370	15.370	15.386	15.368	15.375	15.346	15.343	15.366

Representative EMP analyses of Epidote - Well OW-910 - 1236 m depth										
Point	**1**	**2**	**3**	**4**	**5**	**6**	**7**	**8**	**9**	**10**
SiO_2	37.64	35.24	36.30	39.07	46.13	44.57	36.16	35.77	35.48	35.81
TiO_2	0.58	0.57	0.67	0.44	0.49	0.56	0.47	0.49	0.39	0.34
Al_2O_3	8.73	7.67	7.75	9.15	9.18	6.66	8.03	7.23	6.92	7.19
Fe_2O_3	18.66	20.21	20.37	19.53	14.88	21.70	19.91	21.11	21.34	22.18
MnO	0.49	0.51	0.44	0.28	0.26	0.42	0.48	0.39	0.36	0.30
MgO	0.50	0.62	0.41	0.40	0.60	0.36	0.35	0.29	0.32	0.49
CaO	30.05	32.50	32.36	29.69	22.75	24.41	32.59	33.05	33.16	32.44
Na_2O	0.88	0.03	0.21	1.07	0.17	0.06	0.02	0.01	0.04	0.06
K_2O	0.17	0.07	0.07	0.07	3.59	0.62	0.03	0.05	0.09	0.04
SrO	0.02	0.04	0.00	0.05	0.00	0.01	0.00	0.01	0.10	0.05
Total	97.71	97.47	98.58	99.74	98.05	99.37	98.04	98.41	98.19	98.90
Number of cations on the basis of 24 Oxygens										
Si	6.146	5.873	5.958	6.219	7.191	6.957	5.961	5.916	5.900	5.897
Ti	0.071	0.072	0.083	0.053	0.058	0.066	0.058	0.061	0.048	0.042
Al	1.681	1.506	1.499	1.716	1.686	1.225	1.559	1.409	1.356	1.395
Fe^{3+}	2.293	2.536	2.517	2.339	1.745	2.549	2.471	2.628	2.670	2.750
Mn	0.068	0.072	0.061	0.038	0.034	0.055	0.067	0.055	0.051	0.041
Mg	0.121	0.155	0.099	0.095	0.140	0.084	0.086	0.070	0.078	0.120
Ca	5.258	5.804	5.692	5.064	3.801	4.082	5.756	5.857	5.909	5.725
Na	0.279	0.010	0.067	0.329	0.051	0.018	0.005	0.004	0.013	0.020
K	0.035	0.015	0.015	0.013	0.713	0.123	0.006	0.010	0.019	0.008
Sr	0.002	0.004	0.000	0.004	0.000	0.001	0.000	0.001	0.009	0.005
Total	15.953	16.047	15.992	15.871	15.418	15.160	15.970	16.012	16.054	16.003

Representative EMP analyses of Epidote - Well OW-905A - 1560 m depth										
Point	**1**	**2**	**3**	**4**	**5**	**6**	**7**	**8**	**9**	**10**
SiO_2	37.12	36.39	36.95	38.03	37.29	37.88	34.16	37.32	38.01	37.42
TiO_2	0.14	0.08	0.23	0.11	0.08	0.11	0.34	0.13	0.16	0.11
Al_2O_3	23.10	23.48	19.55	24.18	24.02	24.34	20.39	24.09	24.44	24.18
Fe_2O_3	14.86	13.78	19.53	13.82	13.30	13.73	15.45	13.41	13.75	13.15
MnO	1.53	1.05	0.94	0.93	1.03	1.01	0.62	1.46	1.61	0.69
MgO	0.05	0.02	0.02	0.02	0.01	0.03	0.03	0.03	0.01	0.00
CaO	21.50	22.16	21.76	22.39	21.79	21.90	21.88	21.51	21.69	22.42
Na_2O	0.00	0.01	0.01	0.02	0.01	0.00	0.00	0.00	0.00	0.00
K_2O	0.01	0.01	0.00	0.01	0.03	0.03	0.05	0.03	0.01	0.02
SrO	0.05	0.01	0.06	0.04	0.00	0.03	0.09	0.00	0.02	0.09
Total	98.35	97.00	99.05	99.54	97.55	99.07	93.01	97.98	99.71	98.08
Number of cations on the basis of 24 Oxygens										
Si	5.693	5.647	5.720	5.725	5.721	5.722	5.599	5.709	5.715	5.711
Ti	0.016	0.010	0.027	0.012	0.009	0.012	0.042	0.015	0.019	0.012
Al	4.175	4.295	3.566	4.291	4.343	4.334	3.940	4.342	4.331	4.349
Fe^{3+}	1.715	1.609	2.275	1.566	1.536	1.561	1.906	1.544	1.555	1.510
Mn	0.199	0.139	0.124	0.118	0.133	0.129	0.086	0.189	0.205	0.090
Mg	0.011	0.005	0.004	0.004	0.003	0.007	0.008	0.007	0.003	0.000
Ca	3.534	3.684	3.610	3.612	3.581	3.546	3.842	3.525	3.495	3.666
Na	0.000	0.002	0.002	0.005	0.002	0.001	0.000	0.000	0.000	0.000
K	0.001	0.002	0.000	0.002	0.005	0.006	0.010	0.007	0.001	0.004
Sr	0.004	0.001	0.005	0.003	0.000	0.003	0.009	0.000	0.002	0.008
Total	15.348	15.393	15.333	15.338	15.334	15.321	15.442	15.337	15.326	15.350